

MODELING AND SIMULATION OF PORE-SCALE MULTIPHASE FLUID FLOW AND REACTIVE TRANSPORT IN FRACTURED AND POROUS MEDIA

Paul Meakin^{1,2,3} and Alexandre M. Tartakovsky⁴

Received 8 February 2008; accepted 18 December 2008; published 14 July 2009.

[1] In the subsurface, fluids play a critical role by transporting dissolved minerals, colloids, and contaminants (sometimes over long distances); by mediating dissolution and precipitation processes; and by enabling chemical transformations in solution and at mineral surfaces. Although the complex geometries of fracture apertures, fracture networks, and pore spaces may make it difficult to accurately predict fluid flow in saturated (single-phase) subsurface systems, well-developed methods are available. The simulation of multiphase fluid flow in the subsurface is much more challenging because of the large density and/or viscosity ratios found in important applications (water/air in the vadose zone; water/oil, water/gas, gas/oil, and water/oil/gas in hydrocarbon reservoirs; water/air/nonaqueous phase liquids (nonaqueous phase liquids/dense nonaqueous phase liquids) in contaminated vadose zone systems; and gas/molten rock in volcanic systems, for example). In addition, the complex behavior of fluid-fluid-solid contact lines and their impact on dynamic contact angles must also

be taken into account and coupled with the fluid flow. Here we review the methods that are currently being used to simulate pore-scale multiphase fluid flow and reactive transport in fractured and porous media. After the introduction, the review begins with an overview of the fundamental physics of multiphase fluids flow followed by a more detailed discussion of the complex dynamic behavior of contact lines and contact angles, an important barrier to accurate pore-scale modeling and simulation. The main part of the review focuses on five different approaches: pore network models, lattice gas and lattice Boltzmann methods, Monte Carlo methods, particle methods (molecular dynamics, dissipative particle dynamics, and smoothed particle hydrodynamics), and traditional grid-based computational fluid dynamics coupled with interface tracking and a contact angle model. Finally, the review closes with a discussion of future trends and challenges.

Citation: Meakin, P., and A. M. Tartakovsky (2009), Modeling and simulation of pore-scale multiphase fluid flow and reactive transport in fractured and porous media, *Rev. Geophys.*, 47, RG3002, doi:10.1029/2008RG000263.

1. INTRODUCTION

[2] Fluids play a critical role in a wide range of geological processes. For example, hydration and dehydration processes are common, and they are often coupled with fracturing and fluid flow [Jamtveit *et al.*, 2000; Strating and Vissers, 1991]. Because diffusion coefficients are usually small, and the time required for diffusive transport through a distance of l is proportional to l^2 while the time required for advection through the same distance is proportional to l ,

advective transport of dissolved species is critically important in a very wide range of subsurface geochemical transformations, and both dissolved minerals and anthropogenic contaminants may travel through great distances in the subsurface as a result of fluid flow. The transport of colloids, including anthropogenic and natural nanoparticles, is also mediated by the flow of water and other fluids. Although many fractured and porous geological systems are saturated with a single fluid (usually water with a variety of dissolved minerals and gasses), pore spaces and fracture apertures are often occupied simultaneously by two, and sometimes more, fluids. Well-known examples include the vadose zone (air and an aqueous phase), geothermal systems (an aqueous phase and a gas phase that contains steam and a variety of other gasses), and metamorphic systems [Yardley and Bottrell, 1988]. Economically important systems include oil reservoirs (oil/aqueous/gas) and gas reservoirs (aqueous/gas).

¹Center for Advanced Modeling and Simulation, Idaho National Laboratory, Idaho Falls, Idaho, USA.

²Also at Physics of Geological Processes, University of Oslo, Oslo, Norway.

³Also at Multiphase Flow Assurance Innovation Center, Institute for Energy Technology, Kjeller, Norway.

⁴Computational Mathematics Technical Group, Computational and Information Sciences Directorate, Pacific Northwest National Laboratory, Richland, Washington, USA.

[3] In principle, the pore-scale simulation of single-phase fluid flow through fractured and porous media is relatively straightforward. However, the complex geometries of pore spaces, fracture apertures, and fracture networks may result in severe practical difficulties and large uncertainties. On larger scales, single-phase fluid flow simulations are usually based on the idea that the properties of subsurface media fluctuate on scales that are significantly smaller and significantly larger than the scale of a representative elementary volume (REV) and that the fluctuations are small on intermediate scales (on the order of the REV scale over which the structural details can be averaged [Bear, 1972]). In large-scale simulations, macroscopic parameters such as the porosity and permeability are assigned to each REV on the basis of experimental information and statistical correlations, and heterogeneities on the REV scale are averaged (upscaled) to the much larger scale of the grid blocks used in field-scale or reservoir-scale simulations. One of the objectives of pore-scale simulations is to calculate the properties of subsurface media over a representative elementary volume. However, the concept of a representative elementary volume is not generally well founded, particularly for fluid flow in fractured media.

[4] The representative elementary volume concept is also applied broadly in the large-scale simulation of multiphase fluid flow. In these applications the flux densities and the potential gradients of the fluid phases are related by relative permeabilities (Onsager transport coefficients [Onsager, 1931a, 1931b]), including coupling coefficients, that depend on the fluid volume fractions (relative saturations) in the REV. In general, multiphase fluid flow exhibits hysteretic and history-dependent behavior that cannot be rigorously described by simple relative permeability/saturation/capillary pressure models.

[5] Pore-scale simulations are important because pore-scale phenomena have an important impact on larger-scale phenomena, and it is easier to systematically vary fluid properties, pore space geometries, and boundary conditions in computer simulations than in experiments. Although it is very difficult to directly use results obtained from pore-scale simulations to improve quantitative predictions based on large-scale simulations, the understanding and information obtained from pore-scale investigations does contribute to our ability to understand large-scale natural processes and improve large-scale geotechnical applications.

[6] Pore-scale simulations of multiphase fluid flow in confined systems are much more challenging than single-phase flow simulations for three fundamental reasons: (1) a fast, robust, and accurate way must be found to track the complex dynamics of fluid-fluid interfaces (or less efficient methods that do not require interface tracking must be employed); (2) the behavior of multiphase fluids with large density, viscosity, and compressibility ratios is difficult to simulate accurately with many methods; and (3) the behavior of fluid-fluid-solid contact lines (and the associated dynamic contact angles) is inherently complex and sensitive to small length-scale physical and chemical heterogeneities and impurities that influence the wetting behavior and/or

surface tension. In addition, Marangoni effects (flow driven by surface tension gradients [Marangoni, 1865]) may be important in some cases in which natural surfactants are present or synthetic surfactants are used for applications such as enhanced oil recovery and contaminant remediation. In addition, phenomena such as the nucleation and growth of bubbles, boiling, and the dissolution of bubbles are important in some systems. Processes that depend on nucleation are particularly difficult to model because they depend on thermally driven fluctuations and/or the presence of nucleation centers (surfaces and particles) that are difficult to characterize. In both cases, atypically large fluctuations or atypical nucleation sites may play a crucial role. This review is concerned with multiphase fluid flow and reactive transport on small scales where the major source of uncertainty is a consequence of these fundamental issues. On larger scales, lack of information about complex multi-scale heterogeneity is usually the main source of uncertainty. Geological systems are heterogeneous on all scales from the scale of defects on mineral surfaces, the roughness of pore walls, and diagenetic minerals formed in pore spaces to the scale of oil reservoirs, aquifers, and sedimentary basins and beyond.

[7] Pore network models have been used extensively to simulate multiphase and single-phase fluid flow in porous media, and these models will continue to provide important insight and information in the future. However, pore network models are based on simplified models for the pore space geometry and, in the case of multiphase fluid flow, simplified physics. In addition, pore network models are not well suited for the simulation of multiphase fluid flow in fracture apertures, fractured porous media, vuggy carbonates, or other systems with complex "macropores." More recently, a number of methods based more firmly on first principles have been developed. These methods include lattice Boltzmann simulations [Frisch *et al.*, 1986; D'Humieres *et al.*, 1986], particle methods such as dissipative particle dynamics [Hoogerbrugge and Koelman, 1992; Espanol and Warren, 1995] and smoothed particle hydrodynamics [Lucy, 1977; Gingold and Monaghan, 1977], and computational fluid dynamics with fluid-fluid interface tracking/capturing and velocity-dependent contact angles [Huang *et al.*, 2005]. These newer methods are less computationally efficient than pore network models, but the sustained increases in the capability of computing systems are making them more attractive. Despite recent advances, it is still not possible to accurately and reliably simulate multiphase fluid flow for the full range of density ratios, viscosity ratios, compressibilities, and wetting behaviors found in subsurface systems. Simple pore-scale and sub-pore-scale models for multiphase fluid flow and reactive solute transport have also been developed. In the future, multiscale multiphysics models for multiphase fluid flow and reactive transport will be developed, implemented on high-performance computing systems, and applied to subsurface processes.

[8] Because of its scientific interest and practical importance, multiphase fluid dynamics has been investigated

using both experimental and computational methods by a large community of scientists and engineers. Consequently, a quite large number of methods have been developed to simulate multiphase fluid flow. In this review we focus on the methods that have been used to simulate multiphase fluid flow in porous, fractured, and fractured porous geomaterials on the pore scale.

2. FUNDAMENTALS

[9] All of the properties of fluids and their behavior in the vicinity of solid surfaces can, in principle, be understood in terms of the interactions between their molecular components, the interactions between these molecular components and solids, and the effects of the temperature, T , that determines the average kinetic energy via the principle of equipartition of energy,

$$\frac{1}{2}m\bar{v}^2 = \frac{3}{2}k_B T \quad \text{or} \quad \frac{1}{2}m\bar{v}_i^2 = \frac{1}{2}k_B T, \quad (1)$$

where m is the molecular mass; k_B is the Boltzmann constant; T is the temperature; $\bar{v}^2 = \langle \mathbf{v} \cdot \mathbf{v} \rangle$ is the mean square velocity; v_i is the i th Cartesian component of the velocity, \mathbf{v} ; and \bar{v}_i^2 is the mean square of the i th velocity component. In general, the intermolecular interactions consist of a combination of long-range attractive interactions and short-range repulsive interactions.

[10] Analytical methods are incapable of accurately predicting fluid properties from intermolecular interactions, and quantum molecular dynamics or classical molecular dynamics with accurate interaction potentials must be used for this purpose. Monte Carlo methods with accurate interaction potentials can also be used to obtain some fluid properties. In many molecular dynamics simulations used to investigate the generic properties of fluids and solids, the molecules are represented by point masses, and the pairwise molecule-molecule interactions are represented by a Lennard-Jones potential [Allen and Tildesley, 1987],

$$E(r) = E_0 \left[(\sigma/r)^{12} - (\sigma/r)^6 \right], \quad (2)$$

where σ is the characteristic interaction distance (the distance at which the long-range attractive and short-range repulsive components of the interaction energy are equal), E_0 is the amplitude of the potential, and $E(r)$ is the interaction potential energy of a pair of particles separated by a distance of r . Usually, the interaction energy is replaced by the truncated Lennard-Jones potential,

$$E(r) = E_0 \left[(\sigma/r)^{12} - (\sigma/r)^6 \right] - E_0 \left[(\sigma/r_c)^{12} - (\sigma/r_c)^6 \right] \quad \text{if } r < r_c \quad (3a)$$

$$E(r) = 0 \quad \text{if } r > r_c, \quad (3b)$$

to reduce the number of particle-particle interactions that must be calculated. (Even with a cutoff in the range of

interaction, most of the computing time in molecular dynamics simulations is used to calculate the interatomic or intermolecular forces at each step.) At high particle number densities, corresponding to an average interparticle separation less than approximately σ (the minimum of the interaction potential is at $r = 2^{1/6}\sigma$), the repulsive part of the interaction is dominant; the ensemble of particles behaves as a solid, liquid, or dense supercritical fluid, depending on the temperature; and the compressibility of the fluid is small. Under these conditions (at temperatures above the melting point and at strain rates that are not too high), the flow of the Lennard-Jones fluid can be described quite accurately by the incompressible Navier-Stokes equations consisting of the momentum conservation equation

$$\rho \partial \mathbf{v} / \partial t = -\rho(\mathbf{v} \cdot \nabla) \mathbf{v} - \nabla P + \eta \nabla^2 \mathbf{v} + \mathbf{f}_b, \quad (4)$$

where \mathbf{v} is the fluid velocity, ρ is the fluid density, P is the pressure, η is the dynamic viscosity of the fluid, and \mathbf{f}_b is the force per unit volume acting on the fluid because of gravity and other body forces, and the volume conservation equation

$$\nabla \cdot \mathbf{v} = 0. \quad (5)$$

In practice, the incompressible Navier-Stokes equations often work quite well for compressible fluids such as gases. However, if compressibility effects cannot be neglected, the momentum conservation equation must be replaced by

$$\rho \partial \mathbf{v} / \partial t = -\rho(\mathbf{v} \cdot \nabla) \mathbf{v} - \nabla P + \eta \nabla^2 \mathbf{v} + (2\eta/3 + \lambda) \nabla(\nabla \cdot \mathbf{v}) + \mathbf{f}_b, \quad (6a)$$

$$\rho \partial \mathbf{v} / \partial t = -\rho(\mathbf{v} \cdot \nabla) \mathbf{v} - \nabla P + \eta \nabla^2 \mathbf{v} + (\eta + \eta') \nabla(\nabla \cdot \mathbf{v}) + \mathbf{f}_b, \quad (6b)$$

or

$$\rho \partial \mathbf{v} / \partial t = -\rho(\mathbf{v} \cdot \nabla) \mathbf{v} - \nabla P + \eta \nabla^2 \mathbf{v} + \eta_b \nabla(\nabla \cdot \mathbf{v}) + \mathbf{f}_b, \quad (6c)$$

where η' is the second viscosity [Liebermann, 1949], η_b is the bulk viscosity, and λ is the element of the viscosity tensor corresponding to the second Lamé coefficient in linear elasticity, which is also called the second viscosity coefficient. (In general, the viscosity is a fourth-rank tensor that relates the second-rank stress tensor, $\boldsymbol{\sigma}$, to the second-rank strain rate tensor, $\dot{\boldsymbol{\epsilon}}$ ($\boldsymbol{\sigma} = \boldsymbol{\eta} : \dot{\boldsymbol{\epsilon}}$). For a d -dimensional isotropic fluid, the elements of the viscosity tensor, $\boldsymbol{\eta}$, are given by $\eta_{ijkl} = \eta(\delta_{ik}\delta_{jl} + \delta_{il}\delta_{jk}) + \lambda\delta_{ij}\delta_{kl}$. It is often assumed, without justification, that the bulk viscosity, $\eta_b = \lambda + 2\eta/3$, is zero, and bulk viscosity coefficients are not available for many fluids under conditions that are important in geological systems. The viscous term in the Navier-Stokes equation can also be written as $\nabla \cdot \{\boldsymbol{\eta} \cdot [\nabla \otimes \mathbf{v} + (\nabla \otimes \mathbf{v})^T]\}$, and, in general, the viscosity tensor depends on both the temperature and pressure.) In addition, the volume conservation equation

must be replaced by the mass conservation or continuity equation

$$\partial \rho / \partial t + \nabla \cdot (\rho \mathbf{v}) = 0. \quad (7)$$

In some subsurface applications, the fluid temperatures may vary, and equations (4) and (5) can be supplemented by an energy equation such as

$$\rho dU/dt = -\rho \mathbf{v} \cdot \nabla U + \nabla \cdot k_T \nabla T - P \nabla \cdot \mathbf{v} + \Phi_{\text{visc}} + \dot{q} \quad (8)$$

or the conservation of energy equation [Anderson, 1995]

$$\rho d(U + v^2/2)/dt = -\rho \mathbf{v} \cdot \nabla (U + v^2/2) + \nabla \cdot k_T \nabla T - P \nabla \cdot \mathbf{v} + \Phi_{\text{visc}} + \dot{q} + \rho \mathbf{f}_b \cdot \mathbf{v}, \quad (9)$$

where U is the internal energy density per unit mass; k_T is the thermal conductivity, which is related to the thermal diffusion coefficient, \mathcal{D}_T , by $k_T = \mathcal{D}_T \rho C_p$, where C_p is the heat capacity at constant pressure; and \dot{q} is the rate of heat generation per unit volume due to radiative heating, etc. In equations (8) and (9) Φ_{visc} , the viscous dissipation, is given by $\Phi_{\text{visc}} = \boldsymbol{\sigma}_\eta : \dot{\boldsymbol{\epsilon}} = \dot{\boldsymbol{\epsilon}} : \boldsymbol{\eta} : \dot{\boldsymbol{\epsilon}}$, where $\boldsymbol{\sigma}_\eta$ is the viscous stress tensor, $\dot{\boldsymbol{\epsilon}}$ is the strain rate tensor, and $\boldsymbol{\eta}$ is the fourth-rank viscosity tensor. The energy dissipation equation can also be written in the form $\Phi_{\text{visc}} = (\eta/2)[\nabla \otimes \mathbf{v} + (\nabla \otimes \mathbf{v})^T] : [\nabla \otimes \mathbf{v} + (\nabla \otimes \mathbf{v})^T] + \lambda(\nabla \cdot \mathbf{v})^2$, where “ \otimes ” indicates the tensor product. If the fluid is incompressible, then $\nabla \cdot \mathbf{v} = 0$, and the rate of heat production due to viscous dissipation is given by $\Phi_{\text{visc}} = (\eta/2)[\nabla \otimes \mathbf{v} + (\nabla \otimes \mathbf{v})^T] : [\nabla \otimes \mathbf{v} + (\nabla \otimes \mathbf{v})^T]$. For real fluids, the density and viscosity will be temperature-dependent, and a heat transport equation must be used to calculate the time-dependent temperature field. In general, the energy conservation equation includes the diffusion and advection of heat as well as chemical transformations, phase changes, and other processes such as viscous dissipation and radioactive decay that result in the generation or absorption of heat. The coupling between chemical processes (chemical kinetics and molecular diffusion), fluid flow, and heat transport is important in many subsurface applications, and a chemical kinetics model with temperature-dependent rate constants is needed if the temperature varies by more than $O(1)$ K. In addition, changes in temperature will change the equilibrium compositions of multicomponent fluids, and this must be taken into account together with chemical diffusion.

[11] In addition to the conservation of momentum, mass, and energy during fluid flow, fluids are isotropic, and the physics of fluids is Galilean invariant. The isotropy of simple fluids allows the 81 elements of the viscosity tensor to be expressed in terms of just two viscosity coefficients (η and λ , for example) just as the elastic tensor can be expressed in terms of the two Lamé coefficients (or combinations of them such as the shear modulus and Young’s modulus) for an isotropic solid. Any serious model for the behavior of fluids must conform to these basic conservation principles and symmetries. The fact that the

flow of essentially all simple fluids can be described by the Navier-Stokes equation, irrespective of their composition, is an important universality. Under extreme strain rate conditions, the Navier-Stokes equations can no longer be applied because of changes in the structure of the fluid and because of a rapid increase in temperature. In more complex fluids, such as polymer solutions, high solid volume fraction colloidal dispersions, and liquid crystals, the structure is much more sensitive to the strain rate, and these fluids exhibit a distinctly non-Newtonian behavior at quite low strain rates. In some cases, these complex fluids can be described by a modified Navier-Stokes equation with a strain rate-dependent effective viscosity, $\eta(\dot{\boldsymbol{\epsilon}})$, where $(\dot{\boldsymbol{\epsilon}})$ is the strain rate. For example, $\eta(\dot{\boldsymbol{\epsilon}}) \propto \dot{\gamma}^{n-1}$, where $\dot{\gamma}$ is the shear strain rate, with $n < 1$ for shear thinning power law fluids and $n > 1$ for shear thickening power law fluids. In other cases, complex fluids may not flow until a critical shear stress is exceeded. For example, molten and partially molten rocks are often modeled as Bingham fluids with a nonzero yield stress. In other cases, the behavior of the complex fluid is history-dependent, and the relation between the strain rate and the stress may be highly nonlinear. Although complex fluids can be used to enhance oil recovery, heavy oils may have non-Newtonian rheologies, and subsurface biocolloidal systems may behave like complex fluids under some conditions (when nutrients are used to stimulate bioremediation, for example); the simulation of these systems is beyond the scope of this review.

[12] In general, fluid systems consist of a number of chemically distinct components, C , which may form a number of coexisting phases, \bar{P} . At equilibrium, the chemical potential, $\mu(P, T, \{x\})$, of each component must be the same in each phase, where $\{x\}$ is the set of composition variables and P is the pressure. This imposes $C(\bar{P} - 1)$ constraints, which, together with the \bar{P} constraints imposed by the requirement that $\sum_{i=1, C} x_i = 1$ in each phase, reduces the number of degrees of freedom from $C\bar{P} + 2$ to

$$\begin{aligned} F &= (C\bar{P} + 2) - C(\bar{P} - 1) - \bar{P} = C\bar{P} + 2 - C\bar{P} + C - \bar{P} \\ &= C - \bar{P} + 2, \end{aligned} \quad (10)$$

and this is the Gibbs phase rule. For example, above the liquid-vapor critical point for a pure material, $C = 1$, there is only one phase, $\bar{P} = 1$, and the number of degrees of freedom (the number of independent intensive variables) is two (both the temperature and pressure can be varied independently). Below the critical temperature, two phases may be in equilibrium along the liquid-vapor phase boundary. Under these conditions, there is still only one component, and there is one degree of freedom (either the pressure or the temperature may be changed, but once one has been changed the other is determined by the constraint of maintaining equilibrium between the liquid and vapor phases). In a two-component liquid-liquid mixture, there may be one or two phases in equilibrium corresponding to three or two degrees of freedom, and in the single-phase region(s) the temperature, pressure, and composition can be independently changed. Two liquid phases with different

compositions may be at equilibrium at points on a two-dimensional surface (or surfaces) in the temperature, pressure, and composition space, and there are two degrees of freedom.

[13] The free energy density (free energy per unit volume) of a binary two-component fluid or a single-component fluid can be described by a Ginzburg-Landau/Cahn-Hilliard free energy functional [Cahn and Hilliard, 1958; Ginzburg and Landau, 1950]

$$F^T(\mathbf{x}) = F[\phi(\mathbf{x})] + F'[\nabla\phi(\mathbf{x})], \quad (11)$$

where $\phi(\mathbf{x})$ is the compositional or fluid density order parameter (also referred to as the phase field) at position \mathbf{x} , $F(\phi)$ is the free energy density for a homogeneous fluid with an order parameter of ϕ , and $F'[\nabla\phi(\mathbf{x})]$ is the contribution to the free energy due to concentration or density gradients. Equation (11) is most often used for single-component fluids under conditions that result in the formation of coexisting liquid and gas phases or when a two-component liquid separates into two liquid phases with different compositions. Under these conditions large order parameter (density or composition) gradients occur in a narrow interface zone (except very near the critical point where the thickness of the interface is relatively large and the gradients are small). The total free energy of the fluid is given by

$$\mathcal{F} = \int_{\Omega} F^T(\mathbf{x}) d\mathbf{x} = \int_{\Omega} \{F[\phi(\mathbf{x})] + F'[\nabla\phi(\mathbf{x})]\} d\mathbf{x}, \quad (12)$$

where Ω is the fluid domain, $d\mathbf{x} = dx dy$ for two-dimensional systems, and $d\mathbf{x} = dx dy dz$ for three-dimensional systems. In simple, generic models for two-phase fluids, the free energy density for a fluid with uniform composition is often given the simple form

$$F(\phi) = -\alpha\phi^2/2 + \beta\phi^4/4, \quad (13)$$

and the contribution of the composition or density gradient is given the form

$$F'(\nabla\phi) = (c/2)|\nabla\phi|^2 = (c/2)\nabla\phi \cdot \nabla\phi. \quad (14)$$

Equations (11) and (12) can be regarded as Taylor expansions near the critical point, but the simple $(c/2)\nabla\phi \cdot \nabla\phi$ form for the gradient contribution to the free energy functional is commonly used far from the critical point. The coefficient, c , of the “gradient” term in the free energy density is, in general, a function of the order parameter, but it is usually assumed to be a constant.

[14] If the free energy function for a fluid of uniform composition or uniform density has two minima, two phases with different compositions or densities will form over a range of average order parameters. In contrast to the classical fluid-fluid interface model of Young, Laplace, and others, which was based on the idea that the fluid-fluid interface has zero width, the Cahn-Hilliard/Ginzburg-Landau model assumes that the fluid composition varies

continuously over a narrow interface zone [van der Waals, 1893], and models of this type are frequently referred to as diffuse interface models.

[15] The total free energy given by equations (12) and (14) is

$$\mathcal{F} = \int_{\Omega} F[\phi(\mathbf{x})] + \frac{c}{2} \{\nabla\phi(\mathbf{x}) \cdot \nabla\phi(\mathbf{x})\} d\mathbf{x}, \quad (15)$$

and, at equilibrium, the order parameter field, $\phi(\mathbf{x})$, minimizes the total free energy. The first variation of the free energy is given by

$$\delta\mathcal{F} = \int_{\Omega} \{[\partial F(\phi(\mathbf{x}))/\partial\phi(\mathbf{x})]\delta\phi(\mathbf{x}) + c\nabla\phi(\mathbf{x}) \cdot \delta\nabla\phi(\mathbf{x})\} d\mathbf{x}. \quad (16)$$

Integrating the second term in the integral on the right-hand side of equation (16) by parts gives

$$\delta\mathcal{F} = \int_{\Omega} \{\partial F[\phi(\mathbf{x})]/\partial\phi(\mathbf{x}) - c\nabla^2\phi(\mathbf{x})\}\delta\phi(\mathbf{x}) d\mathbf{x}, \quad (17)$$

and $\delta\mathcal{F}$ must be zero for arbitrary perturbations, $\delta\phi(\mathbf{x})$, of the phase field if the system is at equilibrium. Here periodic boundary conditions have been assumed to eliminate surface terms. It follows from equation (17) that the potential associated with the order parameter is given by

$$\mu(\mathbf{x}) = \delta\mathcal{F}/\delta\phi(\mathbf{x}) = \partial F[\phi(\mathbf{x})]/\partial\phi(\mathbf{x}) - c\nabla^2\phi(\mathbf{x}), \quad (18)$$

and the force per unit volume acting on the fluid at position \mathbf{x} due to the potential gradient is given by

$$\mathbf{f}(\mathbf{x}) = -\phi\nabla\mu(\mathbf{x}) = -\phi\nabla\{\partial F[\phi(\mathbf{x})]/\partial\phi(\mathbf{x}) - c\nabla^2\phi(\mathbf{x})\}. \quad (19)$$

At equilibrium, the force, $\mathbf{f}(\mathbf{x})$, in equation (19) is zero. In a flowing fluid, which is not at equilibrium, the order parameter varies slowly with position far from the interface, and the bulk fluid force ($-\phi\nabla\partial F/\partial\phi$) dominates in this region. In the case of a single-component two-phase system (liquid and vapor), where the order parameter is the density, $\phi(\mathbf{x}) = \rho(\mathbf{x})$, the force per unit volume acting on the fluid due to the free energy is given by

$$\begin{aligned} \mathbf{f}(\mathbf{x}) &= -\rho(\mathbf{x})\nabla\mu(\mathbf{x}) = -\rho(\mathbf{x})\nabla\{\partial F[\rho(\mathbf{x})]/\partial\rho(\mathbf{x}) - c\nabla^2\rho(\mathbf{x})\} \\ &= -\rho(\mathbf{x})[\nabla\mu_p(\mathbf{x}) + \nabla\mu_g(\mathbf{x})] = -\nabla P - \rho(\mathbf{x})\nabla\mu_g(\mathbf{x}), \end{aligned} \quad (20)$$

where $\rho(\mathbf{x})\nabla\mu_g(\mathbf{x})$ is the contribution to the force from the gradient contribution to the free energy. It follows from equation (20) that if the effect of the body force, $\mathbf{f}_b(\mathbf{x})$, acting on the fluid is included, the dynamical equation for the fluid is

$$\begin{aligned} \rho(\mathbf{x})d\mathbf{v}(\mathbf{x})/dt &= -\rho(\mathbf{x})\nabla\{\partial F[\rho(\mathbf{x})]/\partial\rho(\mathbf{x}) - c\nabla^2\rho(\mathbf{x})\} + \nabla \\ &\quad \cdot \boldsymbol{\sigma}_\eta + \mathbf{f}_b(\mathbf{x}), \end{aligned} \quad (21)$$

and the acceleration of the fluid is given by

$$d\mathbf{v}(\mathbf{x})/dt = -\nabla\{\partial F[\rho(\mathbf{x})]/\partial\rho(\mathbf{x})\} + c\nabla\nabla^2\rho(\mathbf{x}) + \nabla \cdot \boldsymbol{\sigma}_\eta/\rho(\mathbf{x}) + \mathbf{f}_b(\mathbf{x})/\rho(\mathbf{x}), \quad (22)$$

where $\boldsymbol{\sigma}_\eta$ is the viscous stress tensor. Equation (20) can also be written in the form

$$d\mathbf{v}(\mathbf{x})/dt = \nabla \cdot \boldsymbol{\sigma}_c/\rho + \nabla \cdot \boldsymbol{\sigma}_\eta/\rho + \mathbf{f}_b/\rho, \quad (23)$$

where $\boldsymbol{\sigma}_c$ is the capillary stress tensor. For a single-component fluid, the capillary stress tensor is given by $\boldsymbol{\sigma}_c = [-P + c\rho\nabla^2\rho + (c/2)|\nabla\rho|^2]\mathbf{I} - c\nabla\rho \otimes \nabla\rho$.

[16] With an appropriate choice of the homogeneous free energy density, $F(\rho)$, the strength, c , of the $c(\nabla\rho \cdot \nabla\rho)$ term in the free energy functional, and the density-dependent viscosity, this equation can be used to simulate the dynamics of a single-component liquid-vapor system, and from equation (19) it follows that the equation of motion for a two-component two-phase system is

$$d\mathbf{v}(\mathbf{x})/dt = -\nabla\{\partial F[\phi(\mathbf{x})]/\partial\phi(\mathbf{x})\} + c\nabla\nabla^2\phi(\mathbf{x}) + \nabla \cdot \boldsymbol{\sigma}_\mu/\rho + \mathbf{f}_b/\rho. \quad (24)$$

(The coefficient, c , of the $(c/2)\nabla\phi \cdot \nabla\phi$ term in the free energy functional is given by $(k_B T/6)\int_0^\infty r^2 C^{(2)}(r)dr$, where $C^{(2)}(r)$ is the pair direct two-point correlation function in the uniform fluid [Davis and Scriven, 1982], which can be obtained from molecular dynamics or Monte Carlo simulations. If the free energy functional is expressed in terms of particle number densities and their gradients, this approach can be extended to multicomponent fluids by using the direct correlation functions $C_{ij}^{(2)}(r, \{n\})$ to calculate the coefficient c_{ij} of the $(c_{ij}/2)\nabla n_i \cdot \nabla n_j$ contribution to the free energy functional.)

[17] If a realistic free energy functional is used, the width of the interface is very small (typically on the order of 1 nm, except very near to a critical point), and this approach to computational fluid dynamics can be used only on very small scales since several grid elements must span the interface to provide a reasonably accurate representation of the order parameter profile across the interface. On very small scales, thermally driven fluctuations may also be important, and equation (22) may be replaced with

$$d\mathbf{v}(\mathbf{x})/dt = -\nabla\{\partial F[\phi(\mathbf{x})]/\partial\phi(\mathbf{x})\} + c\nabla\nabla^2\phi(\mathbf{x}) + \nabla \cdot \boldsymbol{\sigma}_\mu/\rho + \zeta_T/\rho, \quad (25)$$

where ζ_T is the rate of the random exchange of momentum due to thermal fluctuations. These fluctuations are conservative (they are a consequence of the momentum-conserving molecular motion).

[18] For a planar interface lying in the (x, y) plane, the equilibrium order parameter profile, $\phi(z)$, that minimizes the free energy can be calculated from equation (18), which can be written in the form

$$dF[\phi(z)]/d\phi(z) - cd^2\phi(z)/dz^2 = 0. \quad (26)$$

(Equation (26) can also be derived by noticing that equation (15) has the same form as the action integral ($I = \int_{t_1}^{t_2} L(q, \dot{q})dt$, where q is a generalized coordinate, $\dot{q} = \partial q/\partial t$, and $L = E_k - E_p$ is the Lagrangian) in classical mechanics. Here E_k is the kinetic energy, and E_p is the potential energy. The free energy functional, $F = F[\phi(\mathbf{x})] + \frac{c}{2}\{\nabla\phi(\mathbf{x}) \cdot \nabla\phi(\mathbf{x})\}$, plays the role of the Lagrangian, $\mathcal{F} = \int_\Omega F^T(\phi, \nabla\phi) d\mathbf{x}$ plays the role of the action integral, and equation (26) is the one-dimensional Euler-Lagrange equation over a fixed volume (which plays the role of the time interval). Minimization of the total free energy, \mathcal{F} , with the mass conservation constraint, $\int_\Omega \rho(\mathbf{x}) d\mathbf{x} = M$, where M is the total mass, can be performed by minimizing $\int_\Omega F^T(\mathbf{x}) d\mathbf{x} - \lambda \int_\Omega \rho(\mathbf{x}) d\mathbf{x}$, where λ is the Lagrange multiplier associated with the mass conservation constraint. This leads to the relationship $dF[\phi(\mathbf{x})]/d\phi(\nabla\mathbf{x}) - c\nabla^2\phi(\mathbf{x}) - \lambda = 0$, and λ is the chemical potential. More generally, this equation can be replaced by $dF[\phi(\mathbf{x})]/d\phi(\nabla\mathbf{x}) - c\nabla^2\phi(\mathbf{x}) + V_{ex}(\mathbf{x}) - \lambda = 0$, where $V_{ex}(\mathbf{x})$ is the external potential.)

[19] Multiplying equation (26) by $d\phi(z)/dz$ gives

$$dF[\phi(z)]/dz - c[d\phi(z)/dz]d^2\phi(z)/dz^2 = 0 \quad (27)$$

or, after integration,

$$F[\phi(z)] = \frac{c}{2} \left[\frac{d\phi(z)}{dz} \right]^2. \quad (28)$$

Equation (28) can be used to obtain the profile of the order parameter, ϕ , and this allows both the surface tension and the width of the interface to be calculated. If the homogeneous free energy density is written in the form $F(\phi) = bf(\phi)$, where $f(\phi)$ is a function that defines the shape of $F(\phi)$ while b defines its magnitude, then it follows from equation (28) that the width, w , scales as

$$w \propto (c/b)^{1/2}. \quad (29)$$

In the absence of the “ $(c/2)\nabla\phi \cdot \nabla\phi$ ” term in the free energy functional a homogeneous continuum fluid described by a free energy, $F(\phi)$, with minima at ϕ_1 and ϕ_2 would separate into two homogeneous phases with order parameters of ϕ_1 and ϕ_2 separated by a sharp interface if $\phi_1 < \bar{\phi} < \phi_2$, where $\bar{\phi}$ is the initial (homogeneous) or average order parameter. The potentials in two phases at equilibrium must be equal ($\mu(\phi_1) = \mu(\phi_2)$), and the surface tension (the excess free energy per unit area of interface relative to the equilibrium free energy of a system with the same mass and average composition but without the gradient term in the free energy functional [Cahn and Hilliard, 1958]) is given by

$$\Gamma = c \int_{-\infty}^{+\infty} (d\phi/dz)^2 dz. \quad (30)$$

The width of the interface in equation (29) is the width of the zone in which most of the change in the order parameter from ϕ_1 to ϕ_2 takes place. For example, if $\phi_2 > \phi_1$, the width

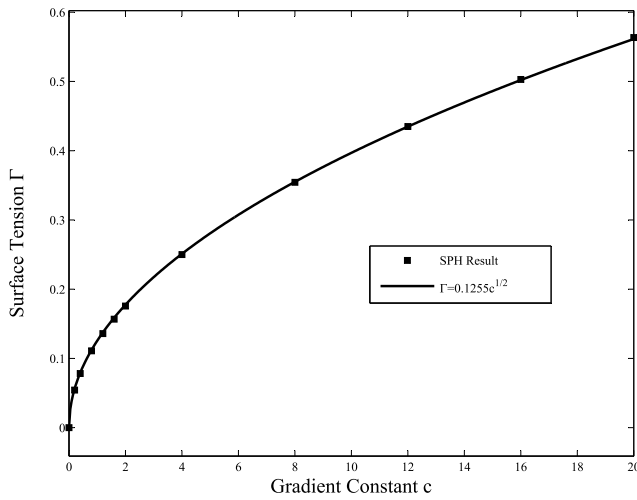


Figure 1. Dependence of the surface tension on the coefficient, c , of the gradient term, $c(\nabla\phi \cdot \nabla\phi)$, in the free energy functional obtained from a one-dimensional smoothed particle hydrodynamics (SPH) simulation [Xu *et al.*, 2009].

of the interface could be defined as the width of the zone in which $\phi_1 + 0.1(\phi_2 - \phi_1) < \phi < \phi_2 - 0.1(\phi_2 - \phi_1)$. Since the width is proportional to $(c/b)^{1/2}$, it follows from equation (19) that

$$\Gamma \propto cw^{-1} \propto c(c/b)^{-1/2} \propto (cb)^{1/2}. \quad (31)$$

Figure 1 shows how the surface tension, determined from the excess surface free energy in a one-dimensional smoothed particle hydrodynamics (SPH, section 9) simulation, depends on the magnitude, c , of the gradient coefficient in the free energy functional (equations (12) and (14)). The homogeneous part of the free energy functional, $F(\phi) = F(\rho)$, was based on a two-phase van der Waals equation of state. The particle positions that minimize the free energy, \mathcal{F} , calculated from the densities and density gradients at all of the particles using the SPH method were found using a conjugate gradient method, and the excess free energy due to the surfaces was calculated from $2F^s = 2\Gamma = \mathcal{F}^{\min} - \mathcal{F}_{\text{hom}}^{\min}$, where \mathcal{F}^{\min} is the minimized free energy and $\mathcal{F}_{\text{hom}}^{\min}$ is the free energy of the corresponding homogeneous system with the same mass calculated from the van der Waals equation of state.

[20] In the absence of the gradient term in the free energy functional the surface tension, Γ , is zero. Minimization of the free energy may still correspond to a phase-separated system if the homogeneous free energy functional has multiple minima and the average fluid composition or density lies between these minima. However, if the surface tension is zero, the fluid-fluid interface will have a complex irregular shape. In real molecular fluids or fluid mixtures, the surface tension approaches zero at the critical point(s), where the minima merge, and phase-separated fluids with a surface (interfacial) tension of zero do not exist.

[21] Equations (11)–(31) describe inhomogeneous systems that can be characterized by a single order parameter.

These include single-component liquid gas systems and two-component “immiscible” liquids that form two liquid phases. In practice, liquids are never completely immiscible (a small amount of liquid 1 dissolves in liquid 2, and a small amount of liquid 2 dissolves in liquid 1 because the entropy of mixing, which has the form $\bar{S}_m = -k_B\rho_n[x_1\ln(x_1) + x_2\ln(x_2)]$, where \bar{S}_m is the entropy of mixing per unit volume, ρ_n is the number density of molecules per unit volume, and x_1 and x_2 are the molar fractions, increases very rapidly as the concentration of the minor component, x_1 or x_2 , increases from zero). In a binary mixture, the order parameter can be defined in a number of ways including $\phi = c_1 - \langle c_1 \rangle$, $\phi = \phi_1^V - \langle \phi_1^V \rangle$, and $\phi = (\phi_1^V - \langle \phi_1^V \rangle) / \langle \phi_1^V \rangle$, where c_1 is the concentration of component 1, ϕ_1^V is the volume fraction of component 1, and $\langle \dots \rangle$ indicates an average over the system.

[22] For more complex systems, more than one order parameter is needed. Under these conditions equations (9)–(22) can be generalized on the basis of the free energy functional

$$F^T(\mathbf{x}) = F[\phi_1(\mathbf{x}), \phi_2(\mathbf{x}) \dots] + F'[\nabla\phi_1(\mathbf{x}), \nabla\phi_2(\mathbf{x}) \dots], \quad (32)$$

where ϕ_i is the i th order parameter (phase field) and F' is a general quadratic form. In general, the order parameters may be associated with conserved or unconserved fields. A fluid system in which both the density and the composition are spatially variable is an important example. In this case, free energy functionals with the form

$$F^T(\mathbf{x}) = F[\phi(\mathbf{x}), \rho(\mathbf{x})] + c_\rho \nabla\rho(\mathbf{x}) \cdot \nabla\rho(\mathbf{x}) + c_\phi \nabla\phi(\mathbf{x}) \cdot \nabla\phi(\mathbf{x}) \quad (33)$$

have been used [Conti, 2001].

[23] Liquids such as water at room temperature have very low compressibilities, and, for the purpose of flow simulations, they can be treated as if they are incompressible under all but extreme conditions. However, compressibility effects can be important in the flow of gases, liquid/gas mixtures, and liquids near the liquid/gas critical point. Under conditions that are sufficiently close to equilibrium, compressibility effects can be calculated from the equation of state $P = f(\rho, T)$, where T is the temperature. The van der Waals equation of state

$$(P + d'/V_m^2)(V_m - b') = k_B T, \quad (34)$$

where V_m is the molecular volume (the volume per molecule), is commonly used because of its simplicity. The van der Waals equation can also be written in the form

$$\left\{ P/P_C + 3 \left/ \left[(V_m/V_m^C)^2 \right] \right\} (V_m/V_m^C - 1/3) = (8/3)T/T_C, \quad (35)$$

where $P_C = d'/(27b'^2)$ is the critical pressure, $T_C = 8a'/(k_B 27b')$ is the critical temperature, and $V_m^C = 3b'$ is the critical molecular volume.

[24] For many, but not all, subsurface applications, the temperature is essentially constant, and a barotropic equation of state can be used. In this review we focus on multiphase fluid flow at constant temperature. However, processes such as boiling, melting, temperature gradient driven Marangoni effects, thermally driven convection, and thermal osmosis [Ten Berge and Bolt, 1988] are important in both natural systems (metamorphic, magmatic, and hydrothermal systems, for example) and geotechnical applications (steam injection for heavy oil recovery, in situ oil shale retorting, geothermal energy, and long-term storage of high-level radioactive waste, for example).

[25] The Helmholtz free energy, $A = U - TS$, where U is the internal energy of the system, S is the entropy, and T is the temperature in Kelvins, is a thermodynamic potential that is minimized at equilibrium under constant temperature conditions. For reversible processes in a closed system

$$dA = -PdV - SdT, \quad (36)$$

and at constant temperature

$$dA = -PdV, \quad (37)$$

so that

$$P = -dA/dV = (\rho^2/m)dA/d\rho, \quad (38)$$

where ρ is the fluid density and m is the mass of fluid or

$$P = -\partial A/\partial V|_{T, \{x_i\}} = \rho^2(\partial \bar{A}/\partial \rho), \quad (39)$$

where \bar{A} is the Helmholtz free energy per unit mass and $\{x_i\}$ is the complete set of compositional variables.

[26] If the van der Waals equation, equation (37), is written in the form

$$(P + a/V_M^2)(V_M - b) = nN_0k_B T = nRT, \quad (40)$$

where V_M is the molar volume, n is the number of moles of the van der Waals fluid, N_0 is the Avogadro number, and R is the universal gas constant, it follows that the Helmholtz free energy per unit volume of homogeneous van der Waals fluid is given by

$$F = (-1/V_M)[RT \ln(V_M - b) + a/V_M] \\ = (\rho/M)\{RT \ln[\rho/(M - b\rho)] - a\rho/M\}, \quad (41)$$

where M is the molecular mass. This expression for the free energy per unit volume can be used in conjunction with a gradient contribution ($c/2(\nabla \rho \cdot \nabla \rho)$) in a phase field model for a single-component two-phase fluid.

[27] For an isothermal fluid with small density gradients (a fluid for which the $c\nabla^2 \phi$ term in the free energy functional and the capillary stress tensor generated by it are

small enough to ignore) the momentum conservation equation can be written in the form

$$d\mathbf{v}(\mathbf{x})/dt = (1/\rho)[- \nabla P(\mathbf{x}) + \nabla \boldsymbol{\sigma}_\eta + \mathbf{f}_b]. \quad (42)$$

Substituting the expression for the pressure given in equation (39) into equation (42) gives

$$d\mathbf{v}/dt = -(1/\rho)\nabla(\rho^2 \partial \bar{A}/\partial \rho) + \nabla(\boldsymbol{\sigma}_\mu)/\rho + \mathbf{f}_b/\rho \\ = -(\partial \bar{A}/\partial \rho)\nabla \rho - \nabla(\rho \partial \bar{A}/\partial \rho) + \nabla(\boldsymbol{\sigma}_\mu)/\rho + \mathbf{f}_b/\rho \quad (43)$$

or

$$d\mathbf{v}/dt = -\nabla \bar{A} - \nabla(\rho \partial \bar{A}/\partial \rho) + \nabla(\boldsymbol{\sigma}_\mu)/\rho + \mathbf{f}_b/\rho. \quad (44)$$

It follows from equation (20) that in the absence of the $c\nabla^2 \phi$ term in the free energy functional

$$d\mathbf{v}/dt = -\nabla(\partial F/\partial \rho) + \nabla(\boldsymbol{\sigma}_\mu)/\rho + \mathbf{f}_b/\rho. \quad (45)$$

Using the relationship $F(\rho) = \rho \bar{A}$ it follows that

$$d\mathbf{v}/dt = -\nabla\{\partial[\rho \bar{A}(\rho)]/\partial \rho\} + \nabla(\boldsymbol{\sigma}_\mu)/\rho + \mathbf{f}_b/\rho \\ = -\nabla(\rho \partial \bar{A}/\partial \rho) - \nabla \bar{A} + \nabla(\boldsymbol{\sigma}_\mu)/\rho + \mathbf{f}_b/\rho, \quad (46)$$

which is identical to equation (42).

3. CONTACT LINES, CONTACT ANGLES, AND WETTING BEHAVIOR

[28] Accurate modeling of multiphase fluid flow in fractured and porous systems depends on an accurate prescription for the behavior of the macroscopic contact angle and its dependence on the velocity of fluid-fluid interfaces adjacent to solid surfaces. The physics of wetting and the dynamics of fluid-fluid-solid contact lines driven across solid surfaces by multiphase fluid flow depend on the coupling between atomic-scale phenomena at the fluid-fluid and fluid-solid interfaces and the fluid-fluid-solid contact line, mesoscale (scales between the atomic and continuum scales) processes, and continuum fluid dynamics.

[29] When the interface between two fluids contacts a smooth solid surface, a simple thermodynamic model predicts that the angle between the fluid-fluid interface and the solid surface measured in fluid 1 is given by

$$\cos(\theta_1) = (\Gamma_{s1} - \Gamma_{s2})/\Gamma_{12}, \quad (47)$$

where Γ_{s1} is the specific interfacial energy (energy per unit area) between the solid and fluid 1, Γ_{s2} is the specific interfacial energy between the solid and fluid 2, and Γ_{12} is the specific interfacial energy between fluid 1 and fluid 2. The equilibrium contact angle given by equation (47) is rarely, if ever, observed. If fluid 1 slowly displaces fluid 2 at the surface of the solid, an “advancing” contact angle, θ_1^a , is measured, and if fluid 2 slowly displaces fluid 1, a receding contact angle, θ_1^r , is measured, and, in general, $\theta_1^a > \theta_1 > \theta_1^r$. If the fluid-fluid interface is not moving, the contact angle

can take a range of history-dependent values, and if the fluid-fluid interface is moving, the advancing and receding contact angles depend on the velocity at which the fluid-fluid interface advances or recedes across the solid surface. A liquid with an “equilibrium” contact angle of $\theta_1 = 0$ (measured in that liquid) is said to be strongly wetting, a liquid with $\theta_1 \leq 90^\circ$ is said to be wetting, and if $\theta_1 > 90^\circ$, the liquid is “nonwetting.”

[30] It is well known that the classical continuum hydrodynamics model, based on the no-slip boundary condition at fluid-solid interfaces, which is very well established for computational fluid dynamics applications to fluid flow in large confined systems (pipelines, fuel tanks, and reactor vessels, for example), cannot be applied at the contact line because of a divergence of the strain rate at the contact line [Dussan V., 1979]. A variety of approaches have been proposed to resolve this nonphysical singularity. For example, one approach is to replace the no-slip boundary condition at fluid-solid boundaries by the Navier slip boundary condition

$$v_s = L_s \dot{\epsilon}_s, \quad (48)$$

where v_s is the fluid velocity at the solid surface, L_s is the slip length, and $\dot{\epsilon}_s$ is the strain rate in the fluid at the surface.

[31] Molecular dynamics simulations indicate that for strongly wetting liquids, the slip length, L_s , is a microscopic length with a value on the order of 1 nm, but for partially wetting and nonwetting liquids the slip length may be much larger (tens of molecular diameters for large contact angles [Barrat and Bocquet, 1999]). Slip effects are negligible if $L \gg L_s$, where L is a length characteristic of the confined system in which flow is taking place (pore diameter or fracture aperture, for example). Consequently, slip effects can be neglected in macroscopic systems, including many subsurface porous media. However, slip effects may be large in nanopores and in molecular dynamics simulations. For example, Majumder *et al.* [2005] have reported that the average flow velocity of liquids in nanotubes may be 10^4 – 10^5 times faster than the velocity predicted using hydrodynamics with no-slip boundary conditions and bulk fluid viscosities. Molecular dynamics simulations also indicate that the slip length may increase as the contact line is approached [Koplik *et al.*, 1988].

[32] A variety of theoretical/computational investigations based on phase field models [Seppecher, 1996; Chen *et al.*, 2000; Jacqmin, 2000], molecular dynamics simulations [Freund, 2003], and lattice Boltzmann simulations [Briant *et al.*, 2004a, 2004b] indicate that evaporation/condensation near the contact line(s) may play a significant role in eliminating the singularity. This mechanism is related to the spatial variation in the curvature of the fluid-fluid interface via the Gibbs-Thompson effect, and it depends on a nonzero vapor pressure or partial miscibility. From a macroscopic phenomenological point of view, the effects of slip at the fluid-solid interface and the effects of evaporation/condensation near the contact are virtually indistinguishable, and we are not aware of any attempts to experimen-

tally determine which process is dominant in specific systems. The phase field model [Seppecher, 1996] predicts that the contact angle depends linearly on the capillary number, and there is no contact angle hysteresis. Heterogeneity would be required to induce hysteresis, and this could change the relationship between the contact angle and the contact line velocity.

[33] An alternative approach [Ruckenstein and Dunn, 1977] is to assume that the fluid at the solid surface is able to migrate diffusively under the influence of a chemical potential gradient along the surface. The slip velocity due to this mechanism is given by the equation

$$v_s = -\mathcal{D}_s \nabla \phi_s / nk_B T, \quad (49)$$

where ϕ_s is the thermodynamic potential of the fluid molecules at the solid surface, \mathcal{D}_s is the surface diffusion coefficient, and n is the particle (molecular) number density.

[34] A variety of experimental investigations and theoretical models are consistent with the idea that the contact angles and fluid interface velocity at the solid surface are related by power laws of the form

$$\begin{aligned} \theta_1^a(v > 0) - \theta_1^a(v = 0) &= av^\alpha \quad \text{or} \quad \theta_1^a(Ca > 0) - \theta_1^a(Ca = 0) \\ &= a'Ca^\alpha, \end{aligned} \quad (50)$$

$$\begin{aligned} \theta_1^r(v = 0) - \theta_1^r(v < 0) &= b(-v)^\beta \quad \text{or} \quad \theta_1^r(Ca = 0) - \theta_1^r(Ca < 0) \\ &= b'(Ca)^\beta, \end{aligned} \quad (51)$$

where v is the velocity at which fluid 1 displaces fluid 2 at the solid surface and Ca is the capillary number given by $Ca = \eta v / \Gamma = \eta |\mathbf{v}| / \Gamma$. For a strongly wetting fluid, equation (50) simplifies to

$$\theta_1^a(v) = av^\alpha = a'Ca^\alpha. \quad (52)$$

Some experimental investigations [Tanner, 1979] and theoretical models based on lubrication theory [Tanner, 1979; de Gennes, 1985] suggest that the exponent, α , has a value of 1/3.

[35] More detailed experimental investigations reveal that the simple power law relationships expressed in equations (50), (51), and (52) are valid over only a limited range of contact line velocities or capillary numbers [Schaffer and Wong, 2000, and references therein], and the values obtained for the exponent, α , relating the contact angle to the contact line velocity cover a quite large range. The experimental evidence for a universal power law relating the contact angle to the contact angle to the velocity is weak at best, and in many systems, there may be no power law. Logarithmic corrections [Eggers and Stone, 2004] may lead to effective exponents that are larger than 1/3, but in some systems the deviation from 1/3 is too large to explain in this manner. Unfortunately, experimental investigations may be strongly influenced by processes that are difficult to detect and control, and this

exacerbates the difficulty of establishing reliable models for contact angle dynamics that can be used in computer simulations. For example, reaction between the fluids and the solid surface may change the roughness of the surface, and impurities present in small concentrations may be adsorbed on the solid surface thus modifying its wetting behavior. In addition, impurities adsorbed on the solid surface may become dissolved or redistributed during the experiment. As a result, the effect of contact line motion on the contact angle is poorly understood. In applications to multiphase flow in geological fractured and porous media, the fluids may have complex compositions, and the solid surfaces are often reactive.

[36] When a strongly wetting fluid with a contact angle of $\theta_1 = 0$ spreads slowly on a flat chemically homogeneous surface, a thin “precursor” film spreads on the surface ahead of the macroscopic contact line [Hardy, 1919; Beaglehole, 1989; Ausserré *et al.*, 1986]. The thin film may be formed by diffusion along the solid surface or evaporation (dissolution) from the advancing liquid phase, and diffusive transport through the receding gas (liquid) phase and condensation on the solid surface may dominate viscous effects for sufficiently small velocities or capillary numbers [Elliott and Riddiford, 1962]. Mineral surfaces exposed to air will adsorb a thin film of water, and this thin film of water may mediate dissolution and precipitation processes [Stipp, 1998].

[37] If the precursor film (or other liquid films on solid surfaces) can be treated as a continuum, the dynamics of the film can be analyzed in terms of the effects of the disjoining pressure Π , which drives the advance of the precursor film, and the viscous and capillary forces, which limit the rate of spreading. The disjoining pressure is often assumed to be given by $\Pi(h) = A/(6\pi h^3)$, where h is the film thickness and A is the effective Hamaker constant [Hamaker, 1937; Lifshitz, 1956] that characterizes the strength of the fluid-solid intermolecular interactions. However, the thickness dependence of Π is determined by the form of the intermolecular interactions. If the external pressure, P_{ext} , and the capillary pressure, $P_c = -\Gamma \nabla^2 h$, due to curvature of the liquid-air interface are included, the pressure in the film is given by

$$P = P_{\text{ext}} - \Gamma \nabla^2 h - \Pi. \quad (53)$$

Assuming that the external pressure is constant, slip effects are negligible, the fluid is incompressible, and the film thickness varies slowly ($\nabla h \ll 1$), the average fluid velocity in a thin film on a flat surface is given by the lubrication theory approximation

$$\mathbf{v}_f = -(h^2/3\eta) \nabla P = (h^2/3\eta) (\nabla \Pi - \nabla P_c), \quad (54)$$

and this leads to the equation

$$\partial h / \partial t = 1/3\eta \nabla [h^3 (\nabla \Pi - \nabla P_c)]. \quad (55)$$

If the effects of gravity are taken into account, this equation becomes

$$\partial h / \partial t = 1/\eta \nabla [h^3 (\nabla \Pi - \nabla P_c - \Delta \rho g z)], \quad (56)$$

where $\Delta \rho$ is the density of the fluid in the film minus the density of the surrounding fluid. The effects of slip at the liquid solid interface can be taken into account by using the Navier slip boundary condition (equation (48)) in conjunction with the equation $\partial^2 \mathbf{v} / \partial z^2 = \nabla P / \eta$ for the velocity profile.

[38] In practice, this lubrication theory approach is quite restricted in its applicability because of the underlying assumptions and approximations. Film flow is a complex phenomenon, and flat films are unstable with respect to a wide variety of spatiotemporal pattern formation processes. Sophisticated numerical methods are required to capture the complexities found in real systems [e.g., Bestehorn and Neuffer, 2001; Gao *et al.*, 2003]. There has been a strong focus on unstable film flow on smooth vertical and inclined surfaces because of a wide range of technological applications. Film flow driven by pressure gradients and/or the effects of gravity acting on density differences can play an important role in subsurface processes [Dragila and Wheatcraft, 2001].

[39] If the precursor film is very thin, the spreading process is driven by the balance of molecular interactions between the fluids and the solid surface and limited by diffusive transport processes. Under these conditions, a theoretical approach based on activated hopping and intermolecular interactions is more appropriate than the application of lubrication theory. Molecular dynamics simulations have been used to investigate thin films and contact line behavior. Most of these simulations have been carried out using fluid particles that interact through a shifted and truncated (finite range) Lennard-Jones potential (equation (3)) at temperatures and pressures that result in the formation of liquid and vapor phases.

[40] The classical contact angle theory expressed in equation (47) is based on continuum concepts and does not take into account the molecular nature of fluids. In general, the contact angle can be expected to vary with distance from the solid surface, even under idealized equilibrium conditions. The behavior of fluids near contact lines is inherently multiscale. One paradigm is a transition from a microscopic contact angle near the solid surface via a curved mesoscale interface to a macroscopic contact angle. In practice, only the macroscopic contact angle is observed in most experiments. For a moving contact line, viscous stresses will modify the shape of the fluid-fluid interface and change the observed macroscopic contact angle. In the microscopic region the concept of a contact angle is questionable because of the molecular structure of the fluids. Very near the solid surface and the fluid-fluid interface the structure and properties of the fluids may differ substantially from those in bulk fluids.

[41] A variety of experimental investigations indicate that both chemical heterogeneity (spatial variation in surface

chemistry) and physical heterogeneity (surface roughness) have a strong impact on contact angle hysteresis [Ramos *et al.*, 2003] and contact line dynamics. As it advances across the solid surface, the contact line becomes temporarily pinned by surface heterogeneity, and this results in hysteresis and complex contact line geometries. While contact angle hysteresis described by equations such as (50) and (51) occurs with atomically flat surfaces, the hysteresis is increased by defects, and more pronounced heterogeneity (surface roughness and chemical heterogeneity) contributes to larger differences between the advancing and receding contact angles. For very rough surfaces, composite wetting phenomena in which small gas phase bubbles are trapped in the “valleys” between asperities behind the advancing contact line and/or small droplets of liquid are stranded as the contact line recedes [de Johnge *et al.*, 1990] are observed. The penetration of a fluid-fluid interface through a porous medium can be described in similar terms, and this process also leads to hysteresis and a complex interface geometry.

[42] The Edwards-Wilkinson equation [Edwards and Wilkinson, 1982] with quenched disorder

$$\partial h(\mathbf{x}, t)/\partial t = a\nabla^2 h(\mathbf{x}, t) + c\{\mathcal{F} + \eta_q[\mathbf{x}, h(\mathbf{x}, t)]\} \quad (57)$$

and the Kardar-Parisi-Zhang equation [Kardar *et al.*, 1986] with quenched disorder

$$\partial h(\mathbf{x}, t)/\partial t = a\nabla^2 h(\mathbf{x}, t) + b[\nabla h(\mathbf{x}, t)]^2 + c\{\mathcal{F} + \eta_q[\mathbf{x}, h(\mathbf{x}, t)]\} \quad (58)$$

have been used as paradigms for the physics of contact line dynamics. These equations are based on the Edwards-Wilkinson and Kardar-Parisi-Zhang equations, which include terms representing temporally fluctuating noise instead of the spatially fluctuating quenched disorder in equations (57) and (58). We refer to equation (57) as the “QEW” equation and to equation (58) as the “QKPZ” equation. Langevin equations of this type have also been applied to a variety of other phenomena including moving charge density waves [Higgins *et al.*, 1993], the dynamics of flux lines in superconductors [Bhattacharya and Higgins, 1993; Hellergvist *et al.*, 1996], magnetic domain walls [Wong and Cable, 1983; Urbach *et al.*, 1995], and the dynamics of fluid-fluid interfaces in porous media [Koplik and Levine, 1985; Delker *et al.*, 1996; Stokes *et al.*, 1988].

[43] Equations (57) and (58) describe the dynamics of a rough line that is driven across a heterogeneous surface or a rough surface or interface that propagates through a random medium. The line, $h(\mathbf{x}, t)$, which is assumed to be a single-valued function that fluctuates about a straight line aligned in the x direction, is the distance that the line has advanced at lateral position x , in the direction of propagation (h) after time t . In equations (57) and (58) the term $a\nabla^2 h(\mathbf{x}, t)$ represents the effect of the force per unit length generated by the curvature of the contact line due to the line tension (analogous to the surface tension force for a curved surface),

\mathcal{F} is the force per unit length (in the x direction) driving the contact line over the surface, and $\eta_q[\mathbf{x}, h(\mathbf{x}, t)]$ is the quenched disorder (random pinning force) due to chemical and/or physical heterogeneity. In equation (58), one possible origin of the term $b[\nabla h(\mathbf{x}, t)]^2$ is a geometric factor that accounts for the fact that a segment of the contact line that propagates with a velocity v in the direction normal to the surface propagates with a velocity of $v[1 + (\nabla h)^2]^{1/2}$ in the overall direction of propagation (in the h direction), where ∇h is the local slope. If the slope is small, the increased velocity in the h direction (the direction of propagation on large scales) has the form $b[\nabla h(\mathbf{x}, t)]^2$, where $b = v/2$. In general, a variety of physical processes can also generate the nonlinear $b[\nabla h(\mathbf{x}, t)]^2$ term [Barabasi and Stanley, 1995; Meakin, 1998], and the sign of b can be positive or negative. In models that can be described by equations like the QKPZ equations, the sign of b can be determined by measuring how the line velocity depends on the slope of the line. In general, the magnitude of the nonlinear term, $|b|$, will be nonzero, and the QKPZ equation will be more relevant. However, if $|b|$ is very small, the early time behavior observed in an experiment or simulation may be described by the QEW equation. The propagation of a fluid-fluid interface through a porous medium can be also be described by the QKPZ equation [Horvath and Stanley, 1995].

[44] If the driving force, \mathcal{F} , is smaller than the critical force, \mathcal{F}_c , required to overcome the quenched disorder, then the contact line will advance through a finite distance given by

$$\xi_{\perp} \propto (\mathcal{F}_c - \mathcal{F})^{-\nu_{\perp}}, \quad (59)$$

before it becomes pinned, and the line is trapped in a metastable state. On scales shorter than the lateral correlation length given by

$$\xi_{\parallel} \propto (\mathcal{F}_c - \mathcal{F})^{-\nu_{\parallel}}, \quad (60)$$

the rough line is a random self-affine fractal [Mandelbrot, 1983; Barabasi and Stanley, 1995; Meakin, 1998]. In equations (59) and (60) the exponents ν_{\perp} and ν_{\parallel} are correlation length exponents. A random self-affine fractal, $h(\mathbf{x})$, is invariant to the transformation

$$h(b\mathbf{x}) \equiv b^H h(\mathbf{x}) \text{ or } b^H h(\mathbf{x}) \equiv h(b\mathbf{x}), \quad (61)$$

where “ \equiv ” should be interpreted as “statistically equivalent to” [Mandelbrot, 1983; Meakin, 1998] and the scaling exponent, H , is the Hurst exponent.

[45] For $\mathcal{F} > \mathcal{F}_c$ the driving force can overcome the pinning forces, and the velocity of the line increases as $\mathcal{F} - \mathcal{F}_c$ increases according to the power law

$$V \propto (\mathcal{F} - \mathcal{F}_c)^{\theta} \quad (62)$$

if $\mathcal{F} - \mathcal{F}_c$ is small [Koplik and Levine, 1985; Tang and Bak, 1988; Nattermann *et al.*, 1993; Narayan and Fisher, 1993]. Under these conditions, the advance of the line is very irregular, parts of the interface become temporarily pinned,

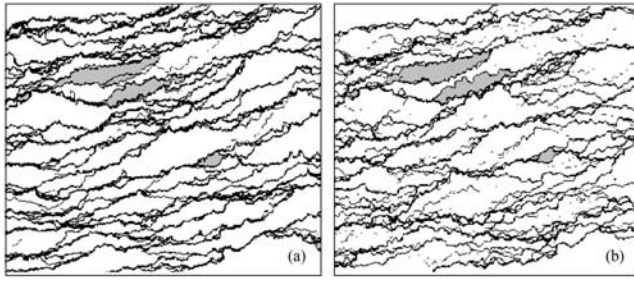


Figure 2. A sequence of pinned helium-4 contact lines on a fabricated rough cesium surface. The contact line propagates from top to bottom. (a) The mean velocity, v , of the contact line is $1.0 \mu\text{m s}^{-1}$, and the contact line is recorded every 0.12 s. (b) The mean velocity is $1.0 \mu\text{m s}^{-1}$, and the contact line is shown every 0.02 s. The shaded areas are “avalanches” (rapid motion of the contact line from one temporarily pinned configuration to the next). Reprinted with permission from *Prevost et al.* [2002], copyright 2002 by the American Physical Society.

and they do not move until they are depinned by changes in adjacent parts of the interface. This behavior is illustrated for an experimental system in Figure 2. As \mathcal{F} is increased, the sizes of the temporarily pinned parts of the interface become smaller, and the motion becomes more regular.

[46] If the line is initially straight, the amplitude of the roughness, $w = [(h - \langle h \rangle)^2]^{1/2}$, will grow as

$$w = \xi_{\perp} \propto t^{\beta}, \quad (63)$$

and the line will be a self-affine fractal on lateral scales up to the lateral correlation length, ξ_{\parallel} , which grows with increasing time as

$$\xi_{\parallel} \propto t^{1/z}. \quad (64)$$

The vertical and lateral correlation lengths are related by

$$w = \xi_{\perp} \propto \xi_{\parallel}^{\alpha}, \quad (65)$$

and the exponents α , β , and z are related by $z = \alpha/\beta$. In most models for the dynamics of self-affine fractal surfaces and interfaces, the exponent α is equal to the Hurst exponent, H (equation (61)), but this is not always the case; a number of models for which $\alpha \neq H$ are known, and for some of these α exceeds the maximum value of H ($H_{\max} = 1$). Experimentally, the roughness exponent has a value of 0.5–0.6 [Prevost et al., 2002; Moulinet et al., 2004].

[47] If $\mathcal{F} - \mathcal{F}_c$ is sufficiently large, the quenched disorder may act like random noise (temporally fluctuating forces) [Kessler et al., 1991], and under these circumstance the ordinary Edwards-Wilkinson or Kardar-Parisi-Zhang (KPZ) equation with fluctuating noise applies. There is also reason to expect that for propagation from an initially straight line, there will be a crossover from QKPZ behavior at early times to KPZ behavior at later times on scales greater than $\xi_{\parallel} \propto t_{*}^{\alpha}$ and $\xi_{\perp} \propto t_{*}^{\beta}$, where t_{*} is the crossover time [Csahok et al., 1993a, 1993b].

[48] If the standard expression for the equilibrium contact angle is replaced by

$$\cos(\theta_1) = (\Gamma_{s1} - \mathcal{F} - \Gamma_{s2})/\Gamma_{12}, \quad (66)$$

then the contact angle at which the contact line begins to advance is given by

$$\cos[\theta_1(\mathcal{F}_c)] = (\Gamma_{s1} - \mathcal{F}_c - \Gamma_{s2})/\Gamma_{12}, \quad (67)$$

and the contact angle for a moving contact line is given by

$$\cos[\theta_1(\mathcal{F} > \mathcal{F}_c)] = (\Gamma_{s1} - \mathcal{F} - \Gamma_{s2})/\Gamma_{12}, \quad (68)$$

so that

$$\cos[\theta_1(\mathcal{F}_c)] - \cos[\theta_1(\mathcal{F})] = (\mathcal{F} - \mathcal{F}_c)/\Gamma_{12}. \quad (69)$$

This equation, with equation (62), indicates that

$$\cos[\theta_1(\mathcal{F} > \mathcal{F}_c)] = \cos[\theta_1(\mathcal{F} = \mathcal{F}_c)] + cV^{1/\theta}. \quad (70)$$

Using equation (70) and the identity

$$\cos(A) - \cos(B) = -2 \sin[(A+B)/2] \sin[(A-B)/2] \quad (71)$$

with equation (60) indicates that

$$\theta_1(\mathcal{F} > \mathcal{F}_c) = \theta_1(\mathcal{F}_c) + c'V^{1/\theta} \quad (72)$$

if V is small and the contact angle $\theta_1(\mathcal{F}_c)$ is not too small. This is a commonly used empirical expression for the velocity-dependent contact angle. Another commonly used expression is

$$\cos[\theta_1(\mathcal{F}_c)] - \cos[\theta_1(\mathcal{F} > \mathcal{F}_c)] = c''V^{1/\theta}, \quad (73)$$

which can be obtained directly from equations (62) and (66). While it is clear that this simple analysis is at best a “toy model,” it does suggest that a stochastic differential equation approach to contact line dynamics may be consistent with experimental observations.

[49] If the pinning forces are selected at random from a finite distribution (no very large pinning forces) and there are no long-range spatial correlations, the roughness exponent α in the equation $w = \xi_{\perp} \propto \xi_{\parallel}^{\alpha}$, has a value of about 0.63, and the exponent β in equation (58) also has a value of about 0.63 [Tang and Leschorn, 1992; Buldyrev et al., 1992] for a line that is driven by a force that is a little larger than \mathcal{F}_c . The QKPZ process is closely related to directed percolation [Tang et al., 1995], and the exponents are given by $\alpha = \beta = \theta = \nu_{\perp}/\nu_{\parallel}$, where ν_{\perp} and ν_{\parallel} are the perpendicular and parallel correlation length exponents ($\xi_{\perp} \propto (p - p_c)^{-\nu_{\perp}}$ and $\xi_{\parallel} \propto (p - p_c)^{-\nu_{\parallel}}$), where p is the fraction of filled sites and p_c is the fraction of filled sites at the directed percolation threshold [Buldyrev et al., 1992]. The numerical values of the directed percolation exponents are known quite accurately ($\nu_{\perp} = 1.09684 \pm 0.00002$ and $\nu_{\parallel} = 1.73383 \pm 0.00003$ [Jensen, 1996]) so

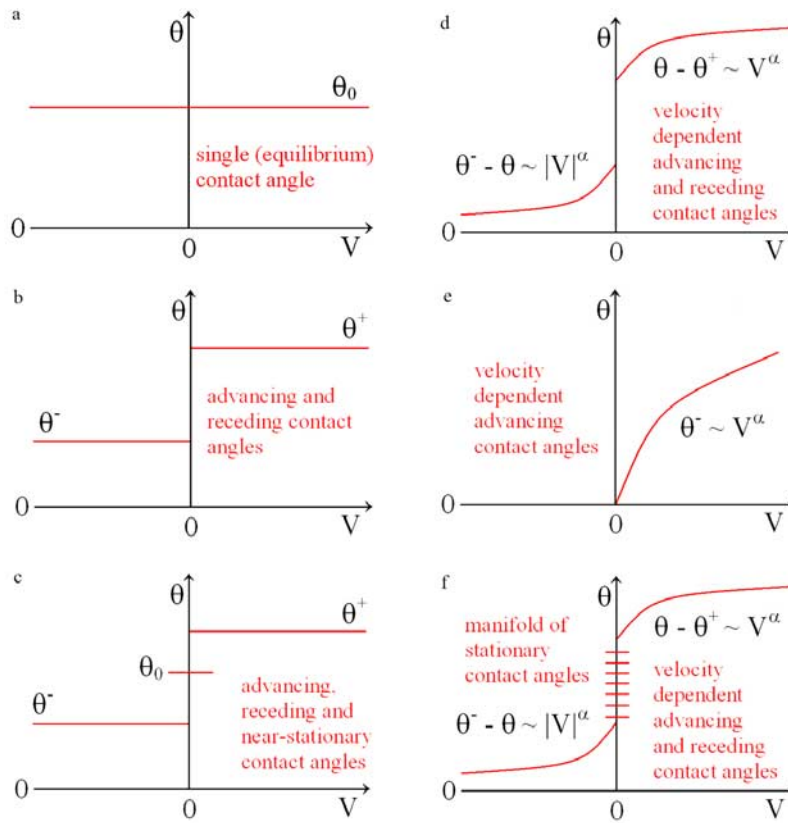


Figure 3. Contact angle models: (a) classical (equilibrium) single contact angle model, (b) two-angle (advancing and receding contact angle) model, (c) three-angle (advancing, receding, and near-equilibrium contact angle) model, (d) velocity-dependent advancing and receding contact angle model for a liquid that does not strongly wet the solid (a separate near-equilibrium contact angle can be added), (e) velocity-dependent advancing contact angle model for strongly wetting fluid (the contact angle is zero for stationary and receding contact lines), and (f) velocity-dependent advancing and receding contact angle with a manifold of metastable stationary states for liquid that does not strongly wet the solid.

that $\alpha = \beta = \theta = \nu_{\perp}/\nu_{\parallel} = 1.09684 \pm 0.00002/1.73383 \pm 0.00003 \approx 0.63$. For the QEW process $\alpha = 1$, $\beta = 0.75$, and $\theta = 0.33$ [Narayan and Fisher, 1993].

[50] In general, the correlation length exponents, ν_{\parallel} and ν_{\perp} , the Hurst exponent, H , the roughness exponent, α , and the exponent, θ , relating the velocity of propagation to the excess driving force, $\mathcal{F} - \mathcal{F}_c$, depend on the value of the coefficient, b , of the nonlinear $[\nabla h(x, t)]^2$ term, the strength and spatial correlations of the pinning forces, $\eta_q[\mathbf{x}, h(\mathbf{x}, t)]$, and the isotropy or anisotropy of the quenched disorder. Of course, the real situation is much more complicated, and the QKPZ equation must be modified to more accurately describe contact line dynamics. For example, in some cases, thermal fluctuations may be sufficient to depin the contact line, and an additional noise term, $\eta(\mathbf{x}, t)$, may be needed on the right-hand side of equations (57) and (58) to represent the thermal fluctuations. In addition, the driving force, \mathcal{F} , will not be constant in typical surface multiphase fluid flow processes. The QEW and QKPZ equations are invariant to the transformation $h(\mathbf{x}, t) \rightarrow -h(\mathbf{x}, t)$, but it is clear that real contact line dynamics are not invariant to this transformation unless the contact angle is $\pi/2$. The behavior expressed in equations (62) and (63) and the other scaling relation-

ships presented above appears to be generic, even though the exponents do depend on model details. In practice, it is difficult to obtain accurate values for the exponents using either experimental methods or computer simulations, and theoretical methods often do not provide exact values for the exponents. Consequently, substantial ambiguity remains.

[51] A model for the dynamics of the contact line and contact angle is required for grid-based continuum model simulations of multiphase fluid flow in confined systems. In principle, coupled molecular dynamics–continuum models can be used. Although the time steps used in the molecular and continuum parts of the model can be decoupled [Hadjiconstantinou, 1999], this approach is not practical because of the extremely small time steps required in the molecular component. It might also be possible to couple continuum fluid dynamics models with a Langevin equation for the contact line dynamics, such as equation (57) or (58), but simpler approaches are needed for most scientific and practical applications, and Figure 3 shows some relatively simple models for the velocity dependence of the contact line. All of these models, except for that illustrated by Figure 3f, have been used in grid-based continuum model

simulations of the behavior of multiphase fluids in contact with solid surfaces. The model illustrated in Figure 3f includes a manifold of metastable states with different contact angles. A finite number of metastable contact angles, which would be selected at random, could be used, or the metastable contact angle could be randomly selected from a continuous distribution. However, experiments performed with heterogeneous surfaces [e.g., *Cubaud and Fermigier*, 2004] indicate that the contact angle, near the contact line, varies with position along the contact line, and this should be taken into account in three-dimensional simulations. Because wetting behavior is often difficult to describe in quantitative terms, the models illustrated in Figure 3 have been used more to investigate the impact of various wetting behaviors on multiphase fluid flow in confined systems than to predict the behavior of specific systems of scientific interest or practical importance.

4. PORE NETWORK MODELS

[52] In pore network models, the complex pore space geometry of most rocks and soils is replaced by a network of pore volumes connected by channels. In these models, both the pore volumes and the connecting channels have simplified geometries, and it is usually assumed that the capillary and viscous forces associated with the pore volumes are negligible (relative to the capillary and viscous forces in the channels). For the most simple models, the pore volumes are located at the nodes of a regular lattice, and the channels have circular cross sections. Although most pore network models are based on regular lattices, the “lengths” of the channels (pore throats) connecting the pore volumes, used to calculate channel volumes and fluid conductivities, may not be equal to the Pythagorean distances measured in the embedding space between the nodes that they connect [*Fenwick and Blunt*, 1998]. Voronoi tessellations [*Fenwick and Blunt*, 1998], Delaunay triangulations [*Blunt and King*, 1990], and a variety of other irregular networks [*Lowry and Miller*, 1995] have also been used. Both the pore volumes and channel radii can be selected randomly from prescribed distributions. In more complex models, other pore and channel geometric characteristics and the pore positions may also be randomly selected from appropriate distributions. An alternative approach is to select the pore volumes, channel lengths, channel radii, and other characteristics to match, as well as possible experimentally determined pore space geometries [*Oren et al.*, 1998; *Patzek*, 2001; *Bakke and Oren*, 1997; *Tsakiroglou and Payatakes*, 2000]. The required three-dimensional digital images of pore space geometries can be obtained from high-resolution three-dimensional X-ray tomography or NMR tomography experiments. Reconstruction of the three-dimensional pore volume from a stack of two-dimensional cross-sectional digital images [*Lin and Cohen*, 1982; *Holt et al.*, 1996] can also be used, but this approach is much more laborious [*Patzek*, 2001].

[53] In some cases, the model is simplified even further. For example, in the case of the invasion percolation model

[*Wilkinson and Willemsen*, 1983] for the displacement of a wetting fluid by a nonwetting fluid in a porous medium it is assumed that the nonwetting fluid always advances through the channel (pore throat) with the smallest opposing capillary pressure difference (the largest throat diameter). In this case, only the pore throat diameter or capillary invasion pressure associated with each bond (channel) in the network is needed to fully define the model. The invasion percolation model is based on the idea that if the flow rates are small enough, the effects of fluid viscosity on the displacement of a wetting fluid by a nonwetting fluid in a porous medium can be neglected. However, it is not clear that the slow flow limit can be reached because of the relatively rapid fluid motion that occurs when the fluid-fluid interface penetrates a pore throat and the energy that is stored in other part of the fluid-fluid interface drives the fluid into the newly accessible pore volume(s), a process often referred to as a Haines jump [*Haines*, 1930]. Simplification is also possible if the fluid-fluid displacement is fast, and capillary effects can be neglected. In the limit in which a viscous fluid is very rapidly displaced by a nonviscous fluid (i.e., very large viscosity ratio), the fluid-fluid displacement process can be simulated by models based on the diffusion limited aggregation (DLA) model [*Witten and Sander*, 1981; *Paterson*, 1984], and in the limit in which a viscous fluid displaces a nonviscous fluid anti-DLA models [*Paterson*, 1984] can be used. Many variants of these simple models have been developed [e.g., *Meakin*, 1991, 1998; *Glass et al.*, 1998; *Vedvik et al.*, 1998]. Realistic pore network models for fluid-fluid displacement should be able to simulate both the DLA and invasion percolation limits, and this has been demonstrated in practice [*Ferer et al.*, 2003].

[54] In most pore network models, the physics of the processes taking place in the idealized porous medium is also simplified [*Blunt and King*, 1990], and information from experiments [*Lenormand et al.*, 1983] or computer models based on conservation principles and more rigorous physics (like those discussed in sections 5–10) is used. If the porous medium is saturated with a single fluid and the resistance to flow in the pores volumes can be neglected because the diameters of the pores are much greater than the diameters of the channels, the pore network model can be represented by pore volumes, $\{V_i\}$, with pressures, $\{P_i\}$, or hydraulic potentials, $\{\Phi_i\}$, connected by channels that control fluid flow through viscous forces. If a channel is completely filled with a single fluid, the flow rate along the channel from pore i to pore j is given by

$$Q_{ij} = S_\eta (\Phi_i - \Phi_j) r_{ij}^4 / (l_{ij} \eta) = G_{ij} (\Phi_i - \Phi_j), \quad (74)$$

where S_η is a shape factor, r_{ij} is the radius of the channel between pore i and pore j , l_{ij} is the channel length, and G_{ij} is the channel mobility or the fluid conductance of the channel. In equation (74), Φ_i is the hydraulic potential, $\Phi_i = P_i + \rho g h_i$, in pore i , where h_i is the coordinate of pore i in

the direction of the gravitational field. If the fluids are incompressible,

$$\sum_i Q_{ij} = 0 \quad \text{and} \quad \sum_j Q_{ij} = 0 \quad (75)$$

for interior pores, which is equivalent to Kirchhoff's equation [Kirchoff, 1845] for a resistor network, and the solution of the flow equation is equivalent to solving a resistor network problem where the electric potentials at the nodes are replaced by the fluid potentials or pressures (for a horizontal two-dimensional network or a network in which the pressure gradient is much larger than the gravitational potential gradient) in the pore volumes and the resistance is replaced by $l_{ij}\eta/S_\eta r_{ij}^4$.

[55] From a practical point of view, the outstanding challenge for single-phase fluid flow applications is to find a reasonably accurate way of representing real porous media by a pore network model. In this review we focus on multiphase fluid flow and reactive transport.

[56] For multiphase fluids, the effects of the capillary pressure jump across fluid-fluid interfaces must be taken into account. In simple pore network models for two-phase fluid flow, one fluid is often assumed to displace the other in a piston-like manner, and, if the effects of gravity acting on the fluid densities can be neglected, equation (74) is replaced by

$$Q_{ij} = S_\eta (P_i - P_j - \Delta P_{ij}^c) r_{ij}^4 / (l_{ij}^{(i)} \eta_i + l_{ij}^{(j)} \eta_j) \quad (76)$$

for a pore that contains a single meniscus. Here ΔP_{ij}^c is the capillary pressure jump across the fluid-fluid interface in the channel connecting pore i and pore j , η_i and η_j are the viscosities of the fluids in the segments of the channel adjacent to pore i and pore j , and $l_{ij}^{(i)}$ and $l_{ij}^{(j)}$ are the corresponding segment lengths. In general, the capillary pressure jump across a fluid-fluid interface is given by

$$\Delta P_c = \Gamma(\kappa_1 + \kappa_2) = \Gamma\mathcal{K}, \quad (77)$$

where κ_1 and κ_2 are the principal curvatures and the pressure is largest on the concave side of the interface. For a channel with a circular cross section $\kappa_1 = \kappa_2 = \cos(\theta)/r$, where r is the channel radius and θ is the contact angle (in some models, the radius varies along the channel). If the hydraulic potential difference, $\Phi_i - \Phi_j$, is not large enough to overcome the capillary entry pressure, the fluid-fluid interface will not enter the channel connecting pores i and j . If the effect of gravity acting on the fluid densities is important, equation (76) must be modified to

$$\begin{aligned} Q_{ij} &= S_\eta (\Phi_i - \Phi_j - \Delta P_c) r_{ij}^4 / (l_{ij}^{(i)} \eta_i + l_{ij}^{(j)} \eta_j) \\ &= S_\eta (P_i - P_j - \Delta P_{ij}^g - \Delta P_{ij}^c) r_{ij}^4 / (l_{ij}^{(i)} \eta_i + l_{ij}^{(j)} \eta_j), \end{aligned} \quad (78)$$

where

$$\Delta P_{ij}^g = g(\rho_i h_{ij}^{(i)} + \rho_j h_{ij}^{(j)}). \quad (79)$$

In equation (79), ρ_i is the density of the fluid in pore i , ρ_j is the density of the fluid in pore j , $h_{ij}^{(i)} = h_{ij} l_{ij}^{(i)} / l_{ij}$, and $h_{ij}^{(j)} = h_{ij} l_{ij}^{(j)} / l_{ij}$. Here $h_{ij} = h_j - h_i$ is the difference in height (distance in the direction of the gravitational field) between pores j and pore i .

[57] Pore network models are completed by the boundary conditions, which include periodic boundary conditions for gravity-driven flow, pressure (potential) boundary conditions, and flux boundary conditions. In the case of single-phase fluid flow, the Kirchhoff equation obtained from equations (74) and (75) is

$$\sum_j G_{ij} (\Phi_j - \Phi_i) = 0. \quad (80)$$

In most applications this equation is solved for the potentials, $\{\Phi_i\}$, using a successive overrelaxation algorithm such as

$$\Phi_i = \gamma \left(\sum_j G_{ij} \Phi_j / \sum_j G_{ij} \right) - (1 - \gamma) \Phi_i, \quad (81)$$

where γ is the overrelaxation parameter or a conjugate gradient method.

[58] If the flow rates, $\{Q_i\}$, into the boundary nodes (pores) are specified, the Kirchhoff equation can be written in the form

$$\mathbf{G}'' \Phi = -\mathbf{Q}, \quad (82)$$

where the vector Φ contains the required potentials and the vector \mathbf{Q} contains the imposed flow rates into the boundary nodes (pore volumes). The off-diagonal elements of \mathbf{G}'' are the conductances, and the diagonal elements are given by $G''_{ii} = -\sum_{j \neq i} G_{ij}$. In general, \mathbf{G}'' is a sparse symmetric matrix. It follows from equation (82) that the potentials at the internal nodes are given by

$$\Phi = \mathbf{G}''^{-1} \mathbf{Q}. \quad (83)$$

Equation (82) can be solved by matrix inversion (equation (83)), conjugate gradient methods, Gaussian elimination, or a variety of other methods. A similar approach [Aker et al., 1998] can be used if the potentials in the boundary nodes are specified. In this case

$$\mathbf{D} \Phi_I = \mathbf{B}, \quad (84)$$

where the vector \mathbf{B} contains the boundary hydraulic potentials, Φ_I contains the required interior potentials, the matrix \mathbf{D} is obtained from the channel conductances, and

$$\Phi_I = \mathbf{D}^{-1} \mathbf{B}. \quad (85)$$

(The Kirchhoff equation can be expressed as $\sum_{j \neq i} G_{ij} \Phi_j = \sum_{k \neq i} G_{ik} \Phi_k$, where the subscript i indicates an internal node and the index k indicates both internal and boundary nodes. This equation can be written in the form $\Lambda \Phi_I = \mathbf{G}_B \mathbf{B} + \mathbf{G}_I \Phi_I$, where Λ is an $N_I \times N_I$ diagonal matrix

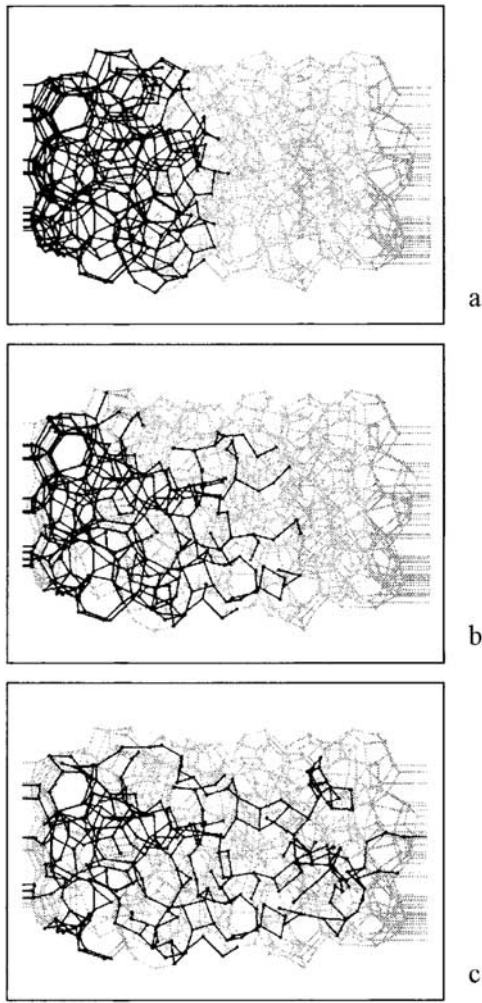


Figure 4. Pore network simulations of immiscible displacement at capillary numbers of (a) 0.3, (b) 0.003, and (c) 0.0003. The ratio between the viscosities of the displacing and displaced fluids was 0.5. The network model was based on 903 pores (Delaunay cells) constructed in the interior of a packing of 1500 spheres with a distribution of diameters (the standard deviation was 1/4 of the mean diameter). The darker lines represent bonds that have been invaded by displacing fluid. Reprinted with permission from *Thompson and Fogler* [1998], copyright 2006 by the American Physical Society.

($\Lambda_{ii} = \sum_{j \neq i} G_{ij} \Phi_j$), Φ_I is a vector consisting of the N_I internal potentials that must be determined, \mathbf{G}_I is an $N_I \times N_I$ matrix whose elements are the conductances of the channels connecting interior nodes, \mathbf{B} is a vector consisting of the N_B boundary potentials, and \mathbf{G}_B is an $N_B \times N_I$ matrix consisting of the conductances of the channels linking boundary and interior nodes. The Kirchhoff equation, $\Lambda \Phi_I = \mathbf{G}_B \mathbf{B} + \mathbf{G}_I \Phi_I$, can be written as $\Phi_I = (\Lambda - \mathbf{G})^{-1} \mathbf{G}_B \mathbf{B} = \mathbf{D} \mathbf{B}$.) Once the internal hydraulic potentials have been determined, the flow rates may be obtained from equations (74), (76), or (78).

[59] For two-phase systems, the simulation consists of a large number of small steps in which the positions of the fluid-fluid interfaces in each channel and the contents of all of the pores are updated using the flow rates calculated from

the hydraulic potential differences. Calculation of the pressures is based on a quasi-stationary approximation (the time scale for equilibration of the pressure is much smaller than the time scale for motion of the fluid-fluid interfaces) using the Kirchhoff equation

$$\sum_j G_{ij} (P_j - P_i - \Delta P_{ij}^g - \Delta P_{ij}^c) = 0, \quad (86)$$

which can also be rearranged to the form given in equation (84), $\mathbf{P} = \mathbf{D}^{-1} \mathbf{B}$, where \mathbf{P} is a vector formed from the pressures in the interior nodes and \mathbf{B} is a vector formed from the boundary pressures and the pressure differences, $\Delta P_{ij}^g + \Delta P_{ij}^c$. Simulations can also be carried out with injection rate boundary conditions [Aker *et al.*, 1998], and pore network models have also been used to simulate three-phase fluid flow in porous media [e.g., Pereira, 1999; van Dijke and Sorbie, 2003].

[60] Figure 4 illustrates immiscible flow simulations in a three-dimensional pore network for three different capillary numbers [Thompson and Fogler, 1998]. These simulations show that the front between the two fluids becomes broader as the capillary number is decreased.

[61] If one of the two fluids strongly wets the mineral surfaces, it may form a continuous film on the surface and fill crevices and grooves. In the invasion percolation model, it is assumed that this wetting film allows the wetting fluid to escape from regions that are surrounded by nonwetting fluid, and the nonwetting fluid is allowed to invade these trapped regions. When this wetting film does not exist, or the film is so thin that film flow can be ignored, the “invasion percolation with trapping” model is used, and once a region has been surrounded by nonwetting fluid, no further invasion into that region is allowed. These two models give very similar results in three-dimensional simulations, but in two-dimensional systems, the fractal dimensionality of the pore space occupied by the invading nonwetting fluid is different for invasion percolation and invasion percolation with trapping. In pore network models, this behavior can be taken into account by allowing both fluids to simultaneously occupy the same segment of a channel, and in some cases the channels are assumed to have polygonal cross sections or cross sections consisting of arc segments that are convex to the fluids and contact at acute angles. In addition, the channel cross section (diameter) may vary along its length [Al-Gharbi and Blunt, 2005]. In a model of this type, the shape factors, S_{η} , for the phases that coexist in the same channel depend on the pressure difference between the two fluids.

[62] Processes other than fluid flow can be included in pore network models. For example, vapor phase diffusion has been included in drying models [Yiotis *et al.*, 2006], the dissociation of methane hydrate has been included in simulations of the release of methane from porous media containing methane hydrate [Tsimpanogiannis and Lichter, 2006], and pore shrinkage has been included in models for the desaturation of deformable soils [Simms and Yanful, 2005].

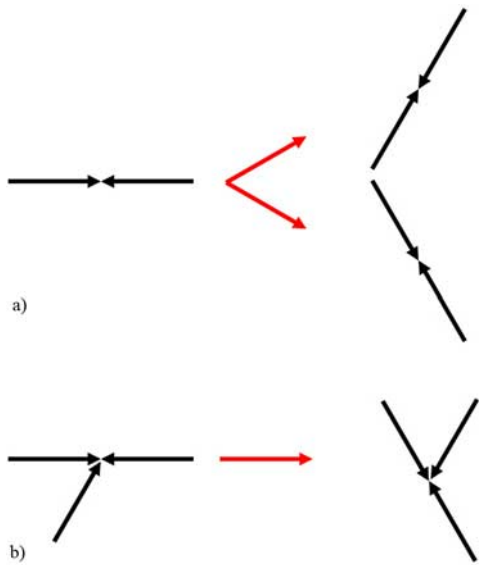


Figure 5. (a and b) Some of the momentum-conserving collisions allowed in a lattice gas model on a triangular lattice. In Figure 5a, two collisions are allowed, and they are selected randomly with equal probability.

[63] Because fluid flow can be simulated for large pore networks (networks consisting of many pore volumes and channels), pore network models have been used to evaluate the validity of concepts and equations used in large-scale models such as reservoir simulators [Fatt, 1956a, 1956b, 1956c; Blunt and King, 1990; Blunt *et al.*, 2002]. This approach can also be used to determine parameters for large-scale continuum models [e.g., Bryant and Blunt, 1992]. However, the value of pore network model simulations for these purposes is limited by the approximations and simplifications used in the pore network models.

[64] The rapidly increasing capabilities of high-performance computing systems will enable pore network simulations to be carried out on much larger scales, but these advances will also allow other methods that are more firmly based on first principles to be implemented and allow the full complexity of pore space geometries revealed by high-resolution X-ray tomography to be taken into account [Spanne *et al.*, 1994]. (For example, a pore network model implemented on a very large parallel computing system using an algorithm that scales well as the number of processing elements increases would allow simulations with $O(10^9)$ pores to be performed (depending on the complexity of the model). The number of pores in a typical core sample may be smaller than this, depending on the characteristic pore size in the rock sample.) Pore network models for multiphase fluid flow may be complex and include a quite large number of invasion and imbibition processes. Very often, they are not described in a completely unambiguous manner in the scientific literature, and this makes it difficult to reproduce them independently. In addition, a substantial effort is required to develop and validate the more complex pore network models. The simulation of single-phase fluid flow in pore spaces obtained by X-ray tomography or pore

spaces “reconstructed” from a limited number of cross sections (planar cuts [Yeong and Torquato, 1998]) is now relatively routine, and simulation of multiphase fluid flow on realistically complex three-dimensional pore spaces is also being used more extensively.

5. LATTICE GAS AND LATTICE BOLTZMANN MODELS

[65] In lattice gas models [Frisch *et al.*, 1986; D’Humières *et al.*, 1986] particles move synchronously from node to node on a regular Bravais lattice (a lattice in which all nodes are identical) and undergo momentum-conserving collisions (Figure 5). Sometimes more than one momentum-conserving collision (defined by the particle directions before and after the collision) is possible for the same incoming particle directions, and in this event one of the possible momentum-conserving collisions is selected randomly. Because of the simplicity of lattice gas models, which can often be implemented on a computer using fast logical operations, the microdynamics of a large number of particles can be followed through a large number of collisions, and because of their discrete nature, lattice gas models are not susceptible to numerical instability. However, these advantages are offset by the stochastic nature of the model, which requires averaging over a quite large number of neighboring particles to obtain an accurate fluid velocity field, and this requires a very large lattice to simulate complex flow fields. Lattice gas models also violate Galilean invariance. Multicomponent, multiphase fluids can be simulated by assigning distinct “labels” to the particles, according to the component that they represent, and modifying the collision rules so that particles are directed toward sites containing particles with the same label (in the direction of the concentration gradient) [Rothman and Zaleski, 1994].

[66] Lattice gas models have also been used to simulate dissolution and precipitation. For example, in the model of Wells *et al.* [1991], the solute concentration is defined on the nodes of the lattice. When a particle moves from one node to an adjacent node, it carries with it the concentration at the node of origin, and in the collision step, the concentrations of the particles arriving at each of the nodes are averaged. If a particle, representing the fluid, reaches a solid node, mass is exchanged between the solid and fluid nodes, and the amount of mass exchanged is a nonlinear function of the concentration carried by the fluid particle (either precipitation or dissolution can occur, depending on the supersaturation or undersaturation). A record is kept of the mass transfer at each of the surface nodes, and when the accumulated precipitation or dissolution has reached a threshold value, the solid node is converted to a liquid node, or the liquid node becomes a solid node.

[67] The major deficiencies of lattice gas models (noisy small-scale dynamics and lack of Galilean invariance) can be overcome by using a mesoscale lattice Boltzmann model in which the amount of fluid associated with each lattice node is large enough to suppress the effects of fluctuations

through averaging, and lattice gas models have been superseded by lattice Boltzmann models for most applications. One approach to the development of lattice Boltzmann models is based on a corresponding lattice gas model [McNamara and Zanetti, 1998]. The idea behind this approach is to replace the velocities of individual particles by a velocity distribution function, $f_i(\mathbf{x}, t)$, the population of particles moving in the i th direction, with velocity \mathbf{v}_i , at position \mathbf{x} at time t .

[68] The second approach [Higuera and Jimenez, 1989] is to discretize the Boltzmann equation

$$\partial f(\mathbf{v}, \mathbf{x}, t) / \partial t = -\mathbf{v} \cdot \nabla f(\mathbf{v}, \mathbf{x}, t) - (\mathbf{F} / \rho) \cdot \partial f(\mathbf{v}, \mathbf{x}, t) / \partial \mathbf{v} + \Omega_R[f(\mathbf{v}, \mathbf{x}, t)] \quad (87)$$

for the evolution of the particle velocity distribution field. In equation (87) $f(\mathbf{v}, \mathbf{x}, t) \delta \mathbf{x} \delta \mathbf{v}$ is the number density of particles with positions in the range \mathbf{x} to $\mathbf{x} + \delta \mathbf{x}$ and velocities in the range \mathbf{v} to $\mathbf{v} + \delta \mathbf{v}$ at time t (in the $\delta \mathbf{x} \rightarrow 0$ and $\delta \mathbf{v} \rightarrow 0$ limit), \mathbf{F} is the force per unit volume acting on the fluid, and Ω_R represents the effects of collisions (relaxation). In lattice Boltzmann models, the distribution function, $f(\mathbf{v}, \mathbf{x}, t)$, is represented by the population densities $\{f_i(\mathbf{x}, t)\}$ of a velocity vector basis set, $\{\mathbf{e}_i / \Delta t\}$, or the corresponding distance vector basis set, $\{\mathbf{e}_i\}$, at each of the nodes on the lattice. The Boltzmann equation is replaced by an equation for the evolution of the populations $\{f_i(\mathbf{x}, t)\}$ due to particle streaming from node to node and relaxation of the populations at the nodes. If Δt is the time required for the population $f_i(\mathbf{x}, t)$ to be transported from the node at position \mathbf{x} to $\mathbf{x} + \mathbf{e}_i$, where $\mathbf{e}_i = \mathbf{v}_i \Delta t$, then the discretized version of equation (87) is

$$f_i(\mathbf{x} + \mathbf{e}_i, t + \Delta t) = f_i(\mathbf{x}, t) + \Delta^F f_i + \Delta^R f_i, \quad (88)$$

where $\Delta^F f_i$ is the change in $f_i(\mathbf{x}, t)$ due to external forces acting on the fluid and $\Delta^R f_i$ is the effects of molecular collisions that relax the discretized distribution function $\{f_i(\mathbf{x}, t)\}$ toward the equilibrium Maxwell-Boltzmann distribution function for a fluid moving with the local velocity $\mathbf{u}(\mathbf{x})$.

[69] In most cases, it is assumed that $\Delta^R f_i$ has the single relaxation time BGK [Bhatnagar *et al.*, 1954] form

$$\Delta^R f_i = (f_i^{eq} - f_i) / \tau, \quad (89)$$

where τ is the relaxation time and $f_i^{eq} = f_i^{eq}[\mathbf{u}(\mathbf{x})]$ is the equilibrium value of f_i , and, in the absence of a body force, the microdynamics of the lattice Boltzmann model is defined by the equation

$$f_i(\mathbf{x} + \mathbf{e}_i, t + \Delta t) = f_i(\mathbf{x}, t) + [f_i^{eq} - f_i(\mathbf{x}, t)] / \tau. \quad (90)$$

The Maxwell-Boltzmann distribution is given by

$$f^{MB}(\mathbf{v}) = \frac{m}{(2\pi k_B T)^{D/2}} \exp \left[-\frac{(\mathbf{v} - \mathbf{u})^2}{2k_B T} \right], \quad (91)$$

where m is the particle mass and $f(\mathbf{v}) \delta \mathbf{v}$ is the probability that a particle will have a velocity between \mathbf{v} and $\mathbf{v} + \delta \mathbf{v}$ ($\delta \mathbf{v} \rightarrow 0$). In lattice Boltzmann models, the Maxwell-Boltzmann distribution is replaced by a discretized approximation, $\{f_i^{eq}\}$, that conserves momentum [He and Luo, 1997]. The most simple momentum-conserving discretization is

$$f_i^{eq} = w_i \rho \left[1 + \frac{\mathbf{e}_i \cdot \mathbf{u}}{c_s^2} + \frac{(\mathbf{e}_i \cdot \mathbf{u})^2}{2c_s^2} - \frac{\mathbf{u} \cdot \mathbf{u}}{2c_s^2} \right], \quad (92)$$

where c_s is the sound velocity, $\rho = \sum_i f_i$ is the fluid density, and w_i is the weight of the i th basis vector. The sound velocity is given by $c_s^2 = k_B T / m$. Higher-order momentum-conserving expansions can be used [Gonzalez-Segredo *et al.*, 2003], and this allows a larger parameter space to be investigated without developing instabilities due to negative components in the velocity distribution function. For example, larger density ratios can be reached in single-component two-phase models. (We have found that very large density ratios can be reached if the equilibrium populations are assumed to be given by $f_i^{eq} \propto w_i \rho \exp[(\mathbf{v}_i - \mathbf{u}')^2 / 2k_B T]$, and \mathbf{u}' is selected to conserve momentum.)

[70] In practice, a variety of methods can be used to include the effects of a body force in the lattice Boltzmann equations [Buick and Greated, 2000] including altering the equilibrium distribution function used in equation (92) to reflect the change in momentum generated by the body force, \mathbf{F} ,

$$\mathbf{u}' = \mathbf{u} + \tau \mathbf{F} / \rho, \quad (93)$$

and adding a term on the right-hand side of equation (90) that corresponds to the external force term in the Boltzmann equation.

[71] For the lattice Boltzmann model to simulate the behavior of an isotropic fluid, the set of basis vectors, $\{\mathbf{e}_i\}$, and the corresponding weights, $\{w_i\}$, must satisfy the following normalization and symmetry conditions:

$$\sum_{i=1}^n w_i = 1, \quad (94)$$

$$\sum_{i=1}^n w_i \mathbf{e}_{i\alpha} = 0, \quad (95)$$

$$\sum_{i=1}^n w_i \mathbf{e}_{i\alpha} \mathbf{e}_{i\beta} \mathbf{e}_{i\gamma} = 0, \quad (96)$$

$$\sum_{i=1}^n w_i \mathbf{e}_{i\alpha} \mathbf{e}_{i\beta} = \Pi^{(2)} \delta_{\alpha\beta}, \quad (97)$$

$$\sum_{i=1}^n w_i \mathbf{e}_{i\alpha} \mathbf{e}_{i\beta} \mathbf{e}_{i\gamma} \mathbf{e}_{i\delta} = \Pi^{(4)} \delta_{\alpha\beta} \delta_{\gamma\delta} + \delta_{\alpha\gamma} \delta_{\beta\delta} + \delta_{\alpha\delta} \delta_{\beta\gamma}, \quad (98)$$

TABLE 1. Basis Vectors and Weights for Most Commonly Used Two-Dimensional and Three-Dimensional Lattice Boltzmann Models

Model	$e_i^2 = 0$	$e_i^2 = 1$	$e_i^2 = 2$	$e_i^2 = 3$
D ₂ Q ₉	$w_i = 4/9$	$w_i = 1/9$	$w_i = 1/36$	
D ₃ Q ₁₅	$w_i = 2/9$	$w_i = 1/9$		$w_i = 1/72$
D ₃ Q ₁₉	$w_i = 1/3$	$w_i = 1/18$	$w_i = 1/36$	

where α , β , γ , and δ are the Cartesian space directions. The quantity $\Pi^{(2)}$ relates the pressure, P , to the fluid density, ρ , and the sound velocity in the fluid is given by

$$c_s = (P/\rho)^{1/2} = \sqrt{\Pi^{(2)}}. \quad (99)$$

It follows from equation (97) that $\Pi^{(2)}$ is twice the kinetic energy per degree of freedom, and from the equipartion of energy principle

$$k_B T = m \langle v_\alpha^2 \rangle = \Pi^{(2)} = c_s^2. \quad (100)$$

The most commonly used lattice Boltzmann models are the two-dimensional D₂Q₉ model and the three-dimensional D₃Q₁₅ and D₃Q₁₉ models. Here the first subscript indicates the dimensionality of the system, and the second subscript indicates the number of basis vectors. Table 1 shows the basis vector set for these three models, where $e_i^2 = \mathbf{e}_i \cdot \mathbf{e}_i$ is the square of the length of the i th basis vector. The vector basis set is defined by the vector lengths and the symmetry of the lattice. For example, for the D₂Q₉ model, there is one vector of length zero (the null vector), there are four vectors of length 1 ((1, 0), (-1, 0), (0, 1), and (0, -1)), and there are four vectors of length $\sqrt{2}$ ((1, 1), (1, -1), (-1, -1), and (-1, 1)).

[72] In lattice Boltzmann models, the local fluid densities and velocities are determined by the population densities $\{f_i(\mathbf{x}, t)\}$ (the fluid density is given by $\rho(\mathbf{x}, t) = \sum_i f_i(\mathbf{x}, t)$, and the fluid velocity is given by $\mathbf{u}(\mathbf{x}, t) = (1/\rho) \sum_i c_i f_i(\mathbf{x}, t)$). In a gas, the viscosity is generated by the transfer of momentum between fluid elements that are moving at different velocities by moving atoms or molecules (momentum diffusion). According to the kinetic theory of gasses, the viscosity is given by $\eta \approx \rho \lambda \bar{v}/d$, where \bar{v} is the average molecular speed, d is the dimensionality of the system, and λ is the mean free path. In lattice Boltzmann simulations, the mean free path is determined by the relaxation time, τ (the shorter the relaxation time, the shorter the mean free path), and the viscosity is given by [Luo and Girimaji, 2003]

$$\eta = \rho c_s^2 \Delta t (2\tau - 1)/2, \quad (101)$$

and if the time, Δt , required for streaming from one node to its neighboring nodes is used as the unit of time, then $\eta = \rho(2\tau - 1)/6$ for the models in Table 1. If the single relaxation time approximation is used, the Schmidt number, $Sc = \eta/D\rho$, where D is the molecular diffusivity, is equal to

unity, a value typical of gasses, whereas a Schmidt number on the order of 10^3 is more typical of liquids. (The large Schmidt number in liquids is a consequence of the “cage effect.” The molecules can undergo many momentum-transferring “collisions” with neighboring molecules before they escape the transient cage formed by their neighbors.) As a result, diffusive transport is often unrealistically high relative to advection in lattice Boltzmann simulations.

[73] The application of lattice Boltzmann models to subsurface applications requires appropriate boundary conditions. In particular, flow in fractures and porous media (flow in confined systems) requires no-slip, no-flow boundary conditions at solid-fluid interfaces. These boundary conditions can most easily be implemented by means of a “bounce back” procedure that reverses particle velocities when they contact a solid-liquid interface. If the nodes are located on this interface, this involves a simple particle velocity reversal ($f_i(\mathbf{x}, \mathbf{e}_i) \rightarrow f_i(\mathbf{x}, -\mathbf{e}_i)$), and if the interface is midway between the nodes, $f_i^c(\mathbf{x}, t+1) = f_i^c(\mathbf{x}, t)$, where the subscript i indicates the population density with a velocity of $-\mathbf{e}_i$ and f_i^c indicates the population density after collision [Bouzidi et al., 2001]. A variety of other boundary conditions have been proposed to improve accuracy and treat curved boundaries [Bouzidi et al., 2001]. However, lattice Boltzmann models with subgrid-scale interface location are rarely used in practice. In lattice Boltzmann simulations the fluid(s) can be driven through a model porous, fractured, or fractured porous medium by using a body force, by imposing pressure boundary conditions via the density and the lattice Boltzmann equation of state, or, less commonly, by imposing velocity boundary conditions.

[74] The model fluids generated by simple lattice Boltzmann models are ideal gasses, and hence they have high compressibilities. If the pressure variations are small, lattice Boltzmann models do generate flows that can be accurately described by the incompressible Navier-Stokes equation, and under these conditions the flow of real gasses can also be accurately described by the incompressible Navier-Stokes equations (equations (4) and (5)), but flows with Mach numbers ($Ma = v/c$, where v is the fluid velocity and c is the sound velocity) greater than 0.1 and flows with pressure variations ($\delta P/P$ or $\nabla P L/P$, where L is a length characteristic of the system size) or density variations ($\delta \rho/\rho$ or $\nabla \rho L/\rho$) greater than 0.01 will exhibit significant deviations from incompressible Navier-Stokes flows. (The sound velocity is determined by the compressibility and density of the fluid. For flow of a fluid with a characteristic velocity, \mathbf{V} , in a region of size, L , the fluid will change velocity at a rate of $O(\mathbf{V}^2/L)$. This acceleration will require a pressure gradient of $O(\rho \mathbf{V}^2/L)$, and the pressure variations within the fluid will be $O(\rho \mathbf{V}^2)$. The corresponding density change, $\delta \rho/\rho$, will be $O(\rho \mathbf{V}^2/k_e)$, where k_e is the modulus of the fluid. Since the sound velocity is given by $c = (k_e/\rho)^{1/2}$, it follows that $\delta \rho/\rho = O(\mathbf{V}^2/c^2)$ or $\delta \rho/\rho = O(Ma^2)$.) Although the Mach numbers and density fluctuations are usually very small in subsurface flows, the Mach number and density fluctuations in lattice Boltzmann models used to simulate these processes may be much higher. The compressibility of

the lattice Boltzmann fluid can be modified by changing the population of rest particles (particles with zero velocity) in the equilibrium distribution function [Alexander *et al.*, 1992] or by including a body force that acts in the direction of the pressure gradient [Buick and Cosgrove, 2006]. However, the range of sound velocities that can be simulated using these approaches is quite limited, and it is not possible to increase the sound velocity sufficiently to simulate highly incompressible fluids. In particular, the dimensionless ratio $L\eta VK/k$, where V is a characteristic flow velocity, K is the compressibility, and k is the permeability, characterizing the density variation needed to drive a fluid through a fracture or porous medium must be much smaller than unity for compressibility effects to be negligible.

[75] Recently, Shi *et al.* [2006] have developed a lattice Boltzmann model based on the Enskog equation for the hard disc or hard sphere fluid distribution function, f [Hirschfelder *et al.*, 1964]. Simulations based on this model demonstrate that the compressibility effects are much smaller for the Enskog equation-based model than the Boltzmann equation-based model (ideal gas model) at relatively high pressure gradients.

[76] A lattice Boltzmann approach can also be used to simulate diffusion. This provides a way of simulating coupled flow and diffusion (dispersion) that is consistent with lattice Boltzmann flow simulations [Flekkoy *et al.*, 1995] and a basis for reactive transport simulations [Kang *et al.*, 2004]. In this case, a distribution function, f' , is used to describe the scalar intensive variable field, such as the concentration of a diffusing substance. The corresponding single relaxation time, BGK, lattice Boltzmann equation is

$$f'_i(\mathbf{x} + \mathbf{e}_i, t + \delta t) = f'_i(\mathbf{x}, t) + \{f_i^{eq}[(c(\mathbf{x}), \mathbf{v}(\mathbf{x}), t)] - f'_i(\mathbf{x}, t)\} / \tau_D, \quad (102)$$

where $c(\mathbf{x})$ is the magnitude of the scalar field at position \mathbf{x} and τ_D is the diffusional relaxation time corresponding to the diffusion coefficient, \mathcal{D} . The magnitude of the scalar field is given by $c(\mathbf{x}, t) = \sum_i g_i(\mathbf{x}, t)$, and the diffusion coefficient is related to the relaxation time, τ_D , by a model relationship similar to that relating the fluid viscosity to the relaxation time in equation (101).

[77] Lattice Boltzmann methods have been used extensively to simulate both single-component and multicomponent multiphase fluids. Multiphase fluids are simulated by adding “internal” forces that represent the effects of molecular fluid-fluid interactions. In the popular approach developed for a single-component system by Shan and Chen [1993, 1994] the force acting at position \mathbf{x} is given by

$$\mathbf{F}(\mathbf{x}, t) = -\psi(\mathbf{x}, t) \sum_i G(|\mathbf{e}_i|) \psi(\mathbf{x} + \mathbf{e}_i) \mathbf{e}_i, \quad (103)$$

where the summation is over the vector basis set, $\psi(\mathbf{x}) = \psi[\rho(\mathbf{x})]$ is a function of the density, and $G(e)$ is the node-node interaction strength, which depends on the separation, $e = |\mathbf{e}_i|$. The forces calculated in this manner are then included in the lattice Boltzmann equation using equation (93) to calculate the equilibrium fluid velocity.

This approach may also be used to simulate multicomponent systems. In multicomponent systems a separate distribution function, $f_i^{(n)}(\mathbf{x}, t)$, where n varies from 1 to C is used for each of the C components, and the evolution of each component is obtained from its own lattice Boltzmann equation, which is coupled to the distribution functions for the other components. In this case, equation (103) is generalized to

$$\mathbf{F}^{(j)}(\mathbf{x}, t) = -\psi^{(j)}(\mathbf{x}, t) \sum_{k=1}^{k=C} \sum_i G_{jk}(|\mathbf{e}_i|) \psi^{(k)}(\mathbf{x} + \mathbf{e}_i) \mathbf{e}_i, \quad (104)$$

where G_{jk} is the strength of the interaction between component j and component k . An advantage of this method is that fluid-wall interactions can be included in a consistent manner to control the wetting behavior [Martys and Chen, 1996].

[78] An alternative approach [Swift *et al.*, 1996] is to base the lattice Boltzmann simulation on a Ginzburg-Landau/Cahn-Hilliard free energy functional (equations (9)–(12) with a density order parameter) with a two-phase homogeneous free energy and calculate an expansion for the equilibrium distribution function $\{f_{eq}^i\}$, like equation (92) but including the effects of the nonideal free energy functional. Other models have also been proposed and implemented [e.g., Gunstensen *et al.*, 1991].

[79] One of the most important limitations of lattice Boltzmann models for multiphase fluid flow has been that unlike lattice gas models, they have poor numerical stability, which has prevented them from being used to simulate multiphase fluid flow with large density and viscosity ratios. Since large density and viscosity ratios are important in geologically important systems (water and air in the vadose zone or gas and molten rock in basaltic lavas, for example), this has been a serious deficiency. Quite recently, lattice Boltzmann methods that are stable for density ratios up to at least 1000:1 have been introduced [Lee and Lin, 2005; Zheng *et al.*, 2006]. However, these models are too new to properly evaluate their advantages and disadvantages.

[80] In single-component two-phase systems (liquid/vapor) or two-component two-phase systems (partially miscible liquids or liquid/gas) systems, the density ratio (ρ_1/ρ_2) or the concentration ratios (c_1^1/c_2^1 or c_1^2/c_2^2), where the subscripts indicate the phase and the superscripts indicate the component, are often very large (or very small). However, because of the instability problems associated with lattice Boltzmann models, simulations are carried out with density or concentration ratios that are not very large or very small. As a result, the diffusive transport of the minority species will, in many cases, be unrealistically large, and this can have a substantial impact on simulation results. In particular, this exacerbates the effect of the small Schmidt number when lattice Boltzmann models are applied to multicomponent liquids.

[81] Lattice Boltzmann models have also been used to simulate mineral dissolution and precipitation [Kang *et al.*, 2004]. Early lattice Boltzmann simulations of dissolution

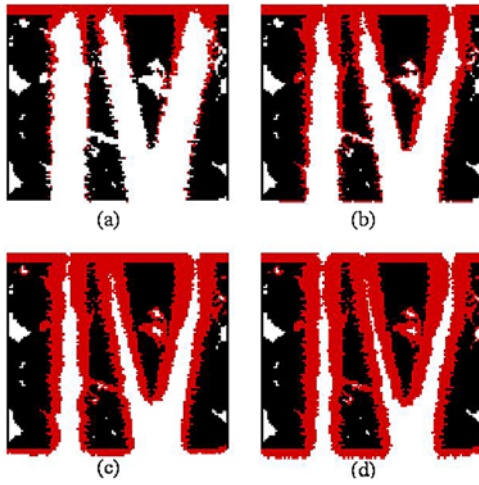


Figure 6. Lattice Boltzmann simulation of progressive precipitation and sealing in a microfracture network. In the simulation, the pore space is initially filled with fluid at equilibrium with the solid (black), and the fluid is driven from top to bottom by a pressure difference. The inflowing fluid is then changed to a supersaturated composition, and precipitate (red) is deposited on the original solid or on accumulated precipitate. During the simulation, the Damkohler number decreases (from (a) 32.4 ($t^* = 0.0457$, where t^* is the time normalized by L^2/D) through (b) 3.24 ($t^* = 0.243$) and (c) 0.324 ($t^* = 1.972$) to (d) 0.0324 ($t^* = 17.118$)). The initial Peclet number, $Pe = \langle |v| \rangle L/D$, was 62.8. In the simulation, the precipitate represents CO_2 hydrate. However, the model does not contain details that are specific to the carbon sequestration application, and the results are determined by the Damkohler number, the Peclet number, and the initial pore space geometry. Reprinted from Kang *et al.* [2005], copyright 2005, with permission from Elsevier.

and precipitation used simple reaction kinetics models such as

$$j = \mathcal{D} \mathbf{n}_s \cdot \nabla c_s = k_r (c_s - c_{eq}), \quad (105)$$

where j is the solute flux density at the interface, \mathcal{D} is the solute diffusion coefficient, \mathbf{n}_s is the inward pointing unit vector perpendicular to the solid surface at position s on the interface, ∇c_s is the concentration gradient at s , c_s is the concentration at s , c_{eq} is the concentration in equilibrium with the solid at s , and k_r is a reaction (dissolution/precipitation) rate constant. However, the lattice Boltzmann approach is much more versatile than this, and models with more general and more complex interfacial (heterogeneous) chemistry have been developed; these models have been combined with lattice Boltzmann models for solution (homogeneous) chemistry and used to simulate pore-scale reactive transport [Kang *et al.*, 2006, 2007]. In general, the chemical potential is higher for a surface that is convex when viewed from the adjacent fluid, and equation (105) may be replaced by

$$\mathcal{D} \mathbf{n}_s \cdot \nabla c_s = k_r [c_s - c_{eq}(\kappa)], \quad (106)$$

where κ is the curvature of the fluid-solid interface. More generally, for both linear and nonlinear reaction kinetics, the effects of surface curvature on the rates of dissolution and precipitation can be accounted for by using the relationship $\mu_s = \mu_s^0 + \Gamma \kappa V_m$, where μ_s^0 is the chemical potential of a flat surface, to calculate the chemical potential of the solid at the surface and then using classical chemical kinetics or linear nonequilibrium thermodynamics [Onsager, 1931a, 1931b; Prigogine, 1947] to calculate the effect of the chemical potential on the reaction rate.

[82] In most lattice Boltzmann models, the solid and fluid phases are represented by a set of lattice sites, and the interface is represented by the edges of lattice sites that separate different phases. If this “staircase” representation is used, it is difficult to calculate interface curvatures, and the Gibbs-Thompson effect (curvature-dependent chemical potentials) is usually neglected. In these cellular models, the amount of solid dissolved from each “solid” site and/or the amount of solid precipitated in each fluid site adjacent to the solid-liquid interface is calculated from equation (104) and accumulated. When the amount of dissolution or the amount of precipitation reaches unity (the site volume), the solid site is converted to a liquid site or a liquid site is converted to a solid site, and the new solid and liquid sites adjacent to the interface are identified. Variants on this cellular approach may be implemented. An improved lattice Boltzmann model, which approximately takes into account the effects of partially filled lattice cells on fluid flow and solute diffusion, has been developed [Verhaeghe *et al.*, 2005].

[83] Mineral precipitation may be diffusion controlled, reaction controlled, nucleation controlled, or in a crossover between these limiting cases. The crossover from diffusion-limited growth to reaction-limited growth depends on the dimensionless Damkohler number, $Da = k_r L/D$ (the rate constant k_r in equation (106) relates the rate of surface growth to the supersaturation, or undersaturation, and it has units of lt^{-1}). Simulations with the type of lattice Boltzmann model described above exhibit a crossover from a fractal dendritic pattern, similar to that generated by the diffusion-limited aggregation [Witten and Sander, 1981] model in the $Da \rightarrow \infty$ limit to a compact pattern, similar to that generated by the Eden model [Eden, 1961] in the $Da \rightarrow 0$ limit. This type of simulation is illustrated by Figure 6, which shows a lattice Boltzmann simulation of precipitation in a microfracture network [Kang *et al.*, 2005; Steefel *et al.*, 2005].

[84] Lattice Boltzmann models for multiphase fluid flow in the presence of solid surfaces give qualitatively realistic contact angle behavior (contact angles that depend on the capillary number [Fan *et al.*, 2001]), and in at least one model [Briant *et al.*, 2001] the equilibrium static contact angle can be calculated from model parameters.

[85] The capillary number-dependent contact angle behavior leads to a quite rich phenomenology, even in quite simple systems. For example, Kang *et al.* [2005] have used a three-dimensional two-component two-phase lattice Boltzmann model, based on the Shan and Chen [1993,

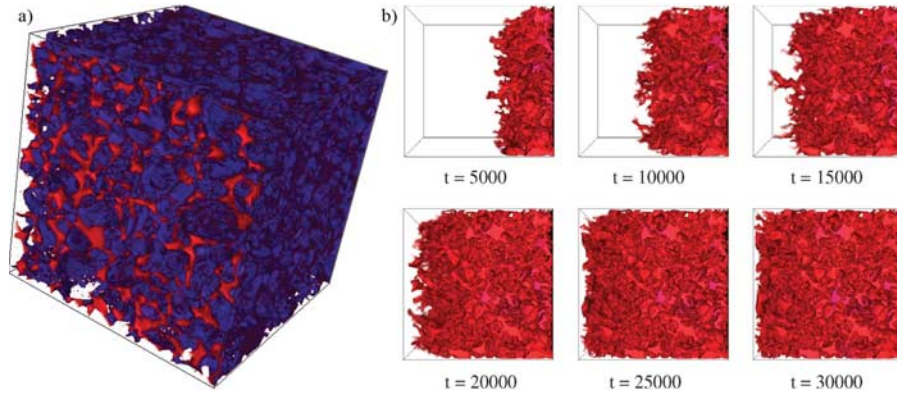


Figure 7. Lattice Boltzmann simulation of fluid-fluid displacement in a porous medium. (a) A visualization of a $4.9 \mu\text{m}$ resolution X-ray tomography image of a Bentheimer sandstone with the mineral phase in blue and the pore space in red. (b) Six stages in a lattice Boltzmann simulation of gravity-driven fluid-fluid displacement in the pore space determined by X-ray tomography. Only the displacing fluid is shown in red. Reproduced from *Harting et al.* [2005, Figures 2 and 3] with permission of the Royal Society.

1994] lattice Boltzmann model for multicomponent fluids, to simulate the behavior of a droplet of fluid that contacts one wall of a vertical rectangular channel, which is filled with a second fluid of the same density and viscosity. The two fluids are driven through the channel by gravity, and at small capillary numbers, the drop of fluid slides along the wall and reaches a steady shape. Depending on the wetting behavior of the drop, characterized by the contact angle, and the capillary number, the entire drop may be detached from the surface, or the drop may fragment in various ways leaving two drops detached from the surface or one drop attached to the surface and one or more detached drops when the critical capillary number is exceeded.

[86] Images of complex three-dimensional pore volumes consisting of up to 10^{10} volume elements (voxels) can be obtained using desktop and synchrotron X-ray tomography. These images have been used to develop pore networks for pore network model simulations, but they are also being used to simulate single-phase and multiphase fluid flow using lattice Boltzmann models. As the technology required to obtain even more detailed and/or larger-scale images is developed, faster computers become available, and lattice Boltzmann models that provide more accurate results under a wider range of conditions and for a wider range of fluids are developed and evaluated, we expect that pore network models will be displaced for some applications by high-resolution lattice Boltzmann simulations. Figure 7 shows a simulation of fluid-fluid displacement carried out in this fashion.

6. MONTE CARLO MODELS

[87] A number of Monte Carlo models have been used for more than 40 years [Bird, 1963] to simulate fluids. In these models [Malevanets and Kapral, 1999], the fluid is represented by particles that undergo streaming and

collision. In the streaming step, the particles move with a constant velocity so that

$$\mathbf{r}_i(t + \Delta t) \rightarrow \mathbf{r}_i(t) + \mathbf{v}_i \Delta t, \quad (107)$$

where $\mathbf{r}_i(t)$ is the position of particle i at time t , $\mathbf{v}_i(t)$ is its velocity, and Δt is the time step. In the collision step the particle velocities after collision are given by

$$\mathbf{v}_i(t^+) \rightarrow \langle \mathbf{v}(t) \rangle + \mathcal{R}[\mathbf{v}_i(t) - \langle \mathbf{v}(t) \rangle], \quad (108)$$

where $\langle \mathbf{v}(t) \rangle$ is the average velocity of the “colliding” particles (the particles in the same cell of a lattice that covers the computational domain) and \mathcal{R} is a random rotation operator. Here t is the time just before the collision takes place and t^+ is the time just after the collision. The rotation operator can be selected randomly from a uniform distribution of all possible rotations or from a discrete set of rotations. An alternative is to select the new particle velocities on the basis of a Maxwell-Boltzmann distribution

$$\mathbf{v}_i(t^+) \rightarrow \langle \mathbf{v}(t) \rangle + \mathbf{v}_i^{\text{MB}}, \quad (109)$$

where \mathbf{v}_i^{MB} is a velocity selected from a Maxwell-Boltzmann distribution adjusted to ensure an average velocity (relative to the local velocity of the fluid) of zero for the particles within the cell ($\sum_i \mathbf{v}_i^{\text{MB}} = 0$, where the summation is over all of the particles in a cell) [Allahyarov and Gompper, 2002].

[88] The cells should be large enough to ensure that the average velocity of the particles inside the cell does not fluctuate too much (typically 20 or more particles), and the cell size should not be larger than the mean free path of the fluid that the model is intended to simulate [Alexander et al., 1998]. Equations (107) and (108) conserve mass, momentum, and energy. Nonslip boundary conditions can be imposed by reversing the velocity of any particle that

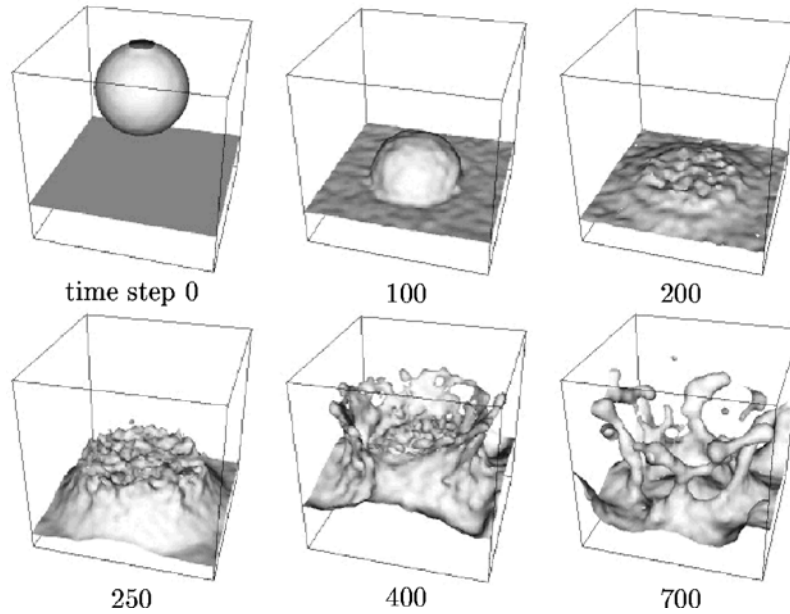


Figure 8. Real-coded lattice gas simulation of a liquid drop impacting a free liquid surface. The “liquid particles” in the drop and in the free liquid have masses that are 100 times the masses of the “gas particles” that fill the rest of the system. Reprinted from Hashimoto *et al.* [2000], copyright 2000, with permission from Elsevier.

contacts a solid surface (bounce back boundary conditions) [Allahyarov and Gompper, 2002]. However, if the solid-fluid interface cuts through grid cells, more complex algorithms are required to ensure no-slip boundary conditions [Lamura *et al.*, 2001]. A simulation can be started by inserting particles at randomly selected positions in the computational domain, randomly selecting their directions of motion, and randomly selecting their velocities from an initial velocity distribution with a maximum velocity constraint ($|\mathbf{v}| < v_{\max}$). The velocity distribution soon relaxes to a Maxwell-Boltzmann distribution. To ensure Galilean invariance, the grid can be randomly shifted by a distance on the order of the cell size before each collision (random rotation) step [Ihle and Kroll, 2001]. This Monte Carlo modeling approach has been given a variety of names including stochastic rotation dynamics, multiparticle collision dynamics, and the real-coded lattice gas.

[89] The effect of gravity acting on the fluid can be included by acceleration of the particles between collisions

$$\mathbf{v}_i(t + \Delta t) = \mathbf{v}_i(t) + \mathbf{g}\Delta t, \quad (110)$$

where \mathbf{g} is the gravitational acceleration. These Monte Carlo methods can also be used to simulate multiphase fluid flow [Hashimoto *et al.*, 2000; Sakai *et al.*, 2002b; Inoue *et al.*, 2004]. One approach [Sakai *et al.*, 2002a], based on the Rothman and Keller [1988] lattice gas/lattice Boltzmann model for multiphase fluid behavior, is to bias the rotation of the particles in response to the composition gradient. For example, in the case of a binary fluid, the particles are given labels of $q_n = \pm 1$, depending on whether they represent

component 1 or component 2. A composition gradient, \mathbf{g}_C , defined as

$$\mathbf{g}_C(\langle \mathbf{r} \rangle) = \sum_i (\langle \mathbf{r} \rangle_i - \langle \mathbf{r} \rangle) / (|\langle \mathbf{r} \rangle_i - \langle \mathbf{r} \rangle|^2) \sum_{n=1}^{n=N(\mathbf{r}_i)} q_n \quad (111)$$

is calculated for each cell (in which the average particle position is $\langle \mathbf{r} \rangle$), where $\langle \mathbf{r} \rangle_i$ is the position of the center of the i th neighboring cell and $N(\mathbf{r}_i)$ is the number of particle in the i th neighboring cell. The neighboring cells may include only nearest neighbor (nn) cells, nn + next-nearest neighbor (nnn) cells, nn + nnn + next to next-nearest neighbor (nnnn) cells, etc. A composition flux vector is also defined as

$$\mathbf{q}(\langle \mathbf{r} \rangle) = \sum_{n=1}^{n=N(\mathbf{r})} q_n [\mathbf{v}_n - \langle \mathbf{v} \rangle(\mathbf{r})], \quad (112)$$

where \mathbf{v}_n is the velocity of the n th particle in the cell for which the composition flux vector is calculated. To bring about phase separation, the rotation operator, \mathcal{R} , that maximizes $\mathbf{g}_C(\langle \mathbf{r} \rangle) \cdot \mathcal{R}[\mathbf{q}(\langle \mathbf{r} \rangle)]$ is selected in each cell.

[90] Figure 8 shows the results of a Monte Carlo simulation of the gravity-driven acceleration of a liquid drop through a gas and its impact on a “pool” of liquid. The simulation was performed using a real-coded lattice gas algorithm very similar to that described above.

[91] Very little experience had been gained with the application of Monte Carlo methods to multiphase fluid flow in the subsurface, and this method has been much less investigated and developed than lattice Boltzmann methods or dissipative particle dynamics for general applications.

However, *Sakai* [2002] has used the real-coded lattice gas approach to simulate single-phase and multiphase fluid flow in two-dimensional porous media. In these simulations bounce back boundary conditions were used at fluid-solid interfaces, and wetting conditions were controlled via rotation operators that depend on a composition gradient, g_C (equation (117)), calculated using a value of q_s assigned to surface cells. Other approaches could equally well be used, including the introduction of interaction forces similar to those used by *Shan and Chen* [1994] to bring about phase separation in lattice Boltzmann simulations, and this approach could also be used to control wetting behavior.

[92] In the related direct simulation Monte Carlo model [Bird, 1994; Alexander *et al.*, 1998] pairs of particles within the same cell are selected randomly after the streaming step, with probabilities that are proportional to their relative velocities. The selected particle pairs are then subjected to collisions that conserve momentum and energy. This Monte Carlo method simulates a fluid that has an ideal gas equation of state but the transport behavior of a dilute hard sphere gas. A hard sphere equation of state can be obtained by increasing the distance that the particles travel after collision to represent the effect of collision between particles of nonzero size [Alexander *et al.*, 1995]. The additional postcollision displacement is given by $\pm \hat{\mathbf{d}}\sigma$, where σ is the hard sphere diameter and the unit vector, $\hat{\mathbf{d}}$, is given by $\hat{\mathbf{d}} = (\mathbf{v}_r' - \mathbf{v}_r)/|\mathbf{v}_r' - \mathbf{v}_r|$. Here $\mathbf{v}_r = \mathbf{v}_i - \mathbf{v}_j$ is the relative velocity before collision, and \mathbf{v}_r' is the relative velocity after collision (the additional displacement is $\hat{\mathbf{d}}\sigma$ for particle i and $-\hat{\mathbf{d}}\sigma$ for particle j). A similar approach can be used to represent the effects of attractive interactions between the particles [Wang and Li, 2003]. The length but not the direction of the additional postcollision displacement is changed by an amount that depends on the temperature to simulate a nonideal gas with a van der Waals equation of state. These algorithms have been used to simulate nonideal gasses, but it is not clear if they can be used to simulate multiphase fluids.

7. MOLECULAR DYNAMICS

[93] In molecular dynamics (MD) simulations the dynamics of a large number of particles that represent atoms or molecules is simulated by integrating the classical equation of motion

$$d\mathbf{v}_i/dt = \mathbf{f}_i/m_i, \quad (113)$$

where \mathbf{v}_i is the velocity of the i th particle, \mathbf{f}_i is the force acting on the i th particle due to interaction with the other particles in the system and external forces such as gravity acting on particle masses and electric fields acting on charged particles, and m_i is the mass of the i th particle. (In some molecular dynamics simulations, the rotation of rigid structures is included and the rotational dynamics is included via the equation $\dot{\omega}_i = \mathbf{I}_i^{-1}\mathbf{\Gamma}_i$, which is analogous to equation (74), where $\dot{\omega}_i$ is the angular velocity of the i th

rigid body, \mathbf{I}_i is its inertial tensor, and $\mathbf{\Gamma}_i$ is the torque exerted on the i th rigid structure by its neighbors.) In principle, MD simulations can be used to simulate fluid flow, and there is evidence that continuum hydrodynamics can be applied on scales on the order of a few nm in some systems [Hirshfeld and Rapaport, 1998; Koplik *et al.*, 1988; Raviv *et al.*, 2001]. In addition, the hydrodynamic size of nanoparticles, determined by dynamic light scattering, is often assumed to be essentially equal to the physical size, and in many cases good agreement has been obtained with other methods such as transmission electron microscopy and plasma resonance blue shift measurements [Xu *et al.*, 2007]. However, experiments and molecular dynamics simulations indicate that the structure of a variety of liquids is much more ordered adjacent to atomically smooth solid surfaces than in bulk fluids [e.g., Christenson, 1983; Yu *et al.*, 1999].

[94] The behavior found in some molecular dynamics simulations of nanoscale multiphase fluid dynamics, such as the breakup of fluid filaments [Moseler and Landman, 2000], differs substantially from the behavior found on larger scales. In this case the differences between nanoscale and large-scale behavior have been attributed to the effects of fluctuations on small scales, which become important when the thermal length, $L_T = (k_B T/\Gamma)^{1/2}$ ($L_T \approx 0.5$ nm for water at room temperature), becomes comparable to the diameter of the fluid filament, and a stochastic hydrodynamics (stochastic lubrication theory) equation has been shown to be consistent with molecular dynamics simulations [Kang and Landman, 2007].

[95] In typical MD simulations with realistic particle-particle interactions, the time step must be on the order of a femtosecond to obtain accurate results, and the duration of the simulation (in physical time units) is typically on the order of a nanosecond (or up to a microsecond if a small number of particles is simulated). This is the most important limitation of the application of molecular dynamics to multiphase fluid flow on the pore scale. Because the strain must be large to reproduce the complex phenomena characteristic of multiphase fluid in confined systems, the strain rate is very large in typical nonequilibrium MD simulations (often on the order of 10^{10} s^{-1} , typical of the strain rates in a nuclear explosion), and at these very high strain rates, the fluid structure and concomitant viscosity may change significantly.

[96] Despite these limitations, MD could be used to simulate multiphase fluid flow on the pore scale if the molecular system provided an accurate scale model for macroscopic (pore-scale) systems of interest. This would be possible if the size of the system used in the MD simulation was large enough to reach the hydrodynamic limit, if the system size was large enough to ensure that the effects of the solid boundaries on the adjacent fluid could be neglected, and if the critical dimensionless ratios were essentially the same in the molecular dynamics model and the system of interest. In the case of fluid flow in the

subsurface, the important dimensionless ratios are (1) the Reynolds number,

$$Re = VL\rho/\eta, \quad (114)$$

where L is the characteristic system size (pore diameter, fracture aperture width, etc.), ρ is the fluid density, and η is the viscosity; (2) the Bond number,

$$Bo = \delta\rho gL^2/\Gamma, \quad (115)$$

where $\delta\rho$ is the difference in density between the two fluids, Γ is the interfacial energy per unit area, and g is the gravitational velocity; and (3) the capillary number,

$$Ca = \eta V/\Gamma. \quad (116)$$

In addition, the Mach number,

$$Ma = v/c, \quad (117)$$

where c is the sound velocity in the fluid, may be important in computer simulations. It is possible to carry out molecular dynamics simulations with Reynolds numbers, Bond numbers, and capillary numbers that are characteristic of subsurface flows. However, simulations with a very large number of particles would be needed to reduce the effects of wall slip (section 3), the formation of ordered fluid adjacent to walls, and the effects of thermal fluctuations. Because of the high strain rates, the Mach number would be quite large in molecular dynamics simulations of multiphase fluid flow, and compressibility effects would be large ($Ma \leq 0.1$ is required to avoid large compressibility effects).

[97] At sea level, the mean free path, λ_f , in air is of the order of 10^{-7} m, smaller than typical pore sizes but larger than the scale of a typical molecular dynamics simulation. If molecular dynamics is used to simulate liquid-gas systems, either the Knudsen number, Kn , defined by

$$Kn = \lambda_f/L, \quad (118)$$

must match the Knudsen number in the corresponding physical system or Kn must be much less than unity (or much greater than unity) in both the model and the physical system. At high pressures in the subsurface, the mean free path in the vapor phase may be smaller than the scale of a typical molecular dynamics simulation.

[98] In practice, MD simulations with realistic particle-particle (atom-atom or molecule-molecule) interactions are not used to simulate multiphase fluid flow in confined systems such as pore volumes or fracture apertures. However, the applications of a number of particle models closely related to molecular dynamics, such as smoothed particle hydrodynamics and dissipative particle dynamics, are growing, and some of these particle methods are discussed in sections 8 and 9.

[99] MD simulations are important in gaining a better understanding of the behavior of very thin fluid films on solid surfaces, fluids very near to solid surfaces, fluid-fluid-solid contact line dynamics, and the velocity-dependent contact angle behavior associated with moving contact lines

(section 3). A number of hybrid MD/continuum models have been developed with the idea of using molecular dynamics to simulate the behavior of fluids near solid surfaces, where continuum models are inadequate, and using standard continuum incompressible Navier-Stokes equation solvers or compressible fluid flow equation solvers farther from the solid surface. The fluid viscosity and equation of state (for compressible flows) must be determined from the MD model, or, at least in principle, accurate intermolecular interactions and experimentally determined bulk fluid properties could be used. An overlap region is needed to match the MD and continuum models, and a number of methods for achieving the matching have been proposed [e.g., O'Connell and Thompson, 1995; Hadjiconstantinou, 1999; Flekkoy et al., 2000; Nie et al., 2004]. In general, the particle (MD) model is coarse grained near the inner boundary of the overlap region (the boundary nearest to the solid) to provide continuum variables (fluid velocity, momentum flux tensor, and energy flux, depending on the model details) that are used as boundary conditions for the continuum model, and the continuum variables are used to constrain the particle variables in a second part of the overlap region, farther from the solid surface. In addition, the particles must be prevented from spreading and eventually filling the entire computational domain. The matching between the particle and continuum models must conserve mass, momentum, and energy.

[100] For example, in the hybrid method investigated by Nie et al. [2004], the overlap region consists of three layers of cells used in the continuum fluid dynamics model. The particle velocities are averaged over small volumes centered on the points where the velocities are needed to provide a boundary condition for the continuum model at the inner boundary of the overlap region (the boundary nearest to the solid). In the second layer of cells in the overlap region, the average particle velocity is constrained to be equal to the average continuum fluid velocity obtained from the continuum fluid dynamics model. This is accomplished by replacing the standard molecular dynamics equation of motion with

$$dv_i/dt = f_i/m - \frac{1}{ncm} \sum_{i=1}^{i=n_c} f_i + Dv_c(t)/Dt, \quad (119)$$

where n_c is the number of particles in the volume element, v_c is the average continuum velocity in the volume element, and D is the Lagrangian derivative or material derivative ($Dx/Dt = dx/dt + \mathbf{v} \cdot \nabla x$). The MD particles are prevented from leaving the region between the solid-fluid interface and the outer boundary of the overlap zone by a force that directs them toward the solid as they approach the outer boundary of the overlap region, and this force diverges as the outer boundary is approached.

[101] The final component of the coupling between the particle and continuum models is to add or remove particles near the outer boundary of the overlap region to match the mass flux across the boundary. If the local mass flux is in the outward direction (toward the continuum region) particles closest to the outer boundary are removed and if there

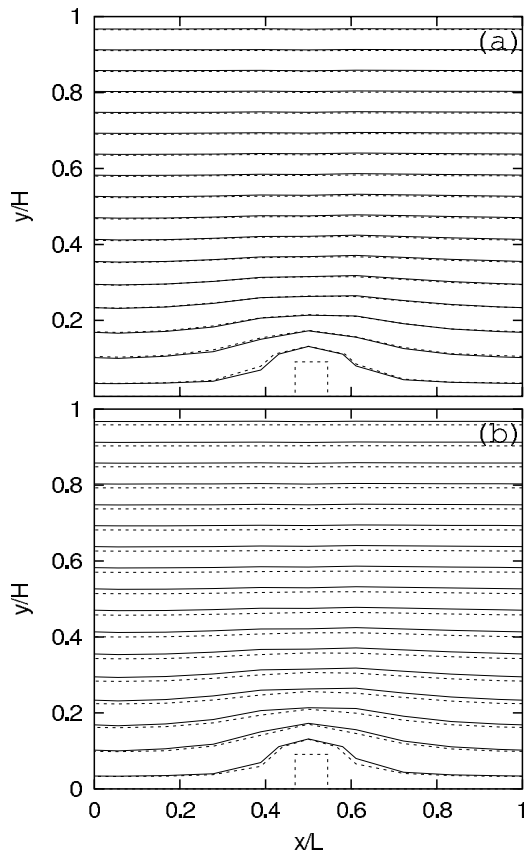


Figure 9. The streamlines for channel flow with a raised area on the bottom wall. The square in the middle of the bottom wall shows the location of the bulge in the surface. (a) The solid line indicates the hybrid solution, and the dashed line indicates the fully atomistic solution. (b) The solid line indicates the hybrid solution, and the dashed line indicates the fully continuum model solution. Reprinted from *Nie et al.* [2004] with the permission of Cambridge University Press.

is a local inward flux, particles are injected into the overlap region near to the outer boundary, keeping particles that are injected during the same time step as far away as possible from each other. In the simulations carried out by *Nie et al.* [2004] all the elements in the computational grid were of the same size. Figure 9 shows results from a full MD simulation, a hybrid MD-continuum model simulation, and a full continuum simulation of a flow in a channel with a raised area on the bottom wall [*Nie et al.*, 2004]. In the hybrid model, MD was used to simulate flow near the rough wall. It can be seen from Figure 9a that the hybrid solution agrees very well with the fully MD solution. Figure 9b shows that the fully continuum model solution significantly deviates from the hybrid solution indicating inadequacy of the continuum description of fluid flow near rough walls.

8. DISSIPATIVE PARTICLE DYNAMICS

[102] In dissipative particle dynamics (DPD) simulations [*Hoogerbrugge and Koelman*, 1992] a fluid is represented

by an ensemble of particles that move because of the combined effects of conservative (nondissipative), \mathbf{f}^C , dissipative, \mathbf{f}^D , fluctuating (random), \mathbf{f}^R , and external, \mathbf{f}^{ext} , forces, and the equation of motion is

$$dm_i \mathbf{v}_i / dt = \mathbf{f}_i^{int} + \mathbf{f}_i^{ext} = \mathbf{f}_i^C + \mathbf{f}_i^D + \mathbf{f}_i^R + \mathbf{f}_i^{ext} = \mathbf{f}_i^{ext} + \sum_{j \neq i} (\mathbf{f}_{ij}^C + \mathbf{f}_{ij}^D + \mathbf{f}_{ij}^R), \quad (120)$$

where \mathbf{v}_i is the velocity of particle i and m_i is its mass. In models for single-phase fluid flow, the conservative forces between particles are given by a simple purely repulsive form such as $\mathbf{f}_{ij}^C = S(1 - r_{ij}/r_0)\hat{\mathbf{r}}_{ij}$ for $r_{ij} = |\mathbf{r}_{ij}| < r_0$ and $\mathbf{f}_{ij}^C = 0$ for $r_{ij} \geq r_0$, where S is the strength of the particle-particle interaction, r_0 is the range of the particle-particle interactions, and $\hat{\mathbf{r}}_{ij}$ is the unit vector pointing from particle j to particle i ($\hat{\mathbf{r}}_{ij} = (\mathbf{x}_i - \mathbf{x}_j)/|\mathbf{x}_i - \mathbf{x}_j|$). The total force acting on particle i due to conservative forces is

$$\mathbf{f}_i^C = \sum_{j \neq i} \mathbf{f}_{ij}^C = \sum_{j \neq i, r_{ij} < r_0} S_{ij}(1 - r_{ij}/r_0)\hat{\mathbf{r}}_{ij}, \quad (121)$$

where S_{ij} is the strength of the interaction between particle i and particle j . The DPD particles can be considered to represent a cluster of atoms or molecules, and the dissipative and random interactions arise because of the internal degrees of freedom. The dissipative particle-particle interactions are given by $\mathbf{f}_{ij}^D = \gamma W^D(r_{ij})(\mathbf{r}_{ij} \cdot \mathbf{v}_{ij})\hat{\mathbf{r}}_{ij}$, where $\mathbf{v}_{ij} = \mathbf{v}_j - \mathbf{v}_i$, for $r_{ij} < r_0$ and $\mathbf{f}_{ij}^D = 0$ for $r_{ij} > r_0$ so that

$$\mathbf{f}_i^D = \sum_{j \neq i} \mathbf{f}_{ij}^D = - \sum_{j \neq i, r_{ij} < r_0} \gamma W^D(r_{ij})(\mathbf{r}_{ij} \cdot \mathbf{v}_{ij})\hat{\mathbf{r}}_{ij}, \quad (122)$$

and the random forces are given by $\mathbf{f}_{ij}^R = \sigma W^R(r_{ij})\zeta_{ij}\hat{\mathbf{r}}_{ij}$ for $r_{ij} < r_0$ and $\mathbf{f}_{ij}^R = 0$ for $r_{ij} > r_0$, where ζ is a random variable with a zero mean and a unit variance so that

$$\mathbf{f}_i^R = \sum_{j \neq i} \mathbf{f}_{ij}^R = \sum_{j \neq i, r_{ij} < r_0} \sigma W^R(r_{ij})\zeta_{ij}\hat{\mathbf{r}}_{ij}. \quad (123)$$

The random and dissipative particle-particle interactions are related through the fluctuation dissipation theorem [*Espanol and Warren*, 1995], which requires that $\gamma = \sigma^2/2k_B T$ and $W^D(r) = [W^R(r)]^2$. The combination of dissipative and fluctuating forces, related by the fluctuation dissipation theorem [*Kubo*, 1966], acts as a thermostat, which maintains the temperature of the system, measured through the average kinetic energy of the particles, at a temperature of T , providing that the time step used in the simulation is small enough. This idea can be taken one step further [*Lowe*, 1999] by integrating the equation of motion with only the conservative forces $\{\mathbf{f}_i^C\}$ over the time step, Δt , and then thermalizing the relative velocities of a fraction, f_T of the particle pairs separated by a distance of r_0 or less by randomly selecting the relative velocities from a Maxwell-Boltzmann distribution and multiplying by $\sqrt{2}$ to convert the Maxwell-Boltzmann single particle velocity distribution at temperature T to a relative velocity

distribution function and preserving the average velocity of the particle pairs to conserve momentum. The fraction, f_T , of particles that are “thermalized” at each step in the simulation can then be varied to change the effective viscosity of the fluid. An advantage of this approach is that it eliminates the problems associated with integration of stochastic differential equations, and the temperature, measured via the particle kinetic energy, deviates less from the temperature used in the DPD algorithm [Nikunen *et al.*, 2003].

[103] When DPD models are used to simulate liquids, the particles overlap extensively (there are several to several tens of particles in a volume of $4\pi r_o^3/3$). As the temperature is lowered from a large value, the DPD system undergoes a Kirkwood-Alder transition to a solid [Kirkwood, 1939; Alder and Wainright, 1962]. The transition temperature depends on the magnitude of the thermal energy relative to the interaction energy. As the number of atoms or molecules, N_p , represented by the DPD particle increases, the thermal energy, $k_B T/2$ per degree of freedom, where k_B is the Boltzmann constant, remains constant while the DPD particle-particle interaction increases in magnitude. This drives the system through the Kirkwood-Alder transition and limits the size of the cluster of atoms or molecules that the DPD particles can represent. For DPD simulations with interaction parameters that have been selected so that the DPD fluid properties match the properties of real liquids, the DPD particle mass can be no more than 10–100 times the atomic or molecular mass [Dzwinel and Yuen, 2000]. DPD can be regarded as thermostatted molecular dynamics with soft particle-particle interactions, and the DPD thermostat has been used in nonequilibrium molecular dynamics simulations [Guo *et al.*, 2002]. The soft particle-particle interactions allow much larger time steps to be taken, and this is a more important advantage than the larger particle size, relative to standard molecular dynamics, when DPD and MD are used to simulate multiphase fluid flow. The model DPD fluid is isotropic, Galilean-invariant, and momentum-conserving ($\mathbf{f}_{ij} = -\mathbf{f}_{ji}$).

[104] Since the particles used in DPD simulations represent a very small volume of fluid, they carry angular momentum, which is neglected when they are treated as point masses. Espanol [1998] developed the “fluid particle model,” which included the angular motion of the particles (the particles are endowed with both mass and moment of inertia). In addition to the standard DPD interparticle interaction forces, the conservative particle-particle interactions include a noncentral “shearing” force, and the dissipative particle-particle interactions include a rotational force (torque) component with the form

$$\mathbf{f}_{ij}^{\text{ROT}} = -\mu^R \mathbf{M}(\mathbf{r}_{ij}) \cdot [\mathbf{r}_{ij} \times (\boldsymbol{\omega}_i + \boldsymbol{\omega}_j)], \quad (124)$$

where $\boldsymbol{\omega}_i$ is the angular velocity of particle i and $\mathbf{M}(\mathbf{r}_{ij})$ is a matrix with the form $\mathbf{M}(\mathbf{r}_{ij}) = C_1(r_{ij})\mathbf{I} + C_2(r_{ij})\mathbf{e}_{ij}\mathbf{e}_{ij}$, where \mathbf{I} is the unit matrix, C_1 and C_2 are constants, and $\mathbf{e}_{ij} = \mathbf{r}_{ij}/r_{ij}$. This model conserves both angular and linear momentum, and it explicitly includes the effects of angular momentum

conservation at the particle scale. The random forces have the form

$$\mathbf{f}_{ij}^{R,n} dt = W^n(r_{ij}) \mathbf{W}_{ij}^n \cdot \mathbf{e}_{ij}, \quad (125)$$

where $W^n(r_{ij})$ are scalar functions of r_{ij} , and there are three independent stochastic components corresponding to traceless symmetric ($n = 1$, due to shear), diagonal ($n = 2$, due to compression), and antisymmetric ($n = 3$, due to rotational) dissipation matrices (\mathbf{W}_{ij}^n).

[105] One approach to the simulation of two-phase (liquid/gas) multiphase single-component systems is to use a conservative interaction force, \mathbf{f}_{ij}^C , that corresponds to a two-phase equation of state. In general, the conservative force acting on particle i is given by

$$\mathbf{f}_i^C = -\partial F^{\text{xs}} / \partial \mathbf{x}_i, \quad (126)$$

where F^{xs} is the excess free energy (the part of the free energy that exceeds the free energy of the corresponding DPD ideal gas due to interparticle interactions) and \mathbf{x}_i is the position of particle i . If the local density at particle i is assumed to be the sum of contributions from particle i and its neighbors with the form $n_i = 1/[w] \sum w_{ij}$ (w_{ij} is a smooth continuous weighting function, not necessarily related to the other weighting functions used in the DPD model, that vanishes at the cutoff distance, r_o , and $[w]$ is a normalization factor, which ensures that $n = \rho$, where $\rho(\mathbf{x})$ is the density, in a homogeneous fluid), then if particle i moves, the local particle density at particle i will change, and the local particle densities at its neighbors will also change. The changes in the densities of particle i and its neighbors result in corresponding changes in the local free energies, and the DPD model of Pagonabarraga and Frenkel [2001] for single-component two-phase fluids is based on the idea that the conservative force acting on particle i in a DPD fluid can be expressed as

$$\begin{aligned} \mathbf{f}_i^C &= - \sum_{j=1}^{j=N} \partial F^{\text{xs}}(n_j) / \partial \mathbf{x}_i \\ &= - \sum_j [\partial F^{\text{xs}}(n_i) / \partial n_i + \partial F^{\text{xs}}(n_j) / \partial n_j] \{ dw(r_{ij}) / dr_{ij} / [w] \} \hat{\mathbf{r}}_{ij}, \end{aligned} \quad (127)$$

where N is the total number of DPD particles in the system and $F^{\text{xs}}(n)$ is the local excess free energy per particle at a particle density of n . For example, for a van der Waals fluid (equation (34)), the pressure is given by $P = \rho k_B T / (1 - b'\rho) - a'\rho^2$, the excess free energy per particle under isothermal conditions, calculated using equation (34) ($-\int (P - \rho k_B T) dV = \int [(P - \rho k_B T) / \rho^2] d\rho$), is given by $F^{\text{xs}} = a'\rho - k_B T \ln(1 - b'\rho)$, and the pairwise conservative force is given by

$$\begin{aligned} \mathbf{f}_{ij}^C &= \{ [k_B T / (1 - b'n_i) - a'] + [k_B T / (1 - b'n_j) - a'] \} \\ &\cdot \{ [\partial w_{ij}(r) / \partial r_{ij}] / [w] \} \mathbf{e}_{ij}. \end{aligned} \quad (128)$$

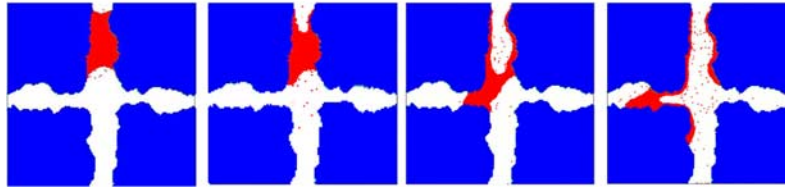


Figure 10. Four stages in a two-dimensional dissipative particle dynamics simulation of the penetration of a wetting fluid through a fracture junction [Meakin *et al.*, 2007].

Multicomponent, multiphase systems can be simulated by labeling the particles to identify which component they represent and using different repulsive interaction strengths (equation (121)) (S_{11} , S_{12} , S_{22} ...) with $S_{11} \ll S_{12}$, $S_{22} \ll S_{12}$, etc., to bring about phase separation [Coveney and Espanol, 1995]. However, this approach cannot be used to simulate single-component two-phase (liquid-vapor) systems. An alternative approach is to use a combination of short-range repulsive interactions and (relatively) long-range attractive interactions [Liu *et al.*, 2007]. This borrows from the physical origins of phase separation in single-component fluids (the combination of short-range repulsive and long-range attractive atom-atom and molecule-molecule interactions [van der Waals, 1873]). A combination of short-range repulsive and relatively long range attractive interactions between fluid particles and particles used to represent confining solid materials can also be used to realistically simulate different wetting conditions (velocity-dependent contact angle angles and contact line dynamics [e.g., Kong and Yang, 2006]). In addition a combination of “bounce back” boundary conditions and particle-particle interactions can be used to reduce slip at solid-liquid interfaces to negligible levels. These features were used in the simulation shown in Figure 10.

[106] Another approach to the DPD simulation of liquid gas systems is to use the method of Pagonabarraga and Frenkel [2001] with a two-phase equation of state, such as the van der Waals equation, and add a force with the form $\mathbf{f}_\Gamma^C = c\nabla\nabla^2\rho$ to the conservative force to represent the effect of surface tension [Tiware and Abraham, 2006] (see equation (19)). Here $c/2$ is the coefficient of the $(\nabla\rho)^2$ term in the free energy functional (see equations (11)–(15)).

[107] In dissipative particle dynamics simulations, the fluid(s) can be driven through a confining medium by body forces (representing gravity) acting on the particle masses, by injecting and removing particles near the system boundaries to represent flow boundary conditions or by adding and removing particles to maintain prescribed particle densities (pressures) near the system boundaries. Dissipative particle dynamics has not been as extensively applied as lattice Boltzmann methods to the simulation of multiphase fluid flow in the subsurface, and its advantages and disadvantages are less well understood. It is well suited to the simulation of nanoscale multiphase systems because the effects of thermal fluctuations, which can be important at very small scales [Kang and Landman, 2007], are properly included. Because of the soft particle-particle interactions, the compressibility of DPD fluids is large relative to real

liquids, except for liquids near the critical point. For lattice Boltzmann models, the simplicity of the microdynamics allows quantities such as the fluid viscosity to be analytically calculated, and the lattice Boltzmann model is more computationally efficient than DPD. On the other hand, DPD is numerically stable and rigorously Galilean invariant under all conditions. DPD methods have been applied quite extensively to systems such as polymer solutions, colloids, emulsions (surfactants), membranes, etc. In these applications, DPD serves as a coarse-grained nonequilibrium molecular dynamics model, and it retains sufficient molecular level detail to investigate the effects of the size, shape, and rigidity of large molecules, and their intermolecular interactions, on the behavior of soft condensed matter. DPD could be applied to simulate the behavior of colloids (both biocolloids and mineral colloids), biopolymers, biofilm, and other soft condensed matter in the subsurface.

9. SMOOTHED PARTICLE HYDRODYNAMICS MODELS

[108] SPH was introduced 30 years ago to simulate astrophysical fluid dynamics [Lucy, 1977; Gingold and Monaghan, 1977; Monaghan, 1992]. SPH is based on the idea that a continuous field, $A(\mathbf{r})$, can be represented by a superposition of smooth bell-shaped functions, $W(|\mathbf{r} - \mathbf{r}_i|)$ (usually referred to as the smoothing function or weighting function), centered on a set of points, $\{\mathbf{r}_i\}$, and the gradient of the field is given by the same superposition of the gradients of the smoothing function. A set of extensive properties, such as the particle mass, m_i , is associated with each particle, and in this case the mass can be thought of as being smoothed or smeared by the smoothing function so that the contribution of particle i to the fluid density field, $\rho(\mathbf{r})$, is given by $\rho^i(\mathbf{r}) = m_i W(|\mathbf{r} - \mathbf{r}_i|)$, where the smoothing function is normalized so that $\int W(\mathbf{r}) d\mathbf{r} = 1$. Consequently, the density field is given by

$$\rho(\mathbf{r}) = \sum_i \rho^i(\mathbf{r}) = \sum_i m_i W(\mathbf{r} - \mathbf{r}_i, h). \quad (129)$$

More generally, the intensive field $A(\mathbf{r})$ is given by

$$\begin{aligned} A(\mathbf{r}) &= \sum_i A^i(\mathbf{r}) = \sum_i a_i W(\mathbf{r} - \mathbf{r}_i, h) \\ &= \sum_i (m_i A_i / \rho_i) W(\mathbf{r} - \mathbf{r}_i, h), \end{aligned} \quad (130)$$

and the gradient of A is given by

$$\nabla A(\mathbf{r}) = \sum_i (m_i A_i / \rho_i) \nabla W(\mathbf{r} - \mathbf{r}_i, h). \quad (131)$$

(The standard SPH formulation [Gingold and Monaghan, 1977; Lucy, 1977] is based on the identity $A(\mathbf{r}) = \int A(\mathbf{r}') \delta(\mathbf{r} - \mathbf{r}') d\mathbf{r}'$, where \mathbf{r} and \mathbf{r}' are position vectors and δ is the Kronecker delta function. If the δ function is replaced by the smoothing function $W(\mathbf{r} - \mathbf{r}', h)$, $A(\mathbf{r}) = \int A(\mathbf{r}') W(\mathbf{r} - \mathbf{r}', h) d\mathbf{r}'$, where $\int W(\mathbf{r}, h) d\mathbf{r} = 1$, $A(\mathbf{r})$ is a smoothed version of $A(\mathbf{r}')$, and if the field A is defined by a set of points that carry masses m_i , the density field is given by $\rho(r) = \sum_i m_i W(\mathbf{r} - \mathbf{r}_i, h)$ and $A(r) = \sum_i (m_i / \rho_i) A_i W(\mathbf{r} - \mathbf{r}_i, h)$, which is equation (130).)

[109] The SPH equations for continuous fields can also be expressed in terms of the particle number density, $n_i = \sum_i W(\mathbf{r} - \mathbf{r}_i, h)$, as

$$A(\mathbf{r}) = \sum_i (A_i / n_i) W(\mathbf{r} - \mathbf{r}_i, h), \quad (132)$$

$$\nabla A(\mathbf{r}) = \sum_i (A_i / n_i) \nabla W(\mathbf{r} - \mathbf{r}_i, h). \quad (133)$$

The SPH equation for the flow of an inviscid fluid is based on the equation of motion

$$d\bar{\mathbf{v}}/dt = -\nabla P / \rho, \quad (134)$$

where $\bar{\mathbf{v}}$ is the local fluid velocity and ∇P is the pressure gradient. The pressure gradient field is obtained from the density field via the equation of state and the identity $\nabla P / \rho = \nabla(P/\rho) + (P/\rho^2) \nabla \rho$. The resulting equation of motion is

$$\frac{d\mathbf{v}_i}{dt} = - \sum_j m_j \left(\frac{P_i}{\rho_i^2} + \frac{P_j}{\rho_j^2} \right) \nabla_i W(\mathbf{r}_i - \mathbf{r}_j, h), \quad (135)$$

where \mathbf{v}_i is the velocity of particle i and ∇_i is the gradient operator with respect to \mathbf{r}_i . This is one of many possible SPH formulations of the Euler equation for inviscid fluid flow. The point particles in the SPH method can be thought of in terms of a moving (Lagrangian) disordered grid, and there are many ways of solving differential equations using SPH, just as there are many possible ways of formulating fluid flow equations using regular grids. In practice, equation (135) cannot be used to simulate the Euler equation because the particles in an SPH simulation move between regions with different velocities, thus creating a viscosity due to momentum diffusion, in the same way that viscosity is created in molecular dynamics simulations (without including viscous forces in the equation of motion) and in simple fluids [Hoover, 1998].

[110] If a body force, such as the effects of gravity acting on the fluid density, is added, the equation of motion becomes

$$\frac{d\mathbf{v}_i}{dt} = - \sum_j m_j \left(\frac{P_i}{\rho_i^2} + \frac{P_j}{\rho_j^2} \right) \nabla_i W(\mathbf{r}_i - \mathbf{r}_j, h) + \mathbf{f}_i / m_i, \quad (136)$$

where \mathbf{f}_i is the body force per unit mass. In many applications $\mathbf{f}_i = m_i \mathbf{g}$, where \mathbf{g} is the gravitational acceleration.

[111] Since the first applications of SPH were in the area of astrophysics, where viscous forces usually do not play a significant role, it was almost 20 years until the effects of viscosity were included in SPH simulations [Takeda et al., 1994; Posch et al., 1995], apart from the addition of “artificial viscosity” to improve the numerical stability of SPH models. In SPH simulations, the effects of viscosity on fluid flow can be included by adding an SPH formulation of the “ $\eta \nabla^2 \mathbf{v}$ ” or “ $\nabla \cdot \{ \eta \cdot [\nabla \otimes \mathbf{v} + (\nabla \otimes \mathbf{v})^T] \}$ ” viscous dissipation term in the Navier-Stokes equation (equation (4)), and the equation of motion becomes [Morris et al., 1997; Zhu et al., 1997, 1999]

$$\begin{aligned} \frac{d\mathbf{v}_i}{dt} = & - \sum_j m_j \left(\frac{P_i}{\rho_i^2} + \frac{P_j}{\rho_j^2} \right) \nabla_i W(\mathbf{r}_i - \mathbf{r}_j, h) \\ & + \sum_j \frac{m_j (\eta_i + \eta_j) (\mathbf{v}_i - \mathbf{v}_j)}{\rho_i \rho_j |\mathbf{r}_i - \mathbf{r}_j|^2} (\mathbf{r}_i - \mathbf{r}_j) \cdot \nabla_i W(\mathbf{r}_i - \mathbf{r}_j, h) + \mathbf{g}. \end{aligned} \quad (137)$$

Here \mathbf{v}_i is the velocity of particle i and η_i is the fluid viscosity at particle i (the viscosity can vary spatially in multiphase and/or multicomponent systems). The corresponding equation of motion based on the particle number density, n , is $m_i d\mathbf{v}_i/dt = \mathbf{f}_i$, where

$$\begin{aligned} \mathbf{f}_i = & - \sum_j \left(\frac{P_i}{n_i^2} + \frac{P_j}{n_j^2} \right) \nabla_i W(\mathbf{r}_i - \mathbf{r}_j, h) \\ & + \sum_j \frac{(\eta_i + \eta_j) (\mathbf{v}_i - \mathbf{v}_j)}{n_i n_j |\mathbf{r}_i - \mathbf{r}_j|^2} (\mathbf{r}_i - \mathbf{r}_j) \cdot \nabla_i W(\mathbf{r}_i - \mathbf{r}_j, h) + m_i \mathbf{g}. \end{aligned} \quad (138)$$

In theoretical work on SPH it is often convenient to use a Gaussian form for the smoothing function. However, in numerical investigations a variety of spline functions with a finite range, h , have been used, and the smoothing function, $W(|\mathbf{r}|)$, in the above equations may be replaced by $W(|\mathbf{r}|, h)$ to emphasize this. The use of a finite range for the smoothing function is important in SPH simulations for the same reason that a finite interaction range is important in MD simulations: the summations in equations such as (137) and (138) can be truncated and “ \sum_j ” can be replaced by “ $\sum_{j, r_{ij} < h}$,” thus reducing the order of the SPH algorithm from $O(n^2)$ to $O(n)$, where n is the number of particles. An

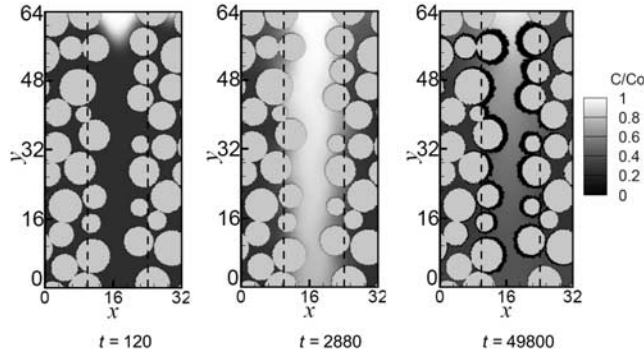


Figure 11. SPH simulation of reactive transport and precipitation in a porous medium with a microfracture. The Damkohler number was $Da = 2.548$, and the Peclet numbers prior to precipitation were $Pe_m = 0.082$ for the matrix and $Pe_f = 22.82$ for the fracture. The gray particles represent mineral grains, and the black particles represent precipitated mineral. The gray scale denotes the dimensionless concentration, C/C_0 . A solution with a solute concentration of $C_0 = 4C_{eq}$ was injected into the fractured porous medium, which was initially filled with a solution having a solute concentration of C_{eq} . The solution was injected at the upper boundary located at $y = 64$ [Tartakovsky *et al.*, 2007b].

example is the fourth-order spline smoothing function [Zhu *et al.*, 1999]

$$W(\mathbf{r}, h) = \alpha \begin{cases} \left(3 - \frac{3|\mathbf{r}|}{h}\right)^5 - 6\left(2 - \frac{3|\mathbf{r}|}{h}\right)^5 + 15\left(1 - \frac{3|\mathbf{r}|}{h}\right)^5 & 0 \leq |\mathbf{r}| < h/3 \\ \left(3 - \frac{3|\mathbf{r}|}{h}\right)^5 - 6\left(2 - \frac{3|\mathbf{r}|}{h}\right)^5 & h/3 \leq |\mathbf{r}| < 2h/3 \\ \left(3 - \frac{3|\mathbf{r}|}{h}\right)^5 & 2h/3 \leq |\mathbf{r}| < h \\ 0 & h < |\mathbf{r}| \end{cases} \quad (139)$$

where $\alpha = 63/(478\pi h^2)$ and $\alpha = 81/(359\pi h^3)$ in two and three spatial dimensions.

[112] To simulate fluid flow in confined systems such as porous media and fractured porous media it is convenient to use stationary particles to represent the confining solid phase with a combination of short-range repulsive interactions and (relatively) long-range attractive interactions between the liquid particles and the solid particles. Bounce back boundary conditions (reversal of particle velocities) can be used to return to the fluid particles that penetrate too far into the solid, and if this is done, only a thin layer of solid particles near the solid-fluid interface is needed. The summations in equation (138) are over all particles including solid particles. For nondeformable porous media, the velocities of the SPH particles that represent solids in equation (138) are set to zero, and viscosities associated with the solid particles are assumed to be equal to the fluid viscosity (η_j is set equal to η_i in equations (137) and (138) when particle j is a solid particle).

[113] SPH can also be used to simulate diffusion and dispersion. In a coordinate system moving with the fluid the

effects of diffusion can be calculated from

$$\frac{dC_i}{dt} = \frac{1}{m_i} \sum_{j \in \text{fluid}} \frac{(\mathcal{D}_i n_i m_i + \mathcal{D}_j n_j m_j)(C_i - C_j)}{n_i n_j (\mathbf{r}_i - \mathbf{r}_j)^2} (\mathbf{r}_i - \mathbf{r}_j) \cdot \nabla_i W(\mathbf{r}_i - \mathbf{r}_j, h), \quad (140)$$

where C_i is the solute concentration (mass of solute carried by particle i divided by the mass of solution carried by particle i) and \mathcal{D}_i is the molecular diffusion coefficient associated with particle i .

[114] The SPH discretization of the advection-diffusion-reaction equation with heterogeneous (dissolution or precipitation) reaction kinetics of the form $k(C - C_{eq})^\beta$, where C is the solute concentration at the liquid-solid interface and C_{eq} is the solute concentration at equilibrium with the solid, is

$$\frac{dC_i}{dt} = \frac{1}{m_i} \sum_{j \in \text{fluid}} \frac{(\mathcal{D}_i n_i m_i + \mathcal{D}_j n_j m_j)(C_i - C_j)}{n_i n_j (\mathbf{r}_i - \mathbf{r}_j)^2} (\mathbf{r}_i - \mathbf{r}_j) \cdot \nabla_i W(\mathbf{r}_i - \mathbf{r}_j, h) - k(C_i - C_{eq})^\beta \sum_{k \in \text{solid}} \Delta_k \frac{W(\mathbf{r}_i - \mathbf{r}_k, h)}{\sum_{l \in \text{fluid}} n_l W(\mathbf{r}_k - \mathbf{r}_l, h)}, \quad (141)$$

where k is the rate constant, β is the order of the heterogeneous reactions, and Δ_k denotes the reactive surface area (length in two-dimensional simulation) associated with solid particle k . In equation (141) $\sum_{j \in \text{fluid}}$ indicates summation over all fluid particles, and $\sum_{j \in \text{solid}}$ indicates summation over all solid particles. The last term in equation (141) is proportional to the rate of the mass loss/gain (per unit mass of solution) due to the precipitation/dissolution reaction. Mass conservation requires the rate of solid mass gain/loss due to precipitation or dissolution to be

$$\frac{dm_k}{dt} = \frac{k \Delta_k}{\sum_{l \in \text{fluid}} n_l W(\mathbf{r}_k - \mathbf{r}_l, h)} \sum_{i \in \text{fluid}} m_i (C_i - C_{eq})^\beta W(\mathbf{r}_i - \mathbf{r}_k, h). \quad (142)$$

Homogeneous reactions can be included by adding terms in the right-hand side of equation (141). For example, if the solute is unstable or reacts with itself, the term $-rC_i^\alpha$, where α is the order of the reaction, can be added to the right-hand side of equation (140) or (141).

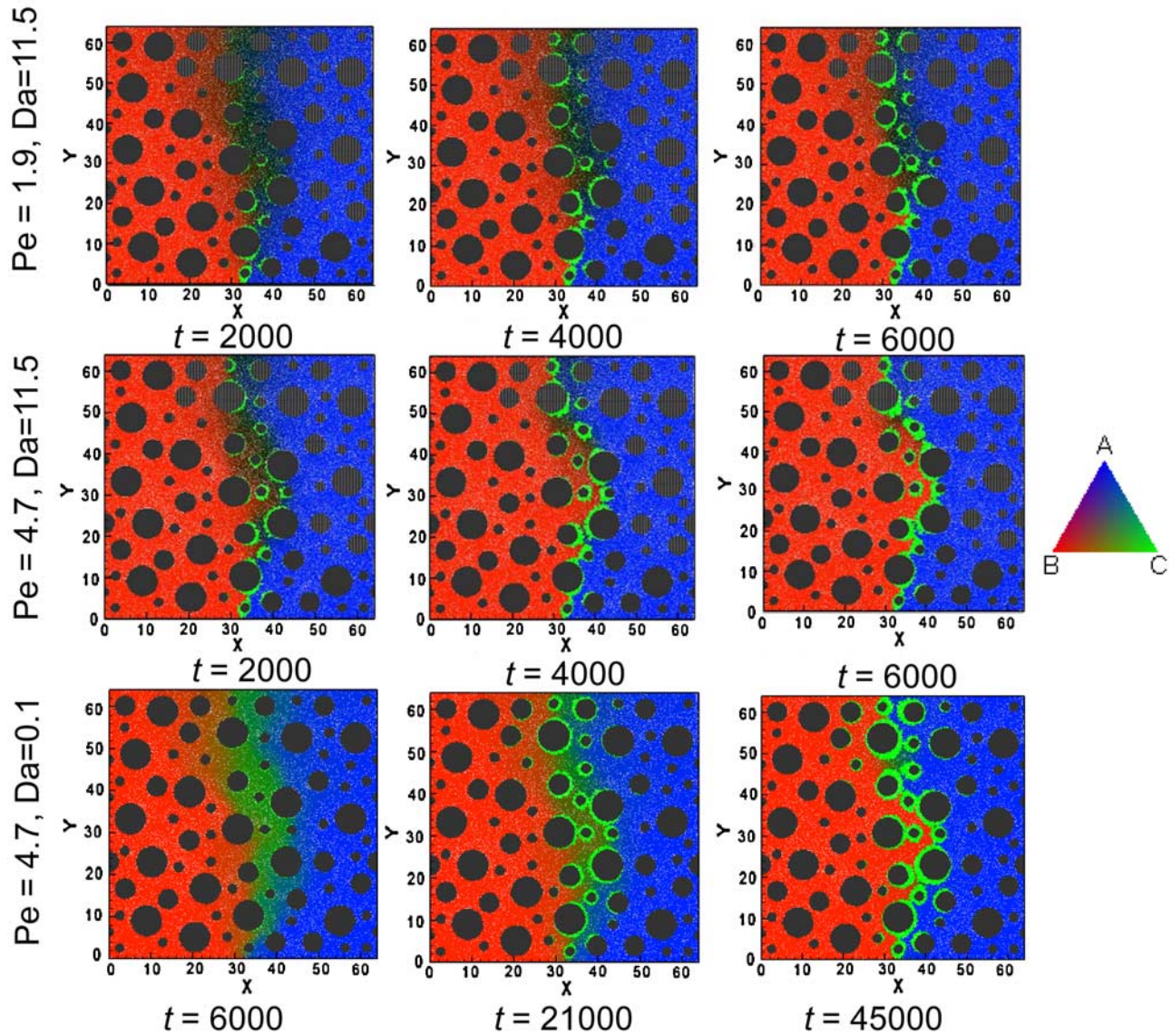


Figure 12. Two-dimensional SPH simulations of precipitation resulting from the mixing of two reactive solutions in a porous medium at two different Peclet numbers. The solutes A (red particles) and B (blue particles) were injected at the same rate into the right and left parts of the computational domain. As the solutions mix, A and B react and produce the product C , which precipitates on mineral surfaces. The color scale indicates the concentrations of A , B , and C . The gray particles represent mineral grains, and the green particles are precipitated solid C [Tartakovsky *et al.*, 2008a].

[115] Precipitation and dissolution processes can be modeled by using an approach similar to that employed in lattice Boltzmann model simulations [Kang *et al.*, 2004]. The masses, m_i , of the solid particles are tracked, and once the mass of a solid particle, m_k , exceeds $2m_k^0$, where m_k^0 is the mass of the mineral phase with a volume of $1/n_k$ (where n_k is the SPH particle number density in the solid), the nearest fluid particle “precipitates,” becoming a new solid particle, and the mass of the new solid particle is set to $m_i - m_k^0$ while the mass of the old solid particle becomes m_k^0 . Similarly, if the mass of a solid particle reaches zero, the solid particle becomes a new fluid particle. Since the fluid velocity adjacent to a solid surface is very small, the velocity of the

new fluid particle is set to zero, and the concentration of the fluid particle is set to the equilibrium concentration.

[116] Figure 11 illustrates an SPH simulation of the injection of a supersaturated solution into a fractured porous medium that was initially saturated with a solution at equilibrium with the solid. In the simulation the precipitate eventually completely seals the fracture walls.

[117] Figure 12 illustrates simulations of multicomponent reactive transport in a two-dimensional porous medium. Solutions of A and B were injected in two different halves of a porous medium, and the product of homogeneous reaction



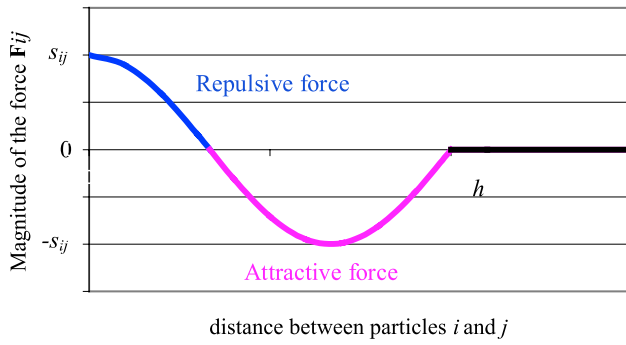


Figure 13. Example of a combination of short-range repulsive and (relatively) large-range attractive particle-particle interactions that can be used to control phase separation, surface tension, and wetting behavior in SPH simulations. The example is defined by equation (146), but a variety of interactions with similar general forms can be used successfully.

precipitated on the soil grains once its concentration $[C]$ exceeded the equilibrium concentration, C_{eq} . The simulations showed that the precipitate formed a thin layer in the mixing zone and that the precipitate layer significantly reduced the mixing between the two reactants, A and B . To prevent dissolution due to reduced mixing, the injected solutions contained C with a concentration of C_{eq} . The simulations show that the rate of precipitation increases with increasing Peclet number and the width of the precipitation zone decreases with increasing Damkohler number.

[118] Because the precipitate separating the two solutions has a width on the order of the grain diameter, continuum-scale simulations would provide misleading results (the amount of precipitation required would be seriously overestimated). On the other hand, pore-scale simulations cannot be used to simulate large-scale processes. In this case a multiscale multiresolution model that uses small SPH particles to simulate the precipitation zone and large SPH particles to simulate solute dispersion can be used [Tartakovsky *et al.*, 2008b].

[119] Formal similarities between SPH and MD simulations [Hoover, 1998] have been used as a basis for an SPH model for multiphase immiscible fluids [Tartakovsky and Meakin, 2006]. In this model, the momentum conservation equation for each particle is written in the form

$$m_i \frac{d\mathbf{v}_i}{dt} = \mathbf{f}_i^h + \mathbf{f}_i^{\text{int}}. \quad (144)$$

In equation (144), the total force acting on each particle is a combination of the “hydrodynamic” force, \mathbf{f}_i^h , given by equation (138) and the interaction force,

$$\mathbf{f}_i^{\text{int}} = \sum_j \mathbf{f}_{ij}, \quad (145)$$

resulting from the molecular-like pair-wise fluid-solid and fluid-fluid particle-particle interaction forces, \mathbf{f}_{ij} . The exact form of these particle-particle interactions is not critical to the success of the SPH model (generation of the correct

multiphase behavior with surface tensions that satisfy the Young-Laplace equation) providing they have a short-range repulsive component and a (relatively) long-range attractive component, with a cutoff to reduce the computational burden. For example, interaction forces with the form

$$\begin{aligned} \mathbf{f}_{ij} &= s_{ij} \cos(1.5\pi|\mathbf{r}_i - \mathbf{r}_j|/h) (\mathbf{r}_i - \mathbf{r}_j) / |\mathbf{r}_i - \mathbf{r}_j| \quad \text{for } |\mathbf{r}_i - \mathbf{r}_j| \leq h \\ \mathbf{f}_{ij} &= 0 \quad \text{for } |\mathbf{r}_i - \mathbf{r}_j| > h, \end{aligned} \quad (146)$$

shown in Figure 13, where s_{ij} is the strength of the pair-wise particle-particle interaction forces, have been used in most simulations of this type. However, forces corresponding to interaction potentials consisting of a combination of positive (repulsive) short-range polynomial spline functions (like that given in equation (139)) and longer-range negative (attractive) spline functions have also been used successfully.

[120] The compressibility of the SPH fluid is determined by the equation of state and the additional particle-particle interaction forces used to bring about phase separation. If the compressibility is low, smaller time steps are required, and SPH simulations become impractical for very low compressibility liquids. In this case, the related moving-particle semi-implicit (MPS) method [Koshizuka and Oka, 1996] could be used. The MPS method imposes incompressibility by correcting the particle velocities to maintain a constant particle number density. However, the correction depends on the pressure gradient, and a pressure Poisson equation must be solved to determine the pressure field. This adds a substantial computational burden, which is not justified if the compressibility effects in the SPH simulation are small.

[121] Particles representing solid phase are fixed in space but enter into the summation in equations (145) to avoid a large nonphysical decrease in fluid density near the fluid-solid boundary and to control the wetting behavior. The forces entering equation (145) are antisymmetric, and as a result, linear momentum is exactly conserved. The interaction strength s_{ij} between particles i and j depends on which fluid components or solid phases the particles represent. If the interaction strength, s_{ij} , between dissimilar particles is smaller than the interaction strength, s_{ii} and s_{jj} between like particles, the particle-particle interaction forces prevent the fluids represented by the dissimilar particles from mixing and create a surface tension. (For the interactions used in the simulations, mixing is controlled primarily by the relatively long range attractive component. The particle number densities in the fluid phases are controlled primarily by the short-range component and the effective particle-particle interaction forces generated by the ideal gas equation of state. The long-range attractive component of the fluid-solid particle-particle interactions dominates the wetting behavior.) Various wetting conditions are modeled by making the interaction strength between solid or boundary particles and the wetting fluid particles larger than the interaction strength between the solid particles and the nonwetting fluid particles. For single-component fluids, the strength of wetting for the liquid phase is determined by the strength

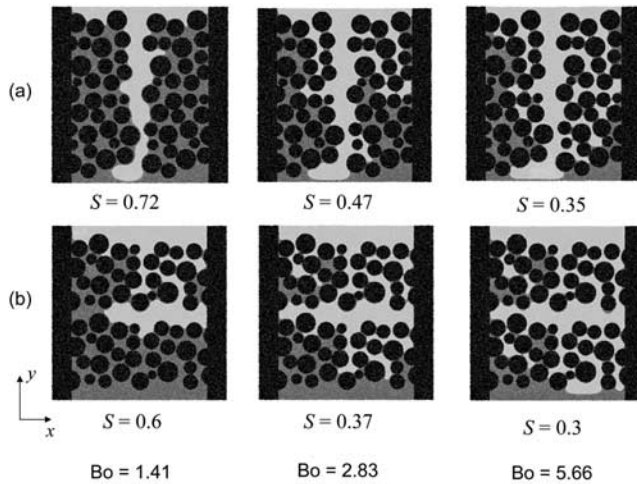


Figure 14. Drainage (gravity acting vertically) of a wetting liquid from a porous medium containing a microfracture. Equilibrium distribution of fluids for three different Bond numbers. Reprinted with permission from *Tartakovsky et al.* [2007c], copyright 2007, American Institute of Physics.

of the fluid-boundary particle-particle interactions relative to the strength of the fluid-fluid particle-particle interactions. The short-range repulsive part of the fluid-particle/boundary-particle interactions also simulates no-flow boundary conditions. However, these repulsive interactions may not be sufficiently strong to prevent all particles from penetrating the solid regions, and they may be combined with bounce back of particles that penetrate the boundaries. An equation of state is used to calculate the pressure needed to close the system of flow equations. An ideal gas equation of state, $P_i = P_o n_i = c^2 n_i$, is often used. In addition, particle-particle interactions in conjunction with an equation of state can be used to simulate unconfined liquid drops [Tartakovsky and Meakin, 2005a, 2005b]. (A two-phase equation of state can be used as an alternative to particle-particle interactions in conjunction with an ideal equation of

state. However, the “artificial” surface tension [Hoover, 1998; Colagrossi and Landrini, 2003] generated by models of this type is very weak, and it is necessary to add additional forces corresponding to the capillary stress gradient (equations (20)–(23)) to obtain liquid drops with smooth surfaces.)

[122] Figure 14 illustrates SPH simulations of fluid drainage from a fractured porous medium. The fractured porous medium was drained by incrementally increasing the gravitational force. These simulations mimic the approach commonly used in the laboratory to measure capillary pressure/saturation, P_c/S , relationships. Figure 14 shows the equilibrium distribution of the strongly wetting liquid for three Bond numbers, Bo (dimensionless P_c), during drainage with the same microfracture orientated perpendicular and parallel to the direction of the gravitational forces. The orientation of the microfracture has a large effect on the equilibrium distribution of the fluids for all values of the Bond number used in the simulations and on the S/Bo relationship (Figure 15). The S/Bo curve for the vertical fracture exhibits a “dual-domain” behavior. One part corresponds to the drainage from the fracture with a smaller entry pressure, and the second part corresponds to drainage from the porous matrix with a larger entry pressure. The horizontal microfracture creates a local capillary barrier effect because the liquid must overcome a capillary pressure difference to enter the wider microfracture from the narrower pores. The SPH method had been also used to simulate pore-scale dissolution of the trapped nonaqueous phase liquids, pore-scale miscible nonreactive flows [Zhu and Fox, 2002; Tartakovsky and Meakin, 2005c], and single-component and multicomponent reactive transport and precipitation [Tartakovsky et al., 2007a, 2007b].

10. TRADITIONAL GRID-BASED COMPUTATIONAL FLUID DYNAMICS

[123] For most applications, numerical solution of the Navier-Stokes equations (computational fluid dynamics

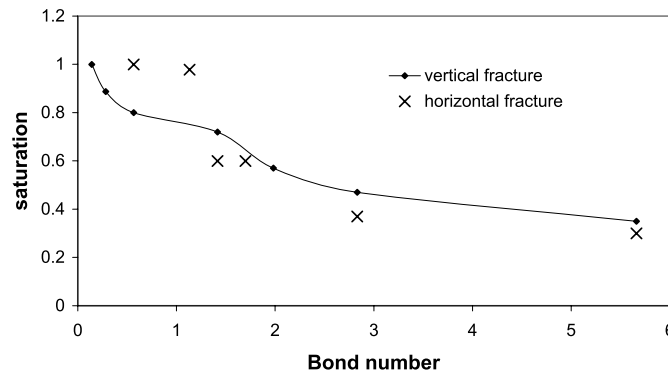


Figure 15. The Bo (or P_c)–saturation relationship during the drainage of the strongly wetting liquid in the fractured medium (illustrated in Figure 13) when the microfracture is oriented perpendicular and parallel to the direction of the gravitational field. Reprinted with permission from *Tartakovsky et al.* [2007c], copyright 2007, American Institute of Physics.

(CFD)) using a traditional grid-based method such as a finite volume, finite difference, or finite element formulation is the preferred approach because of its superior numerical efficiency and its ability to simulate fluid flow with very large density and viscosity ratios. However, the application of standard CFD to multiphase fluid flow in confined systems such as fractured and porous media with small characteristic lengths (pore diameters and fracture aperture widths, for example) has been inhibited by two difficulties: (1) the challenge of tracking the complex dynamics of fluid-fluid interfaces and (2) the need for a contact line/contact angle model that can be coupled with the CFD simulation. A variety of methods have been developed to track fluid-fluid interfaces [Unverdi and Tryggvason, 1992; Glimm *et al.*, 1999; Sethian, 1999, and references therein], and this difficulty has been largely overcome. However, as the discussion in section 3 indicates, the information and understanding required for a detailed treatment of the contact line/contact angle dynamics are still lacking. Several relatively simple interface tracking methods including the level set, volume of fluid, and phase field methods have been developed and demonstrated to work well, even when the interfaces undergo topological changes such as fluid fragmentation and coalescence. In addition, some of these methods have been implemented in conjunction with contact angle models.

[124] Some of the most frequently used interface tracking, or interface capturing, methods are based on an indicator function, $f_{\text{ind}}(\mathbf{x})$ (or a set of $n - 1$ indicator functions if there are n distinct fluid phases), which is advected with the flow. For two-phase fluids, the level set method is based on an indicator function, $f_{\text{ls}}(\mathbf{x})$, that is positive in regions occupied by one phase and negative in regions occupied by the other. In a d -dimensional computational domain, the fluid-fluid interface can be thought of as the d -dimensional cut through the surface $(\mathbf{x}, f_{\text{ls}}(\mathbf{x}))$ at $f_{\text{ls}} = 0$ in the $d + 1$ -dimensional $(\mathbf{x}, f_{\text{ls}})$ space. The evolution of the level set function due to flow is given by

$$\partial f_{\text{ls}} / \partial t = -\mathbf{v} \cdot \nabla f_{\text{ls}}, \quad (147)$$

where \mathbf{v} is the fluid velocity. For level set methods, the indicator function is the signed distance function, which has a magnitude at position \mathbf{x} equal to the shortest distance between \mathbf{x} and the interface ($|\nabla f_{\text{ls}}| = 1$) and a sign that is positive on one side of the interface (in fluid 1) and negative on the other side (in fluid 2). The curvature of the level set function is given by

$$\mathcal{K} = \nabla \cdot (\nabla f_{\text{ls}} / |\nabla f_{\text{ls}}|), \quad (148)$$

and the curvature of the interface needed to calculate the surface tension force acting on the interface is the curvature of the level set function at $f_{\text{ls}} = 0$. One approach to including the effects of surface tension in the model, often referred as a continuous surface tension force model [Brackbill *et al.*, 1992], is to replace the pressure jump at a sharp interface by a body force, integrated across the interface, that acts only on

the fluid near the interface [Sussman *et al.*, 1999]. The sharp interface is replaced by a function, $T(\mathbf{x}) = T[\varepsilon(\mathbf{x})]$, which varies smoothly from 0 to 1 as the distance from the interface, ε , varies from $-w/2$ to $w/2$, where w is the width of the interface. The force per unit volume acting on the fluid is then given by

$$\mathbf{f}_V = \rho \dot{\mathbf{v}} = \mathcal{K} \nabla T \mathbf{T}. \quad (149)$$

Since advection deforms the signed distance function, it must be frequently reconstructed. Fortunately, the signed distance function is needed only near the interface (where the signed distance function has a value of zero). Fast methods have been developed for reconstructing the signed distance function [e.g., Sethian, 1999; Adalsteinsson and Sethian, 1999; Osher and Fedwick, 2003], and consequently, this does not incur a prohibitive computational burden.

[125] A number of methods have been developed to evolve the indicator function, $f_{\text{ind}}(\mathbf{x}, t)$, once the velocity field, $\mathbf{v}(\mathbf{x}, t)$, has been calculated through the Navier-Stokes equation. The level set method handles topological changes (coalescence and fragmentation) very well. However, mass conservation is often significantly violated. Particle level set [Enright *et al.*, 2002] and adaptive mesh refinement [Nourgaliev and Theofanous, 2007] methods have been developed to improve mass conservation. In the particle level set method, particles with different labels are inserted on opposite sides of the interface and advected with the flow, and the interface is corrected throughout the simulation to ensure that it continues to separate particles with different labels. Since the Lagrangian particles accurately follow the flow, they can be used to correct the distorted level set function in underresolved regions. The applications of the level set method to multiphase fluid flow in the subsurface would require coupling with a contact angle model, and boundary conditions would be implemented in the same way as in large-scale computational fluid dynamics applied to problems such as flow in pipes, cooling systems, pumping equipment, etc.

[126] The indicator function used in the volume of fluid (VOF) method is the set of volume fractions $\{F_V^n\}$ in each element of the computational grid ($F_{V,i}^n = \phi_i^n$, where ϕ_i^n is the volume fraction of phase n in the i th grid element). In the case of an n -phase system only $n - 1$ volume fractions, ϕ_i , are needed to define the composition of the fluid in each grid element (cell) because $\sum_n \phi_i^n = 1$. In the case of a two-phase fluid, the volume fractions $\{F_V = F_V^1\}$ for a single phase are sufficient. $F_{V,i} = 1$ if the i th cell is completely filled with phase 1, $F_{V,i} = 0$ if the i th cell is completely filled with phase 2, and $0 < F_{V,i} < 1$ if part of the fluid-fluid interface passes through the i th cell. Since the volume fraction, $F_{V,i}$, is not sufficient to determine the direction and position of the part of the interface in the i th cell, an interface reconstruction algorithm [Rider and Koth, 1998] based on $F_{V,i}$ and the volume fractions in neighboring cells is needed. First, the orientation of the interface segment that cuts the i th cell is determined from the volume fraction gradient, $\nabla F_{V,i}$, treating F_V as if it were a continuous

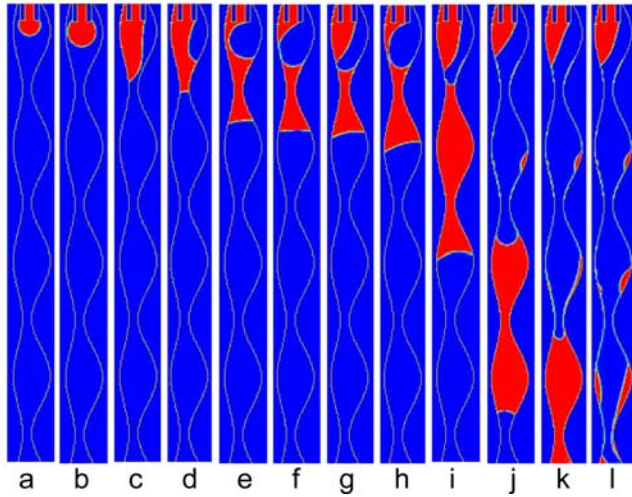


Figure 16. Two-dimensional simulation of the injection of a liquid into an aperture with sinuous walls. Snapshots after (a) 0.5, (b) 1.0, (c) 1.9, (d) 2.0, (e) 2.1, (f) 2.2, (g) 2.9, (h) 3.0, (i) 7.5, (j) 8.2, (k) 8.3, and (l) 8.5 s. The computational domain is 20 mm high, and the width is 3 mm [Huang *et al.*, 2005].

function. Then the unit vector normal to the interface is obtained from

$$\mathbf{n} = \nabla F_V / |\nabla F_V|, \quad (150)$$

and this defines the orientation of the interface.

[127] In liquid-gas simulations the indicator function is usually given a value of unity in the liquid phase and zero in the gas phase, and under these circumstances \mathbf{n} points into the liquid phase. The value of \mathbf{n} , calculated using equation (150), in cell i containing part of the interface and the volume fraction, F_i , in that cell provide sufficient information to specify the surface segment inside the i th cell (in general, the surface segments in adjacent cells are disjointed). During the next step in a simulation, the interface is then advected with the local velocity \mathbf{v}_i through a distance of $\mathbf{v}_i \delta t$, where δt is the time step.

[128] To simulate multiphase fluid flow, the curvature, $\mathcal{K}(\mathbf{x}_s)$, at position \mathbf{x}_s on the fluid-fluid interface is required to calculate the pressure jump caused by surface tension ($\Delta P = \Gamma \mathcal{K}(\mathbf{x}_s)$). In the VOF simulation, the effects of surface tension are expressed in terms of a body force that acts on the fluid in cells near the interface where the gradient of the indicator function, ∇F_V , is nonzero. These body forces are given by [Brackbill *et al.*, 1992]

$$F(\mathbf{x}_{\text{int}}) = \Gamma \mathcal{K}(\mathbf{x}_{\text{int}}) \nabla F_V(\mathbf{x}_{\text{int}}), \quad (151)$$

where \mathbf{x}_{int} is in the interface zone, and the curvature is calculated using equation (148). This is very similar to the method used in level set interface capturing.

[129] To simulate multiphase fluid flow in the presence of solids, a fluid-fluid-solid contact angle model must be coupled with the VOF simulation. In two-dimensional

simulations, this can be done by imposing the boundary condition

$$\mathbf{n}(\mathbf{x}_s) = \mathbf{n}_w(\mathbf{x}_s) [\cos(\theta)] + \mathbf{n}_t(\mathbf{x}_s) [\sin(\theta)] \quad (152)$$

in the grid nodes located at the wall, where θ is the contact angle measured in phase 1, $\mathbf{n}_w(\mathbf{x}_s)$ is the unit vector normal to the solid-fluid interface pointing into the solid, and $\mathbf{n}_t(\mathbf{x}_s)$ is the unit vector tangent to the solid-fluid interface pointing toward phase 1 [Sikalo *et al.*, 2005]. In three-dimensional simulations, $\mathbf{n}_t(\mathbf{x}_s)$ is the unit vector perpendicular to the fluid-fluid solid contact line in the plane of the solid-fluid interface. Simple contact angle models, like those illustrated in Figure 3, can be implemented by making the contact angle, θ , depend on the fluid velocity adjacent to the solid-fluid interface.

[130] There have been very few applications of continuum computational fluid dynamics with level set or volume of fluid interface tracking to multiphase fluid flow in fractured and porous media. Figure 16 shows a two-dimensional simulation of the injection of a liquid into an aperture with sinuous walls. In this simulation a liquid density of 1.0 g cm^{-3} , a surface tension of 22.8 dyn cm^{-1} , a gravitational acceleration of 980 cm s^{-2} , and a liquid viscosity of

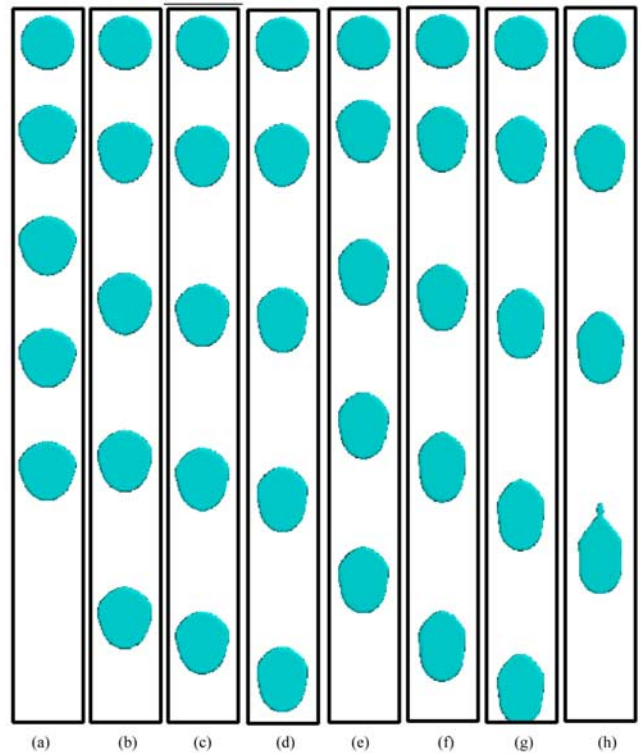


Figure 17. Consecutive snapshots of droplets sliding slowly in a vertical Hele-Shaw cell at various Bond numbers, Bo , and time lapses, Δt . (a) $Bo = 1.8$ and $\Delta t = 0.1 \text{ s}$, (b) $Bo = 1.9$ and $\Delta t = 0.1 \text{ s}$, (c) $Bo = 2.0$ and $\Delta t = 0.09 \text{ s}$, (d) $Bo = 2.1$ and $\Delta t = 0.08 \text{ s}$, (e) $Bo = 2.2$ and $\Delta t = 0.0625 \text{ s}$, (f) $Bo = 2.3$ and $\Delta t = 0.0625 \text{ s}$, (g) $Bo = 2.4$ and $\Delta t = 0.0436 \text{ s}$, and (h) $Bo = 2.5$ and $\Delta t = 0.0625 \text{ s}$ [Huang and Meakin, 2008].

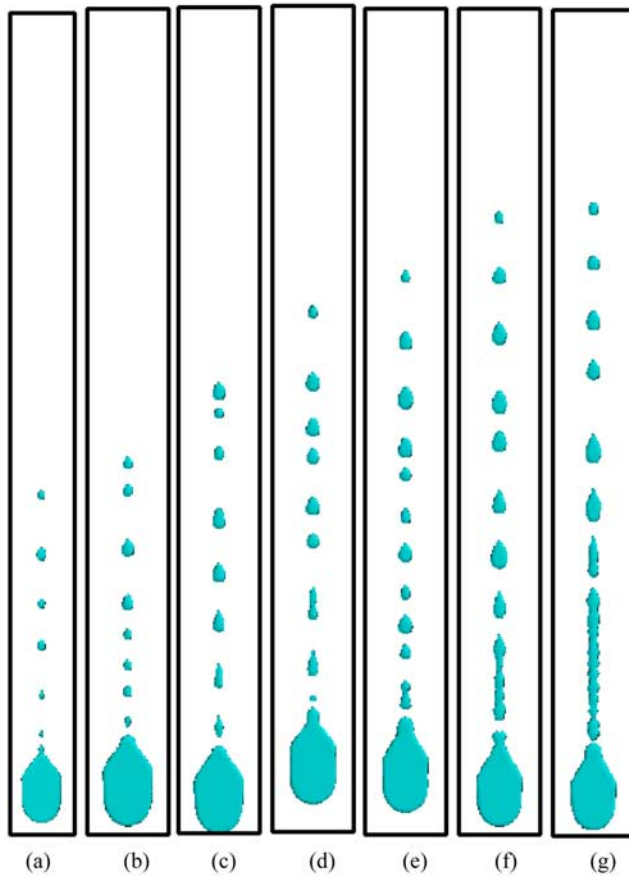


Figure 18. Simulated drop shapes and droplet patterns under high-speed sliding conditions: (a) $Bo = 2.51$, with a height 25% larger than others in Figure 18; (b) $Bo = 2.62$; (c) $Bo = 2.72$; (d) $Bo = 2.82$; (e) $Bo = 2.92$; (f) $Bo = 3.12$; and (g) $Bo = 3.22$ [Huang and Meakin, 2008].

$1.52 \times 10^{-1} \text{ g cm}^{-1} \text{ s}^{-1}$ were used. The contact angle model was based on an advancing contact angle of $\theta_a = 65^\circ$, a receding contact angle of $\theta_r = 35^\circ$, and a near-equilibrium of $\theta_{eq} = 35^\circ$ (see Figure 3c). Although the volume of fluid method is less elegant than the level set method, it has the important advantage of good mass conservation.

[131] Figures 17 and 18 show some results from a grid-based finite volume of fluid simulation of the Navier-Stokes equations for a liquid drop confined in a Hele-Shaw cell consisting of two smooth-walled vertical sheets separated by a small gap. Volume of fluid interface tracking was used in these simulations. A vertical Hele-Shaw cell can be regarded as a very simple model for a vertical fracture aperture. In the simulations, the Hele-Shaw cell aperture width, b , was set to 1 mm. At the start of a simulation, a cylindrical drop of liquid with a radius of $r = 1.5$ mm was inserted into the gap between the walls of the Hele-Shaw cell, with its axis perpendicular to the walls. The liquid-gas interfacial tension was $\Gamma = 20 \text{ dyn cm}^{-1}$; the fluid viscosities were $\mu_{\text{liquid}} = 1.50 \times 10^{-2} \text{ g cm}^{-1} \text{ s}^{-1}$ and $\mu_{\text{gas}} = 1.50 \times 10^{-4} \text{ g cm}^{-1} \text{ s}^{-1}$; the fluid densities were set to $\rho_{\text{liquid}} = 1.0 \text{ g cm}^{-3}$ and $\rho_{\text{gas}} = 1.0 \times 10^{-3} \text{ g cm}^{-3}$; and

the advancing, receding, and near-stationary contact angles were $\theta_a = 60^\circ$, $\theta_r = 5^\circ$, and $\theta_{eq} = 45^\circ$ (see Figure 3c). The changes in the shape of the drop as it slides in the gap between the cell walls, the changes in the asymptotic (long time) shape of the drop as the Bond number is increased, and the transition from sliding to sliding plus the shedding of a train of droplets is very similar to behavior observed in the experiments of Podgorski *et al.* [2001].

[132] Like lattice Boltzmann models for multiphase fluid flow, the phase field model is a diffuse interface model (the interface is spread out over a nonzero width, ξ_w). The success of diffuse interface methods depends on the width of the interface, which should be large enough to be resolved using the computational grid but small enough to satisfy the relationship $\xi_w \ll \{l_i\}$, where $\{l_i\}$ are the characteristic macroscopic length scales, including the system size.

[133] The phase field method for multiphase fluid dynamics [Jacqmin, 1999; Badalassi *et al.*, 2003] is based on the Ginzburg-Landau/Cahn-Hilliard equation (equations (9)–(12)), which is coupled with the Navier-Stokes equation. The diffusive transport of the composition or density variable can be expressed in the form $\mathbf{J} = -m\nabla\mu$, where μ is the chemical potential given by equation (16), \mathbf{J} is the flux density, and m is a mobility or Onsager transport coefficient, which may depend on the local phase field, $\phi(\mathbf{x})$. (More generally, $J_i = -L_{ij}\nabla\mu_j$ for a multicomponent system, where \mathbf{L} is the matrix of Onsager transport coefficients [Onsager, 1931a, 1931b].) Finally, the evolution of the composition field in a coordinate system moving with the fluid, $\phi(\mathbf{x})$, can be calculated from $\partial\phi(\mathbf{x})/\partial t = -\nabla \cdot \mathbf{J}$, which leads to the equation

$$\partial\phi(\mathbf{x})/\partial t = \nabla \cdot \{m\nabla[\partial F(\phi(\mathbf{x}))/\partial\phi(\mathbf{x}) - c\nabla^2(\phi(\mathbf{x}))]\} \quad (153)$$

for the evolution of the phase field $\phi(\mathbf{x})$. This equation is often referred to as the Cahn-Hilliard equation or conserved Ginzburg-Landau equation. In a stationary coordinate system

$$\partial\phi(\mathbf{x})/\partial t = -\mathbf{v} \cdot \nabla\phi(\mathbf{x}) + \nabla \cdot \{m\nabla[dF(\phi(\mathbf{x}))/d\phi(\mathbf{x}) - c\nabla^2(\phi(\mathbf{x}))]\}. \quad (154)$$

The flow of multiphase fluids can be based on equation (20) including the effect of the external potential on the free energy per unit volume, F . The phase field model is completed by incorporating the force acting on the fluid due to the free energy associated with the phase field into the Navier-Stokes momentum conservation equation (equation (4)) and adding appropriate boundary conditions. The modified, phase field/Navier-Stokes momentum conservation equation for a two-phase fluid is [Gurtin *et al.*, 1996]

$$\rho\partial\mathbf{v}/\partial t = -\mathbf{v} \cdot \nabla\rho\mathbf{v} - \nabla P + \eta\nabla \cdot \nabla\mathbf{v} + \mu\nabla\phi + \mathbf{f} \quad (155)$$

or

$$\rho\partial\mathbf{v}/\partial t = -\mathbf{v} \cdot \nabla\rho\mathbf{v} - \nabla P + \eta\nabla \cdot \nabla\mathbf{v} + \mu\nabla\phi + \phi\nabla V_{ex}, \quad (156)$$

where V_{ex} is the external potential acting on the phase field, and this equation is coupled with the advection diffusion equation (equation (154) for the phase field, ϕ). The modified momentum conservation equation [Jacqmin, 1999]

$$\rho \partial \mathbf{v} / \partial t = -\mathbf{v} \cdot \nabla \rho \mathbf{v} - \nabla S + \eta \nabla \cdot \nabla \mathbf{v} - \phi \nabla \mu + \mathbf{f}, \quad (157)$$

where $S = P - \phi \mu + F(\phi) - c/2(\nabla \phi \cdot \nabla \phi)$, has also been used. Equations (155) and (157) are equivalent if $F(\phi) - c/2(\nabla \phi \cdot \nabla \phi) = 0$, which is satisfied if the phase field is at equilibrium.

[134] The mobility parameter, m , in equations (153) and (154) is important to the accuracy of simulations carried out using the Navier-Stokes/Cahn-Hilliard approach. The phase field free energy functional generates Gibbs-Thompson and disjoining pressure effects, which increase as the mobility parameter, m , increases. On the other hand, the mobility parameter must be large enough to equilibrate the interface (reinitialize the phase field to make the potential uniform across the interface).

[135] In the limit in which the width of the diffuse interface approaches zero, the phase field model becomes identical to the corresponding sharp interface model. In practice, this theoretical limit cannot be closely approached, and the “center” of the diffuse interface approximately locates of the interface in the sharp interface limit. In some phase field models, the phase field ranges from -1 to $+1$, the free energy functional satisfies $F(\phi) = F(-\phi)$, and the $\phi = 0$ level set locates the interface in the sharp interface model. The relaxation of the phase field (equation (153) or (154)) serves a role that is similar to reinitialization of the signed distance function in the level set method. However, the level set method is based on a sharp interface paradigm, and this method attempts to exactly locate the sharp interface.

[136] The approach outlined above assumes a conserved order parameter, ϕ . If the order parameter is not conserved, the free energy functional is usually written in the form

$$\mathcal{F}[\phi(\mathbf{x})] = F[\phi(\mathbf{x})] + \varepsilon^2/2[\nabla \phi(\mathbf{x})]^2, \quad (158)$$

$$\mu(\mathbf{x}) = \delta \mathcal{F} / \delta \phi(\mathbf{x}) = dF[\phi(\mathbf{x})] / d\phi(\mathbf{x}) - \varepsilon^2 \nabla^2 [\phi(\mathbf{x})]. \quad (159)$$

For a nonconserved order parameter, the evolution of the order parameter is given by

$$d\phi(\mathbf{x}) / dt = -M \delta \mathcal{F} / \delta \phi(\mathbf{x}) = -M \{ dF[\phi(\mathbf{x})] / d\phi(\mathbf{x}) - \varepsilon^2 \nabla^2 [\phi(\mathbf{x})] \}, \quad (160)$$

which is often referred to as nonconserved Ginzburg-Landau equation or the Allen-Cahn equation.

[137] The conserved Ginzburg-Landau equation is appropriate for the conserved order parameters such as the concentration (composition) order parameter in spinodal decomposition (the separation of a mixture of two liquids into a liquid phase that is rich in one of the two components and a second phase that is rich in the other component). The nonconserved Ginzburg-Landau equation is appropriate for

nonconserved order parameters including the structural order parameters associated with phase transitions such as melting and magnetic phase transitions where $\int_{\Omega} \phi_n(\mathbf{x}) d\mathbf{x}$ is not conserved. Many processes involve both conserved and nonconserved order parameters. For example, in phase transitions both the structure and density change, and in this case the density order parameter is conserved but the structural order parameter is nonconserved. Irrespective of the dynamics, the width of the interface is controlled by the free energy functional. If the coefficient of the “ $(\nabla \phi)^2$ ” term is increased, the total free energy, $\int_{\Omega} F(\mathbf{x}) d\mathbf{x}$, will be minimized if the interface width is larger (equation (29)).

[138] To model multiphase fluid systems, the “real” free energy functional, $\mathcal{F}(\mathbf{x}) = F[\phi(\mathbf{x}), \nabla \phi(\mathbf{x}), \dots]$, where “ \dots ” indicates higher-order terms, could be used. However, the interface width in most multiphase fluid systems is on the order of a nanometer, and the free energy functional is often not accurately known. Phase field models with a physically realistic free energy functional, or a reasonably accurate approximation of the real free energy functional, are used to simulate the evolution of microstructure. Because of the small physical scale of these simulations, additional terms to represent the effects of thermal fluctuations may be needed. More commonly, if a uniform grid is used, a simplified free energy functional with an interface width on the order of a few grid elements is used. Under these conditions, the phase field model is being used to track the interface(s) (the evolution of the phase field allows the interface to be located, and there is no need for explicit interface tracking), and neither the width of the interface nor the shape of the order parameter profile across the interface have a physical interpretation. Adaptive mesh refinement allows the system size to be substantially increased while a small interface width is maintained, and if adaptive mesh refinement is used, then the width of the interface is on the order of a few times the width of the grid elements at the interface. However, it is not practical to refine the grid to molecular dimensions near the interface.

[139] In general, the fluid properties depend on the order parameter(s), and in most cases, simple relationships between properties such as the viscosity, the mobility, and the order parameter(s) are used [Badalassi et al., 2003; Jacqmin, 1999]. The functions used to describe the fluid properties are smooth functions of the order parameter(s), or phase field(s), that interpolate between the properties of the bulk fluid phases. The Cahn-Hilliard equation generates equilibrium solubilities and vapor pressures that depend on interfacial curvatures. Fluid flow will result in deformation of the fluid-fluid interfaces, including bending; contraction, which causes thickening, in some locations; and stretching, which causes thinning, in others. This will increase the free energy of the system, and the resulting free energy/chemical potential gradients drive flow and diffusion which tend to reduce the interface curvature and restore the interface width. No-slip boundary conditions can be implemented in the normal manner, and the wetting behavior can be controlled by fixing the chemical potential(s) at the solid boundaries.

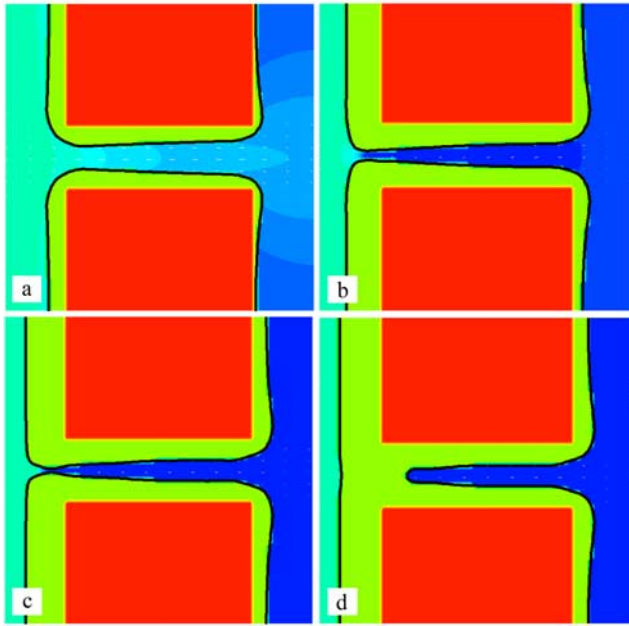


Figure 19. Two-dimensional simulation of precipitation in a pore using the level set method to capture the precipitate/solution interface. The precipitate (lime) grows on the solid (red) as supersaturated fluid is injected on the left-hand side. The simulation includes advection and diffusion of the solute coupled with precipitation on the solid (mineral) substrate or preexisting precipitate. The level set methods allows topological changes (closure of the pore) to be managed in a robust manner [Li *et al.*, 2008].

[140] A phase field method that is closely related to the level set method has been developed by cancelling the contribution to the potential generated by curvature (given by $\kappa = \nabla \cdot (\nabla \phi / |\nabla \phi|)$) of the phase field, which generates curvature-driven interface motion, and retaining the contributions that maintain the order parameter profile in the direction perpendicular to the interface [Folch *et al.*, 1999; Sun and Beckermann, 2006]. In the $w\kappa \rightarrow 0$ limit, this maintains a constant order parameter profile across the moving interface, and this method can be reformulated in terms of relaxation of the phase field toward a predetermined signed function of the distance from the sharp interface. If this approach is used the effects of surface tension can be reintroduced using a continuum interface model (equations (149) and (151)), and the surface tension becomes independent of the phase field, which is used solely for interface location. (A similar approach can be used to simulate precipitation and dissolution processes with phase field interface capturing [Xu and Meakin, 2008]. Following the methodology developed by Karma and Rappel [1998] for dendritic solidification from a melt, the Allen-Cahn equation (160) is coupled with the diffusion equation so that the coupled equations are equivalent to the corresponding sharp interface equations in the limit $\varepsilon \rightarrow 0$ (in the limit where the width of the diffuse interface approaches 0). The resulting equation for the evolution of

the phase field contains a term that eliminates the effects of the curvature-related free energy associated with the phase field (which tends to straighten curved interfaces). The coupling terms in the equations for the evolution of the concentration field and phase field ensure that the concentration field evolved with the appropriate solute source (dissolution) or sink (precipitation) in the diffuse interface and that the motion of the diffuse interface moves in response to the solute source or sink.)

[141] Velocity-dependent contact angles can be implemented via the nonequilibrium order parameter transport equation

$$\partial \phi / \partial t = -V \cdot \nabla \phi + \mathcal{D}_s [\alpha \partial \phi / \partial x_n + \nabla_s F_s(\phi)], \quad (161)$$

where \mathcal{D}_s is the surface diffusion coefficient and $F_s[\phi(\mathbf{x}_s)]$ is the surface free energy per unit area at position \mathbf{x}_s on the surface [Jacqmin, 1999]. An alternative approach is to control the wetting via the homogeneous free energy, $F[\phi(\mathbf{x})]$. For example, a homogeneous free energy with the form

$$F[\phi(\mathbf{x})] = \frac{1 + \alpha(\mathbf{x})}{2} \frac{(\phi^2 - 1)^2}{4} (\phi - 1) + \frac{1 - \alpha(\mathbf{x})}{2} \frac{K}{2} [\phi - A(\mathbf{x})]^2, \quad (162)$$

where $\alpha = 1$ in the fluid-occupied regions, $\alpha = -1$ in solid-occupied regions, and $A(\mathbf{x})$ can be varied to simulate spatially dependent wetting behavior, has been used to simulate complex wetting effects [Luo *et al.*, 2005].

[142] One of the advantages of the level set and phase field methods is that interfaces can be located with subgrid-scale accuracy (as opposed to the grid-scale accuracy of most lattice Boltzman models and the particle-scale accuracy of most SPH and DPD models). The phase field method has been used extensively to simulate the dynamics of solid-liquid boundaries including applications such as the dendritic growth of solid phases from melts [Karma and Rappel, 1998; Kobayashi, 1993; Chen, 2002] or from supersaturated solutions. In problems such as the growth of solid phases in a cooling melt, equations describing heat transport and the release of latent heat (energy conservation) must be included, and a temperature-dependent free energy functional is required. Phase field models have also been applied to a wide range of problems involving the evolution of morphology in materials science [Chen, 2002], condensed matter physics, and other areas. Some applications to geological processes, such as the development of a phase field model to simulate methane and carbon dioxide hydrates, have been reported [Svandal *et al.*, 2006]. However, potential applications far exceed actual applications at present.

[143] Figure 19 shows the results of a two-dimensional simulation of coupled fluid flow, solute transport, and precipitation, based on level set interface capturing. In this simulation, the rate of precipitation is assumed to be proportional to $C_s - C_{eq}$, where C_s is the solute concentration adjacent to the interface and C_{eq} is the solute

concentration in equilibrium with the interface (the Gibbs-Thompson effect was not included).

11. FUTURE TRENDS AND CHALLENGES

[144] On the pore scale the capillary pressure differences across fluid-fluid interfaces often play an important role in multiphase fluid flow, and these capillary pressure differences depend on the intrinsically complex contact line/contact angle dynamics, which, in turn, depends on physical and chemical heterogeneities and chemical impurities, particularly surfactants. In addition, flow through wetting films and vapor phase diffusion can be important. The models described above handle these complexities in different ways and with different levels of approximation. In principle, all of these difficulties can be overcome by molecular dynamics simulations with realistic interaction potentials and realistic models for or information about the structures of mineral surfaces on the atomic scale. In practice, of course, this is completely impossible because the time and length scales associated with the phenomena of interest are enormously larger than the scales that are accessible to molecular dynamics. If molecular dynamics is used as a “scale model” for pore-scale behavior, the contact line/wetting phenomenology may be correct, but the thickness of the precursor film relative to the pore size will be much too large (the MD simulation will be an imperfect scale model).

[145] Dissipative particle dynamics can be regarded as coarse-grained nonequilibrium molecular dynamics. It is on the order of 10^5 times faster than molecular dynamics, but this impressive increase in computational efficiency comes at the expense of loss of detail at the atomic/molecular scale. DPD models can be used to simulate all of the physical mechanisms associated with wetting behavior (slip at the solid-liquid interface, ordering in the fluid adjacent to the solid, evaporation/condensation and the formation of wetting films, etc.). In addition, DPD can also simulate the chemical phenomena (strong modification of interfacial energies, bending rigidity of fluid-fluid interfaces, equilibrium interface curvature, etc.) associated with surfactants. In practice, it is difficult to accurately relate the parameters used in a DPD simulation either to more fundamental molecular parameters or to continuum variables such as the fluid viscosity. More systematic and reliable ways of coarse graining molecular dynamics to construct DPD models would be an important advance.

[146] The lattice gas, lattice Boltzmann, and Monte Carlo models discussed in sections 5 and 6 take the coarse graining one step further. By this stage, essentially all molecular detail has been lost, but the reward is a very large increase in computational efficiency. If the *Shan and Chen* [1993, 1994] approach is used, the fluid-solid interactions are based on molecular interaction concepts, and the wetting behavior depends on these interactions. Alternatively, if the lattice Boltzmann model is based on a free energy functional approach, a surface term, $\int_S \phi h ds$, can be added to the free energy functional [Briant et al., 2004a, 2004b], where ϕ is the phase field and h is the “wetting

potential.” Slip at the solid-fluid boundary [Nie et al., 2004], evaporation/condensation (or molecular transport across liquid/liquid interfaces), and the general effects of surfactants [Nekovee et al., 2000] can still be simulated, but unlike MD and DPD, these models cannot be used to investigate how wetting behavior depends on surfactant size, shape, flexibility, etc., or the effects of atomic-scale heterogeneity. This class of models can be used to simulate the effects of larger-scale physical heterogeneity [Dupuis and Yeomans, 2005] and the effect of the capillary number on the contact angle [Raaijmakers et al., 2002].

[147] Although it is a macroscopic model, smoothed particle hydrodynamics is mathematically equivalent to molecular dynamics, and depending on spatial resolution, it can be interpreted as a molecular or mesoscale model [Hoover, 1998]. Consequently, SPH is capable of simulating all of the complex phenomenology associated with contact line and contact angle dynamics [Tartakovsky and Meakin, 2005a, 2005c, 2006]. However, the full range of scales (from the atomistic to the pore scale) cannot be investigated in a single simulation, and like the MD model, some dimensionless ratios, such as the ratio between the precursor film thickness and the pore size, will be different in SPH simulations and real systems. In the future this deficiency may be mitigated by simulations based on hybrid multiscale particle-based models.

[148] Pore network models and traditional computation fluid dynamics can provide no insight into the physics and chemistry of wetting phenomena. These models must be provided with a contact angle model, like those illustrated in Figure 3. They can be used to investigate the consequences of these models, but they have no other predictive capability. However, if the continuum model is based on a phase field approach, phenomena such as evaporation and condensation near the contact line occur automatically [Jacqmin, 2000].

[149] Despite considerable effort, we do not yet have reliable and accurate methods for simulating multiphase fluid flow under all conditions relevant to subsurface applications. Large density and viscosity contrasts are a challenge for some methods, and small, but nonzero, compressibilities are also a challenge. The soft interaction potentials (or equations of state with large compressibilities, which correspond to soft particle-particle interactions) used in particle methods lead to unrealistically large compressibilities, and this may result in significant errors in some applications such as poroelastic phenomena [Biot, 1941]. Compressibility effects can be reduced by hardening the interaction potentials, but this requires a shorter time step (more computing time or larger computing systems). This may be acceptable if computing speeds continue to increase (some computational science and engineering specialists are expecting that the speeds of the largest systems will increase by a factor of the order of 1000 during the next decade) and efficient particle codes that can efficiently utilize 100,000 or much more processing elements are developed. Particle methods have been developed for incompressible fluids, but they require solution of a pressure Poisson equation [Shao

and Lo, 2003; Koshizuka and Oka, 1996] at each step in the simulation.

[150] Within a few years, individual simulations that require $O(10^6)$ processor core hours will not be uncommon, and it will be possible to invest $O(10^8)$ processor core hours in high-priority investigations if code that scales well to a very large number of processor cores is available. This would make it possible to simulate multiphase fluid flow in complex three-dimensional pore spaces containing $O(10^4)$ pores using particle methods and larger systems using grid-based computational fluid dynamics. Using the same resources, it should be possible to use advanced lattice Boltzmann models (models that can simulate multiphase fluids with high viscosity and density contrasts) to simulate the propagation of fluid-fluid interfaces through porous media represented by voxel maps on $2048 \times 2048 \times 2048$ lattices (currently the cutting edge for X-ray tomography).

[151] The inability to simulate multiphase fluids with large density contrasts has been a serious limitation for lattice Boltzmann methods. New lattice Boltzmann methods that overcome this problem are beginning to emerge, but they have not yet been evaluated for subsurface applications. Lattice Boltzmann models that can be applied to systems with large compressibility ratios and/or large Schmidt numbers would also be an important advance.

[152] Faster algorithms will also play an important role. Historically, better algorithms have contributed more to effective calculation speed than hardware advances in many applications. The application of multiscale methods such as adaptive mesh refinement is now becoming de rigueur for large-scale continuum computational fluid dynamics applications, and adaptive mesh refinement is a key method for high-accuracy multiphase fluid dynamics simulations. However, the application of multiscale particle methods is still very much in its infancy [Scheibe *et al.*, 2007]. Adaptive particle refinement is also promising but little investigated. One approach, which has been applied to smoothed particle hydrodynamics simulations, is to associate individual support scale, h_i , and time steps, δt_i , with each particle. The support scale can be varied continuously to maintain a fixed number of particles within “interaction range,” and the time step can be varied continuously to maintain numerical stability [Hernquist, 1993; Alimi *et al.*, 2003]. If this approach is used, no attempt is made to synchronize the time steps. Instead, the time advances continuously, and particle i is moved when $t \geq t_i^{\text{last}} + \delta t_i$, where t_i^{last} is the time at which particle i last moved and t is the continuously increasing time. The SPH equation of motion must, of course, be modified to take into account the variable smoothing function support scales.

[153] Another approach is to add or remove particles according to some accuracy-related criterion [Lastiwka *et al.*, 2005]. After a particle has been added or removed, the smoothing lengths, h , in the vicinity of the added or removed particle are adjusted (this can be based on the idea that an essentially constant number of particles should be within interaction range of each particle), and particle masses are adjusted to conserve mass and, as well as

possible, the fluid density distribution before particle insertion or removal. This approach can also be thought of in terms of particle fission and coalescence [Kitsionas and Whitworth, 2002].

[154] Invariably, multiphase fluids in the Earth are in close contact with solids, and the complex behavior at the contact plays an important role in their behavior. In this case, several barriers must be overcome before simulations with accurate predictive value can be developed: (1) A better theoretical understanding of the behavior of fluids near to the contact line is needed, (2) accurate and effective ways must be found to couple hydrodynamics and contact line dynamics, and (3) better ways of characterizing and mathematically describing physical and chemical heterogeneities in complex subsurface systems are required. In principle, hybrid multiscale methods based on quantum and classical molecular dynamics could be used. However, at present, there is no clear path forward that would make this dream a reality.

[155] Simulation of mineral precipitation and dissolution on the pore and fracture aperture scale has not yet been very extensive in the geoscience community. In particular, most simulations have employed very simple models for dissolution and/or precipitation chemistry, and there has been little, if any, work on chemical processes coupled with multiphase fluid flow. We believe that this situation is likely to change rapidly. There is strong motivation for such simulations for both scientific discovery and practical applications.

[156] Because physical and chemical heterogeneity plays an important role on essentially all scales, it is not realistic to expect that computer simulations and experiments will give the same results when they are compared in detail. In the invasion percolation limit, for example (the very slow displacement of a wetting fluid by a nonwetting fluid), a small change in the pore space geometry can lead to a large change in the fluid-fluid interface, and the pore space geometry cannot be measured (or fabricated) with sufficient accuracy to support an accurate pore by pore prediction of how the fluid-fluid interface will propagate through the porous medium. Similarly, microscale roughness and trace impurities can also have a strong impact on the outcome of experiments at this detailed level. Consequently, experimentation validation of computer codes for multiphase fluid flow in fractured and/or porous media must be based primarily on the comparison of statistical measures such as correlation functions, saturations, etc. Computer code is subject to a variety of errors including discretization errors (grid and/or particle discretization as well as time discretization), convergence errors, truncation errors, geometry errors, and round-off errors. It is important to understand, control, and reduce these errors, but they cannot be completely eliminated. For many applications it is important to weigh the cost of reducing computational error against the errors and uncertainties associated with experiments and field characterization and the impact of computational uncertainties on the quality of understanding derived from them. Better numerical methods should reduce computa-

tional errors or allow larger-scale simulations to be carried out with acceptable errors.

[157] In most simulations of pore-scale multiphase fluid flow and reactive transport the pore (or fracture) geometry is assumed to be constant, apart from the effects of precipitation and dissolution. However, in many important geosystems the confining geometry changes slowly as a result of processes such as pressure solution [Tada and Siever, 1989] or rapidly because of fracturing and changes in pore pressure or matrix stress. It is important to include the coupling between fluid flow and geomechanical processes for a number of important applications including oil recovery and carbon dioxide sequestration.

[158] Micro-organisms are important in a variety of subsurface geosystems, and they can have an important impact on fluid flow, mineral dissolution, and particle formation. Biofilm may form under nutrient-rich conditions, often resulting from the artificial introduction of nutrients for geotechnical applications such as the decomposition of toxic organic contaminants or the accidental introduction of contaminants that are nutrients. Biofilm often has a strong impact on fluid flow, and the interactions between deformable biofilm and fluid flow may have important consequences. Particle methods such as dissipative particle dynamics are well suited to the simulation of polymeric and colloidal systems, including biopolymers and biocolloids, and soft condensed matter such as biofilm. It is well known that some micro-organisms secrete ligands such as siderophores that can rapidly dissolve minerals and that some micro-organisms mediate the formation of mineral colloids and nanoparticles. Some micro-organisms also produce surfactants that can have an important impact on wetting behavior and surface tension. The accurate simulation of multiphase fluid flow and reactive transport in biologically active systems will be challenging because of their inherent complexity.

[159] **ACKNOWLEDGMENTS.** We would like to thank Peter Coveney (Figure 7), Scott Fogler (Figure 4), Qunjun Kang (Figure 6), Hai Huang (Figures 16–18), Xiaoyi Li (Figure 19), Peter Lichtner (Figure 6), Alex Prevost (Figure 2), and Mark Robbins (Figure 9) for permission to reproduce figures from their publications. Hai Huang, Xiaoyi Li, Robert Nourgaliev, Bruce Palmer, and Zhijie Xu made valuable suggestions that substantially improved the manuscript. This research was supported by the Office of Science of the U.S. Department of Energy under the Scientific Discovery through Advanced Computing program. The Pacific Northwest National Laboratory is operated for the U.S. Department of Energy by Battelle under contract DE-AC06-76RL01830, and the Idaho National Laboratory is operated for the U.S. Department of Energy by the Battelle Energy Alliance under contract DE-AC07-05ID14517.

[160] The Editor responsible for this paper was Daniel Tartakovsky. He thanks two anonymous technical reviewers.

REFERENCES

- Adalsteinsson, D., and J. A. Sethian (1999), The fast construction of extension velocities in level set methods, *J. Comput. Phys.*, **148**, 2–22, doi:10.1006/jcph.1998.6090.
- Aker, E., K. J. Maloy, A. Hansen, and G. G. Batrouni (1998), A two-dimensional network simulator for two phase flow in porous media, *Transp. Porous Media*, **32**, 163–186, doi:10.1023/A:1006510106194.
- Alder, B. J., and T. E. Wainright (1962), Phase transition in elastic disks, *Phys. Rev.*, **127**, 359–361, doi:10.1103/PhysRev.127.359.
- Alexander, F. J., H. Chen, S. Chen, and G. D. Doolen (1992), Lattice Boltzmann model for compressible fluids, *Phys. Rev. A*, **46**, 1967–1970, doi:10.1103/PhysRevA.46.1967.
- Alexander, F. J., A. L. Garcia, and B. J. Alder (1995), A consistent Boltzmann algorithm, *Phys. Rev. Lett.*, **74**, 5212–5215, doi:10.1103/PhysRevLett.74.5212.
- Alexander, F. J., A. L. Garcia, and B. J. Alder (1998), Cell size dependence of transport coefficients in stochastic particle algorithms, *Phys. Fluids*, **10**, 1540–1542, doi:10.1063/1.869674.
- Al-Gharbi, M. S., and M. Blunt (2005), Dynamic network modeling of two-phase drainage in porous media, *Phys. Rev. E*, **71**, 016308, doi:10.1103/PhysRevE.71.016308.
- Alimi, J.-M., A. Serna, C. Pastor, and G. Bernabeu (2003), Smooth particle hydrodynamics: Importance of correction terms in adaptive resolution algorithms, *J. Comput. Phys.*, **192**, 157–174, doi:10.1016/S0021-9991(03)00351-6.
- Allahyarov, E., and G. Gompper (2002), Mesoscopic solvent simulations: Multiparticle-collision dynamics of three-dimensional flows, *Phys. Rev. E*, **66**, 036702, doi:10.1103/PhysRevE.66.036702.
- Allen, M. P., and D. J. Tildesley (1987), *Computer Simulation of Liquids*, Oxford Sci., Oxford, U. K.
- Anderson, J. D. (1995), *Computational Fluid Dynamics*, McGraw Hill, New York.
- Ausserre, D., A. M. Picard, and L. Leger (1986), Existence and role of the precursor film in the spreading of polymer liquids, *Phys. Rev. Lett.*, **57**, 2671–2674, doi:10.1103/PhysRevLett.57.2671.
- Badalassi, V. E., H. D. Cenciros, and S. Banerjee (2003), Computation of multiphase systems with phase field models, *J. Comput. Phys.*, **190**, 371–397, doi:10.1016/S0021-9991(03)00280-8.
- Bakke, S., and P. E. Oren (1997), 3D pore scale modeling of sandstone and flow simulations in the pore network, *SPE J.*, **2**, 136–149, doi:10.2118/35479-PA.
- Barabasi, A.-L., and H. E. Stanley (1995), *Fractal Concepts in Surface Growth*, Cambridge Univ. Press, Cambridge, U. K.
- Barrat, J.-L., and L. Bocquet (1999), Large slip effect at a non-wetting fluid-solid interface, *Phys. Rev. Lett.*, **82**, 4671–4674, doi:10.1103/PhysRevLett.82.4671.
- Beaglehole, D. (1989), Profiles of the precursor of spreading drops of siloxane oil on glass, fused silica and mica, *J. Phys. Chem.*, **93**, 893–899, doi:10.1021/j100339a067.
- Bestehorn, M., and K. Neuffer (2001), Surface patterns of laterally extended thin films in three dimensions, *Phys. Rev. Lett.*, **87**, 046101, doi:10.1103/PhysRevLett.87.046101.
- Bear, J. (1972), *Dynamics of Fluids in Porous Media*, Elsevier, New York.
- Bhatnagar, P. L., E. P. Gross, and M. Krook (1954), A model for collision processes in gasses. 1. Small amplitude processes in charged and neutral one-component systems, *Phys. Rev.*, **94**, 511–525, doi:10.1103/PhysRev.94.511.
- Bhattacharya, S., and M. J. Higgins (1993), Dynamics of a disordered flux line lattice, *Phys. Rev. Lett.*, **70**, 2617–2620, doi:10.1103/PhysRevLett.70.2617.
- Biot, M. A. (1941), General theory of three dimensional consolidation, *J. Appl. Phys.*, **12**, 155–164, doi:10.1063/1.1712886.
- Bird, G. A. (1963), Approach to translational equilibrium in a rigid sphere gas, *Phys. Fluids*, **6**, 1518–1519, doi:10.1063/1.1710976.
- Bird, G. A. (1994), *Molecular Gas Dynamics and the Direct Simulation of Gas Flows*, Clarendon, Oxford, U. K.

- Blunt, M., and P. King (1990), Macroscopic parameters from simulation of pore scale flow, *Phys. Rev. A*, **42**, 4780–4787, doi:10.1103/PhysRevA.42.4780.
- Blunt, M. J., M. Jackson, M. Piri, and P. H. Valvante (2002), Detailed physics, predictive capabilities and macroscopic consequences for pore network models of multiphase flow, *Adv. Water Resour.*, **25**, 1069–1089, doi:10.1016/S0309-1708(02)00049-0.
- Bouzidi, M., M. Firdaouss, and P. Lallemand (2001), Momentum transfer of a Boltzmann-lattice fluid with boundaries, *Phys. Fluids*, **13**, 3452–3459, doi:10.1063/1.1399290.
- Brackbill, J., D. B. Kothe, and C. Zemach (1992), A continuum method for modeling surface tension, *J. Comput. Phys.*, **100**, 335–354, doi:10.1016/0021-9991(92)90240-Y.
- Briant, A. J., P. Papatzacos, and J. M. Yeomans (2001), Lattice Boltzmann simulations of contact line motion in a liquid-gas system, *Philos. Trans. R. Soc. London, Ser. A*, **360**, 485–495.
- Briant, A. J., A. J. Wagner, and J. M. Yeomans (2004a), Lattice Boltzmann simulations of contact line motion. I. Liquid-gas systems, *Phys. Rev. E*, **69**, 031602, doi:10.1103/PhysRevE.69.031602.
- Briant, A. J., A. J. Wagner, and J. M. Yeomans (2004b), Lattice Boltzmann simulations of contact line motion II. Binary fluids, *Phys. Rev. E*, **69**, 031603, doi:10.1103/PhysRevE.69.031603.
- Bryant, S., and M. J. Blunt (1992), Prediction of relative permeability in simple porous media, *Phys. Rev. A*, **46**, 2004–2011, doi:10.1103/PhysRevA.46.2004.
- Buick, J. M., and J. A. Cosgrove (2006), Investigation of a lattice Boltzmann model with a variable speed of sound, *J. Phys. A Math. Gen.*, **39**, 13,807–13,815, doi:10.1088/0305-4470/39/44/013.
- Buick, J. M., and C. A. Greated (2000), Gravity in a lattice Boltzmann model, *Phys. Rev. E*, **61**, 5307–5320, doi:10.1103/PhysRevE.61.5307.
- Buldyrev, S. V., A.-L. Barabasi, F. Caserta, S. Havlin, H. E. Stanley, and T. Viscek (1992), Anomalous interface roughening in porous media: Experiment and model, *Phys. Rev. A*, **45**, R8313–R8316, doi:10.1103/PhysRevA.45.R8313.
- Cahn, J. W., and J. E. Hilliard (1958), Free energy of a nonuniform system. I. Interfacial free energy, *J. Chem. Phys.*, **28**, 258–267, doi:10.1063/1.1744102.
- Chen, H.-Y., D. Jasnow, and J. Vinals (2000), Interface and contact line motion in a two phase fluid under shear flow, *Phys. Rev. Lett.*, **85**, 1686–1689, doi:10.1103/PhysRevLett.85.1686.
- Chen, L.-Q. (2002), Phase-field models for microstructure evolution, *Annu. Rev. Mater. Res.*, **32**, 113–140, doi:10.1146/annurev.matsci.32.112001.132041.
- Christenson, H. K. (1983), Experimental measurements of solvation forces in nonpolar liquids, *J. Chem. Phys.*, **78**, 6906–6913, doi:10.1063/1.444639.
- Colagrossi, A., and M. Landrini (2003), Numerical simulation of interfacial flows by smoothed particle hydrodynamics, *J. Comput. Phys.*, **191**, 448–475, doi:10.1016/S0021-9991(03)00324-3.
- Conti, M. (2001), Density change effects on crystal growth from the melt, *Phys. Rev. E*, **64**, 051601, doi:10.1103/PhysRevE.64.051601.
- Coveney, P. V., and P. Espanol (1995), Dissipative particle dynamics for interacting multicomponent systems, *J. Phys. A Math. Gen.*, **30**, 779–784.
- Csahok, Z., H. Honda, and T. Viscek (1993a), Dynamics of surface roughening in disordered media, *J. Phys. A Math. Gen.*, **26**, L171–L178, doi:10.1088/0305-4470/26/5/001.
- Csahok, Z., H. Honda, E. Somfai, and T. Viscek (1993b), Dynamics of surface roughening in disordered media, *Physica A*, **200**, 136–154, doi:10.1016/0378-4371(93)90512-3.
- Cubaud, T., and M. Fermigier (2004), Advancing contact lines on chemically patterned surfaces, *J. Colloid Interface Sci.*, **269**, 171–177, doi:10.1016/j.jcis.2003.08.008.
- Davis, H. T., and L. E. Scriven (1982), Stress and structure in liquid interfaces, *Adv. Chem. Phys.*, **49**, 357–454, doi:10.1002/9780470142691.ch6.
- de Gennes, P. G. (1985), Wetting: Statics and dynamics, *Rev. Mod. Phys.*, **57**, 827–863, doi:10.1103/RevModPhys.57.827.
- D’Humières, D., P. Lallemand, and U. Frisch (1986), Lattice gas models for 3D hydrodynamics, *Europhys. Lett.*, **2**, 291–297, doi:10.1209/0295-5075/2/4/006.
- de Johnge, V., D. Chatain, I. Riviollet, and N. Eustathopoulos (1990), Contact-angle hysteresis due to roughness in 4 metal sapphire systems, *J. Chim. Phys. Phys. Chim. Biol.*, **87**, 1623–1645.
- Delker, T., D. B. Pengra, and P.-Z. Wong (1996), Interface pinning and the dynamics of capillary rise in a porous medium, *Phys. Rev. Lett.*, **76**, 2902–2905, doi:10.1103/PhysRevLett.76.2902.
- Dragila, M. I., and S. W. Wheatcraft (2001), Free surface films, in *Conceptual Models of Flow and Transport in the Fractured Vadose Zone*, chap. 7, pp. 217–241, Natl. Acad. Press, Washington, D. C.
- Dupuis, A., and J. M. Yeomans (2005), Droplet dynamics on patterned substrates, *Pramana*, **64**, 1019–1027.
- Dussan V., E. B. (1979), On the spreading of liquids on solid surfaces: Static and dynamic contact lines, *Annu. Rev. Fluid Dyn.*, **11**, 371–400, doi:10.1146/annurev.fl.11.010179.002103.
- Dzwinel, W., and D. A. Yuen (2000), Matching macroscopic properties of binary fluids to the interactions of dissipative particle dynamics, *Int. J. Mod. Phys. C*, **11**, 1–25, doi:10.1142/S012918310000002X.
- Eden, M. (1961), A two-dimensional growth process, in *Proceedings of the 4th Berkeley Symposium on Mathematics, Statistics and Probability*, vol. IV, pp. 223–239, Univ. of Calif. Press, Berkeley.
- Edwards, S. F., and D. R. Wilkinson (1982), The surface statistics of granular aggregates, *Proc. R. Soc. London, Ser. A*, **381**, 17–31, doi:10.1098/rspa.1982.0056.
- Eggers, J., and H. A. Stone (2004), Characteristic lengths at moving contact lines for a perfectly wetting fluid: The influence of seed on the dynamic contact angle, *J. Fluid Mech.*, **505**, 309–321, doi:10.1017/S0022112004008663.
- Elliott, G. E. P., and A. C. Riddiford (1962), Dynamic contact lines and rates of adsorption, *Nature*, **195**, 795–796, doi:10.1038/195795a0.
- Enright, D., R. Fedkiw, J. Ferziger, and I. Mitchell (2002), A hybrid particle level set method for improved interface capturing, *J. Comput. Phys.*, **183**, 83–116, doi:10.1006/jcph.2002.7166.
- Espanol, P. (1998), Fluid particle model, *Phys. Rev. E*, **57**, 2930–2948, doi:10.1103/PhysRevE.57.2930.
- Espanol, P., and P. Warren (1995), Statistical dynamics of dissipative particle dynamics, *Europhys. Lett.*, **30**, 191–196, doi:10.1209/0295-5075/30/4/001.
- Fan, L., H. Fang, and Z. Lin (2001), Simulation of contact line dynamics in a two-dimensional capillary tube by the lattice Boltzmann model, *Phys. Rev. E*, **63**, 051603, doi:10.1103/PhysRevE.63.051603.
- Fatt, I. (1956a), The network model of porous media I. Capillary pressure characteristics, *Trans. Am. Inst. Min. Metall. Pet. Eng.*, **207**, 144–159.
- Fatt, I. (1956b), The network model of porous media II. Dynamic properties of a single size tube network, *Trans. Am. Inst. Min. Metall. Pet. Eng.*, **207**, 160–163.
- Fatt, I. (1956c), The network model of porous media III. Dynamic properties of networks with tune network distributions, *Trans. Am. Inst. Min. Metall. Pet. Eng.*, **207**, 164–181.
- Fenwick, D. H., and M. J. Blunt (1998), Three-dimensional modeling of three-phase imbibition and drainage, *Adv. Water Resour.*, **21**, 121–143, doi:10.1016/S0309-1708(96)00037-1.
- Ferer, M., G. S. Bromhal, and D. H. Smith (2003), Pore-level modeling of immiscible drainage: Validation in the invasion percolation and DLA limits, *Physica A*, **319**, 11–23, doi:10.1016/S0378-4371(02)01508-X.
- Flekkoy, E. G., U. Oxaal, J. Feder, and T. Jossang (1995), Hydrodynamic dispersion at stagnation points—Simulations and experi-

- ments, *Phys. Rev. E*, **52**, 4952–4962, doi:10.1103/PhysRevE.52.4952.
- Flekkoy, E. G., G. Wagner, and J. Feder (2000), Hybrid model for combined particle and continuum dynamics, *Europhys. Lett.*, **52**, 271–276, doi:10.1209/epl/i2000-00434-8.
- Folch, R., J. Casademunt, A. Hernandez-Machado, and L. Menendez-Piscina (1999), Phase field model for Hele-Shaw cells with arbitrary viscosity contrast. I. Theoretical approach, *Phys. Rev. E*, **60**, 1724–1733, doi:10.1103/PhysRevE.60.1724.
- Freund, J. B. (2003), The atomic detail of a wetting/de-wetting flow, *Phys. Fluids*, **15**, L33–L36, doi:10.1063/1.1565112.
- Frisch, U., B. Hasslacher, and Y. Pomeau (1986), Lattice-gas automata for the Navier-Stokes equation, *Phys. Rev. Lett.*, **56**, 1505–1508, doi:10.1103/PhysRevLett.56.1505.
- Gao, D., N. B. Morley, and V. Dhir (2003), Numerical simulation of wavy falling film flow using VOF method, *J. Comput. Phys.*, **192**, 624–642, doi:10.1016/j.jcp.2003.07.013.
- Gingold, R. A., and J. J. Monaghan (1977), Smoothed particle hydrodynamics: Theory and application to non spherical stars, *Mon. Not. R. Astron. Soc.*, **181**, 375–389.
- Ginzburg, V. L., and L. D. Landau (1950), On the theory of superconductivity (in Russian), *Zh. Eksp. Teor. Fiz.*, **20**, 1064–1082. (English translation, in *L.D. Landau*, edited by D. ter Haar, pp. 138–167, Pergamon, Oxford, U. K., 1965.)
- Glass, R. J., M. J. Nicholl, and L. Yarrington (1998), A modified invasion percolation model for low-capillary number immiscible displacements in horizontal rough-walled fractures: Influence of local in-plane curvature, *Water Resour. Res.*, **34**, 3215–3234, doi:10.1029/98WR02224.
- Glimm, J., J. W. Grove, X.-L. Li, and N. Zhao (1999), Simple front tracking, in *Contemporary Mathematics*, vol. 238, edited by G.-Q. Chen and E. DiBenedetto, pp. 133–149, Am. Math. Soc., Providence, R. I.
- Gonzalez-Segredo, N., M. Nekovee, and P. V. Coveney (2003), Three-dimensional lattice-Boltzmann simulations of critical spinodal decomposition in binary immiscible fluids, *Phys. Rev. E*, **67**, 046304, doi:10.1103/PhysRevE.67.046304.
- Gunstensen, A. K., D. H. Rothman, S. Zaleski, and G. Zanetti (1991), Lattice Boltzmann model of immiscible fluids, *Phys. Rev. A*, **43**, 4320–4327, doi:10.1103/PhysRevA.43.4320.
- Guo, H., K. Kremer, and T. Sodderrmann (2002), Nonequilibrium molecular dynamics simulation of shear alignment in amphiphilic model systems, *Phys. Rev. E*, **66**, 061503, doi:10.1103/PhysRevE.66.061503.
- Gurtin, M. E., D. Polignone, and J. Vinals (1996), Two phase binary fluids and immiscible fluids described by an order parameter, *Math. Models Methods Appl. Sci.*, **6**, 815–831, doi:10.1142/S0218202596000341.
- Hadjiconstantinou, N. (1999), Hybrid atomistic-continuum formulations and the moving contact line problem, *J. Comput. Phys.*, **154**, 245–265, doi:10.1006/jcph.1999.6302.
- Haines, W. B. (1930), Studies in the physical properties of soil the hysteresis effect in capillary properties and the modes of moisture distribution associated therewith, *J. Agric. Sci.*, **20**, 97–116.
- Hamaker, H. C. (1937), London van der Waals interaction between spherical particles, *Physica*, **4**, 1058–1072.
- Hardy, W. P. (1919), The spreading of fluids on glass, *Philos. Mag.*, **38**, 49–55.
- Harting, J., J. Chin, M. Venturoli, and P. V. Coveney (2005), Large scale lattice Boltzmann simulations of complex fluids: Advanced through the advent of computational grids, *Philos. Trans. R. Soc.*, **363**, 1895–1915.
- Hashimoto, Y., Y. Chen, and H. Ohashi (2000), Immiscible real-coded lattice gas, *Comput. Phys. Commun.*, **129**, 56–62, doi:10.1016/S0010-4655(00)00092-8.
- He, X., and L.-S. Luo (1997), Theory of the lattice Boltzmann method: From the Boltzmann equation to the lattice Boltzmann equation, *Phys. Rev. E*, **56**, 6811–6817, doi:10.1103/PhysRevE.56.6811.
- Hellerqvist, M. C., D. Ephron, W. R. White, M. R. Beasley, and A. Kapitulnik (1996), Vortex dynamics in two-dimensional amorphous Mo₇₇ Ge₂₃ films, *Phys. Rev. Lett.*, **76**, 4022–4025, doi:10.1103/PhysRevLett.76.4022.
- Hernquist, L. (1993), Some Cautionary remarks about smoothed particle hydrodynamics, *Astrophys. J.*, **404**, 717–722, doi:10.1086/172325.
- Higgins, M. J., A. A. Middleton, and S. Bhattacharya (1993), Scaling near mode locking in a charge density wave conductor, *Phys. Rev. Lett.*, **70**, 3784–3787, doi:10.1103/PhysRevLett.70.3784.
- Higuera, F. J., and J. Jimenez (1989), Boltzmann approach to lattice gas simulations, *Europhys. Lett.*, **9**, 663–668, doi:10.1209/0295-5075/9/7/009.
- Hirschfelder, J. O., C. F. Curtiss, and R. B. Bird (1964), *Molecular Theory of Gases and Liquids*, John Wiley, New York.
- Hirshfeld, D., and D. C. Rapaport (1998), Molecular dynamics simulation of Taylor-Couette vortex formation, *Phys. Rev. Lett.*, **80**, 5337–5340, doi:10.1103/PhysRevLett.80.5337.
- Holt, R. M., E. Fjoer, O. Torsoeter, and S. Bakke (1996), Petrophysical laboratory measurements for basin and reservoir evaluation, *Mar. Pet. Geol.*, **13**, 383–391, doi:10.1016/0264-8172(95)00091-7.
- Hoogerbrugge, P. J., and K. M. V. A. Koelman (1992), Simulating microscopic hydrodynamic phenomena with dissipative particle dynamics, *Europhys. Lett.*, **19**, 155–160, doi:10.1209/0295-5075/19/3/001.
- Hoover, W. G. (1998), Isomorphism linking smooth particles and embedded atoms, *Physica A*, **260**, 244–254, doi:10.1016/S0378-4371(98)00357-4.
- Horvath, V. K., and H. E. Stanley (1995), Temporal scaling of interfaces propagating in porous media, *Phys. Rev. E*, **52**, 5166–5169, doi:10.1103/PhysRevE.52.5166.
- Huang, H., and P. Meakin (2008), Three-dimensional simulation of liquid drop dynamics within unsaturated vertical Hele-Shaw cells, *Water Resour. Res.*, **44**, W03411, doi:10.1029/2007WR006158.
- Huang, H., P. Meakin, and M. Liu (2005), Computer simulation of two-phase immiscible fluid motion in unsaturated complex fractures using a volume of fluid method, *Water Resour. Res.*, **41**, W12413, doi:10.1029/2005WR004204.
- Ihle, T., and D. M. Kroll (2001), Stochastic rotation dynamics: A Galilean-invariant mesoscopic model for fluid flow, *Phys. Rev. E*, **63**, 020201, doi:10.1103/PhysRevE.63.020201.
- Inoue, Y., Y. Chen, and H. Ohashi (2004), A mesoscopic simulation model for immiscible multiphase fluids, *J. Comput. Phys.*, **201**, 191–203, doi:10.1016/j.jcp.2004.05.008.
- Jacqmin, D. (1999), Calculation of two-phase Navier-Stokes flows using phase-field modeling, *J. Comput. Phys.*, **155**, 96–127, doi:10.1006/jcph.1999.6332.
- Jacqmin, D. (2000), Contact line dynamics of a diffuse fluid interface, *J. Fluid Mech.*, **402**, 57–88, doi:10.1017/S0022112099006874.
- Jamtveit, B., H. Austrheim, and A. Malthe-Sorensen (2000), Accelerated hydration of the Earth's deep crust induced by stress perturbations, *Nature*, **408**, 75–78, doi:10.1038/35040537.
- Jensen, I. (1996), Low-density series expansions for directed percolation on square and triangular lattices, *J. Phys. A Math. Gen.*, **29**, 7013–7040, doi:10.1088/0305-4470/29/22/007.
- Kang, Q., D. Zhang, P. C. Lichtner, and I. N. Tsimpanogiannis (2004), Lattice Boltzmann model for growth from supersaturated solution, *Geophys. Res. Lett.*, **31**, L21604, doi:10.1029/2004GL021107.
- Kang, Q., I. N. Tsimpanogiannis, D. Zhang, and P. C. Lichtner (2005), Numerical modeling of pore scale phenomena during CO₂ sequestration in oceanic sediments, *Fuel Process. Technol.*, **86**, 1647–1665, doi:10.1016/j.fuproc.2005.02.001.
- Kang, Q., P. C. Lichtner, and D. Zhang (2006), Lattice Boltzmann pore-scale model for multicomponent reactive transport in por-

- ous media, *J. Geophys. Res.*, *111*, B05203, doi:10.1029/2005JB003951.
- Kang, Q., P. C. Lichtner, and D. Zhang (2007), An improved lattice Boltzmann model for multicomponent reactive transport in porous media at the pore scale, *Water Resour. Res.*, *43*, W12S14, doi:10.1029/2006WR005551.
- Kang, W., and U. Landman (2007), Universality crossover of the pinch-off shape profiles of collapsing liquid nanobridges in vacuum and vapor environments, *Phys. Rev. Lett.*, *98*, 064504, doi:10.1103/PhysRevLett.98.064504.
- Kardar, M., G. Parisi, and Y.-C. Zhang (1986), Dynamic scaling of growing interfaces, *Phys. Rev. Lett.*, *56*, 889–892, doi:10.1103/PhysRevLett.56.889.
- Karma, A., and W.-J. Rappel (1998), Quantitative phase-field modeling of dendritic growth in two and three dimensions, *Phys. Rev. E*, *57*, 4323–4349, doi:10.1103/PhysRevE.57.4323.
- Kessler, D. A., H. Levine, and Y. Tu (1991), Interface fluctuations in random media, *Phys. Rev. A*, *43*, 4551–4554, doi:10.1103/PhysRevA.43.4551.
- Kirchoff, G. R. (1845), Ueber den durchgang eines elektrischen stromes durch eine ebene, insbesonere durch eine kreisförmige (About the electric current running through a plane, especially through a circular form), *Ann. Phys. Chem.*, *64*, 487–514.
- Kirkwood, J. G. (1939), Molecular distribution in liquids, *J. Chem. Phys.*, *7*, 919–925, doi:10.1063/1.1750344.
- Kitsionas, S., and A. P. Whitworth (2002), Smoothed particle hydrodynamics with particle splitting, applied to self-gravitating collapse, *Mon. Not. R. Astron. Soc.*, *330*, 129–136, doi:10.1046/j.1365-8711.2002.05115.x.
- Kobayashi, R. (1993), Modeling and simulation of dendritic crystal growth, *Physica D*, *63*, 410–423, doi:10.1016/0167-2789(93)90120-P.
- Kong, B., and X. Yang (2006), Dissipative particle dynamics simulation of contact angle hysteresis on a patterned solid/air composite surface, *Langmuir*, *22*, 2065–2073, doi:10.1021/la051983m.
- Koplik, J., and H. Levine (1985), Interface moving through a random background, *Phys. Rev. B*, *32*, 280–292, doi:10.1103/PhysRevB.32.280.
- Koplik, J., J. R. Banavar, and J. F. Willemsen (1988), Molecular dynamics of Poiseuille flow and moving contact lines, *Phys. Rev. Lett.*, *60*, 1282–1285, doi:10.1103/PhysRevLett.60.1282.
- Koshizuka, S., and Y. Oka (1996), Moving particle semi implicit method for fragmentation of incompressible fluid, *Nucl. Sci. Eng.*, *123*, 421–434.
- Kubo, R. (1966), The fluctuation-dissipation theorem, *Rep. Prog. Phys.*, *29*, 255–282, doi:10.1088/0034-4885/29/1/306.
- Lamura, A., G. Gomper, T. Ihle, and D. M. Kroll (2001), Multi-particle collision dynamics: Flow around a circular and a square cylinder, *Europhys. Lett.*, *56*, 319–325.
- Lastiwka, M., N. Quinlan, and M. Basa (2005), Adaptive particle distribution for smoothed particle hydrodynamics, *Int. J. Numer. Methods Fluids*, *47*, 1403–1409, doi:10.1002/fld.891.
- Lee, T., and C.-L. Lin (2005), A stable discretization of the lattice Boltzmann equation for simulation of incompressible two-phase flows at high density ratio, *J. Comput. Phys.*, *206*, 16–47, doi:10.1016/j.jcp.2004.12.001.
- Lenormand, R., C. Zacone, and A. Sarr (1983), Mechanisms of the displacement of one fluid by another in a network of capillary ducts, *J. Fluid Mech.*, *135*, 337–353, doi:10.1017/S0022112083003110.
- Li, X., H. Huang, and P. Meakin (2008), Level set simulation of coupled advection-diffusion and pore structure evolution due to mineral precipitation in porous media, *Water Resour. Res.*, *44*, W12407, doi:10.1029/2007WR006742.
- Liebermann, L. N. (1949), The second viscosity of liquids, *Phys. Rev.*, *75*, 1415–1422, doi:10.1103/PhysRev.75.1415.
- Lifshitz, E. M. (1956), The theory of molecular attractive forces between solids, *Sov. Phys. JETP, Engl. Transl.*, *2*, 73–83.
- Lin, C., and M. H. Cohen (1982), Quantitative methods of micro-geometric modeling, *J. Appl. Phys.*, *53*, 4152–4162, doi:10.1063/1.331238.
- Liu, M., P. Meakin, and H. Huang (2007), Dissipative particle dynamics simulation of fluid motion through an unsaturated fracture and fracture junction, *J. Comput. Phys.*, *222*, 110–130, doi:10.1016/j.jcp.2006.07.017.
- Lowe, C. P. (1999), An alternative approach to dissipative particle dynamics, *Europhys. Lett.*, *47*, 145–151, doi:10.1209/epl/i1999-00365-x.
- Lowry, M. I., and C. T. Miller (1995), Pore-scale modeling of nonwetting-phase residual saturation in porous media, *Water Resour. Res.*, *31*, 455–473, doi:10.1029/94WR02849.
- Lucy, L. B. (1977), A numerical approach to the testing of the fission hypothesis, *Astron. J.*, *82*, 1013–1024, doi:10.1086/112164.
- Luo, K., M.-P. Kuittu, C. Tong, S. Majaniemi, and T. Ala-Nissila (2005), Phase field modeling of wetting on structured surfaces, *J. Chem. Phys.*, *123*, 194702, doi:10.1063/1.2102907.
- Luo, L.-S., and S. S. Girimaji (2003), Theory of the lattice Boltzmann method: Two fluid model for binary mixtures, *Phys. Rev. E*, *67*, 036302, doi:10.1103/PhysRevE.67.036302.
- Majumder, M., N. Chopra, R. Andrews, and B. J. Hinds (2005), Nanoscale hydrodynamics: Enhanced flow in carbon nanotubes, *Nature*, *438*, 44, doi:10.1038/43844a.
- Malevanets, A., and R. Kapral (1999), Mesoscopic model for solvent dynamics, *J. Chem. Phys.*, *110*, 8605–8613, doi:10.1063/1.478857.
- Mandelbrot, B. B. (1983), *The Fractal Geometry of Nature*, W. H. Freeman, New York.
- Marangoni, C. (1865), *On the Expansion of a Drop of Liquid Floating on the Surface of Another Liquid*, Tipografia dei fratelli Fusi, Pavia, Italy.
- Martys, N. S., and H. Chen (1996), Simulation of multicomponent fluids in complex three-dimensional geometries by the lattice Boltzmann method, *Phys. Rev. E*, *53*, 743–750, doi:10.1103/PhysRevE.53.743.
- McNamara, G. R., and G. Zanetti (1998), Use of the Boltzmann equation to simulate lattice gas automata, *Phys. Rev. Lett.*, *61*, 3222–3225.
- Meakin, P. (1991), Fractal aggregates in geophysics, *Rev. Geophys.*, *29*, 317–354, doi:10.1029/91RG00688.
- Meakin, P. (1998), *Fractals, Scaling and Growth Far From Equilibrium*, Cambridge Univ. Press, Cambridge, U. K.
- Meakin, P., A. Tartakovsky, T. Scheibe, D. Tartakovsky, G. Redden, P. E. Long, S. C. Brooks, and Z. Xu (2007), Particle methods for simulation of subsurface multiphase fluid flow and biogeological processes, *J. Phys. Conf. Ser.*, *78*, U355–U364.
- Monaghan, J. J. (1992), Smoothed particle hydrodynamics, *Annu. Rev. Astron. Astrophys.*, *30*, 543–574, doi:10.1146/annurev.aa.30.090192.002551.
- Morris, J. P., P. J. Fox, and Y. Zhu (1997), Modeling moderate and low Reynolds number flows using SPH, *J. Comput. Phys.*, *136*, 214–226, doi:10.1006/jcph.1997.5776.
- Moseler, M., and U. Landman (2000), Formation, stability and breakup of nanojets, *Science*, *289*, 1165–1169, doi:10.1126/science.289.5482.1165.
- Moulinet, S., A. Rosso, W. Krauth, and E. Rolley (2004), Width distribution of contact lines on a disordered substrate, *Phys. Rev. E*, *69*, 035103, doi:10.1103/PhysRevE.69.035103.
- Narayan, O., and D. S. Fisher (1993), Threshold critical dynamics of driven interfaces in random media, *Phys. Rev. B*, *48*, 7030–7042, doi:10.1103/PhysRevB.48.7030.
- Nattermann, T., S. Setepanow, L. H. Tang, and H. Leschhorn (1993), Dynamics of interface depinning in a disordered medium, *J. Phys.*, *2*, 1483–1488.
- Nekovee, M., P. V. Coveney, H. D. Chen, and B. M. Boghosian (2000), Lattice-Boltzmann model for interacting amphiphilic fluids, *Phys. Rev. E*, *62*, 8282–8294.

- Nie, X. B., S. Y. Chen, W. N. E., and M. O. Robbins (2004), A continuum and molecular dynamics hybrid method for micro- and nano-fluid flow, *J. Fluid Mech.*, 500, 55–64, doi:10.1017/S0022112003007225.
- Nikunen, P., M. Karttunen, and I. Vattulainen (2003), How would you integrate the equation of motion in dissipative particle dynamics simulations?, *Comput. Phys. Commun.*, 153, 407–423, doi:10.1016/S0010-4655(03)00202-9.
- Nourgaliev, R. R., and T. G. Theofanous (2007), High fidelity interface tracking: Unlimited anchored level set, *J. Comput. Phys.*, 224, 836–866, doi:10.1016/j.jcp.2006.10.031.
- O’Connell, S. T., and P. A. Thompson (1995), Molecular dynamics-continuum hybrid computations: A tool for studying complex fluid flows, *Phys. Rev. E*, 52, R5792–R5795, doi:10.1103/PhysRevE.52.R5792.
- Onsager, L. (1931a), Reciprocal processes in irreversible processes I, *Phys. Rev.*, 37, 405–426, doi:10.1103/PhysRev.37.405.
- Onsager, L. (1931b), Reciprocal processes in irreversible processes II, *Phys. Rev.*, 38, 2265–2279, doi:10.1103/PhysRev.38.2265.
- Oren, P. E., S. Bakke, and O. J. Arntzen (1998), Extending predictive capabilities to network models, *SPE J.*, 3, 324–336, doi:10.2118/52052-PA.
- Osher, S., and S. Fedwick (2003), *Level Set Methods and Dynamic Implicit Surfaces*, Springer, New York.
- Pagonabarraga, I., and D. Frenkel (2001), Dissipative particle dynamics for interacting systems, *J. Chem. Phys.*, 115, 5015–5026, doi:10.1063/1.1396848.
- Paterson, L. (1984), Diffusion limited aggregation and two fluid displacement in porous media, *Phys. Rev. Lett.*, 52, 1621–1624, doi:10.1103/PhysRevLett.52.1621.
- Patzek, T. W. (2001), Verification of a complete pore network simulator of drainage and imbibition, *SPE J.*, 62, 144–156.
- Pereira, G. G. (1999), Numerical pore-scale modeling of three-phase fluid flow: Comparison between simulation and experiment, *Phys. Rev. E*, 59, 4229–4242, doi:10.1103/PhysRevE.59.4229.
- Podgorski, T., J. M. Flesselles, and L. Limat (2001), Corners, cusps, and pearls in running drops, *Phys. Rev. Lett.*, 87, 036102–036105, doi:10.1103/PhysRevLett.87.036102.
- Posch, H. A., W. G. Hoover, and O. Kum (1995), Steady state shear flows via nonequilibrium molecular dynamics and smooth-particle applied mechanics, *Phys. Rev. E*, 52, 1711–1720, doi:10.1103/PhysRevE.52.1711.
- Prevost, A., E. Rolley, and C. Guthmann (2002), Dynamics of a helium-4 meniscus on a strongly disordered cesium substrate, *Phys. Rev. B*, 65, 064517, doi:10.1103/PhysRevB.65.064517.
- Prigogine, I. (1947), *Etude Thermodynamique des Phenomenes Irreversibles*, Desoer, Liege, Belgium.
- Raiskinmaki, P., A. Skahib-Manesh, J. A. Koponen, J. Merikoski, and J. Tomonen (2002), Lattice-Boltzmann simulation of capillary rise dynamics, *J. Stat. Phys.*, 107, 143–158.
- Ramos, S. M., E. Charlaix, A. Benyagoub, and M. Toulemonde (2003), Wetting on nanorough surfaces, *Phys. Rev. E*, 67, 031604, doi:10.1103/PhysRevE.67.031604.
- Raviv, U., P. Laurat, and J. Klein (2001), Fluidity of water confined to sub nanometer films, *Nature*, 413, 51–54, doi:10.1038/35092523.
- Rider, W. J., and D. B. Koth (1998), Reconstructing volume tracking, *J. Comput. Phys.*, 141, 112–152, doi:10.1006/jcph.1998.5906.
- Rothman, D. H., and J. Keller (1988), Immiscible cellular automaton fluids, *J. Stat. Phys.*, 52, 1119–1127, doi:10.1007/BF01019743.
- Rothman, D. H., and S. Zaleski (1994), Lattice-gas models of phase separation: Interfaces, phase transitions and multiphase flow, *Rev. Mod. Phys.*, 66, 1417–1479, doi:10.1103/RevModPhys.66.1417.
- Ruckenstein, E., and C. S. Dunn (1977), Slip velocity during wetting of solids, *J. Colloid Interface Sci.*, 59, 135–138, doi:10.1016/0021-9797(77)90347-2.
- Sakai, T. (2002), Single phase and binary immiscible flow in porous media using the real-coded lattice gas, *J. Soc. Rheol.*, 30, 277–282, doi:10.1678/rheology.30.277.
- Sakai, T., Y. Chen, and H. Ohashi (2002a), Formation of micelle in real-coded lattice gas, *Colloids Surfaces A*, 201, 297–303, doi:10.1016/S0927-7757(01)01041-X.
- Sakai, T., Y. Chen, and H. Ohashi (2002b), Real-coded lattice gas model for ternary amphiphilic fluids, *Phys. Rev. E*, 65, 031503, doi:10.1103/PhysRevE.65.031503.
- Schaffer, E., and P.-Z. Wong (2000), Contact line dynamics near the pinning threshold, *Phys. Rev. E*, 61, 5257–5277, doi:10.1103/PhysRevE.61.5257.
- Scheibe, T. D., A. M. Tartakovsky, D. M. Tartakovsky, G. D. Redden, and P. Meakin (2007), Hybrid numerical methods for multi-scale simulations of subsurface biogeochemical processes, *J. Phys. Conf. Ser.*, 78, 012063, doi:10.1088/1742-6596/78/1/012063.
- Seppacher, P. (1996), Moving contact lines in the Cahn-Hilliard theory, *Int. J. Eng. Sci.*, 34, 977–992, doi:10.1016/0020-7225(95)00141-7.
- Sethian, J. A. (1999), *Level Set Methods and Fast Marching Methods: Evolving Interfaces in Computational Geometry, Fluid Mechanics, Computer Vision, and Material Science*, Cambridge Univ. Press, Cambridge, U. K.
- Shan, X., and H. Chen (1993), Lattice Boltzmann model for simulating flows with multiple phases and components, *Phys. Rev. E*, 47, 1815–1819.
- Shan, X., and H. Chen (1994), Simulation of nonideal gases and liquid-gas transitions by the lattice Boltzmann equation, *Phys. Rev. E*, 49, 2941–2948, doi:10.1103/PhysRevE.49.2941.
- Shao, S. D., and E. Y. M. Lo (2003), Incompressible SPH method for simulating Newtonian and non-Newtonian flows with a free surface, *Adv. Water Resour.*, 26, 787–800.
- Shi, Y., T. S. Zhao, and Z. L. Guo (2006), Lattice Boltzmann method for incompressible flows with large pressure gradients, *Phys. Rev. E*, 73, 026704, doi:10.1103/PhysRevE.73.026704.
- Sikalo, S., H.-D. Wilhelm, I. V. Roisman, S. Jakirlic, and C. Tropea (2005), Dynamic contact angle of spreading droplets: Experiments and simulations, *Phys. Fluids*, 17, 062103, doi:10.1063/1.1928828.
- Simms, P. H., and E. K. Yanful (2005), A pore-network model for hydromechanical coupling in unsaturated compacted clayey soils, *Can. Geotech. J.*, 42, 499–514, doi:10.1139/t05-002.
- Spanne, P., J. F. Thovert, C. J. Jacquin, W. B. Lindquist, K. W. Jones, and P. M. Adler (1994), Synchrotron computed microtomography of porous media: Topology and transports, *Phys. Rev. Lett.*, 73, 2001–2004, doi:10.1103/PhysRevLett.73.2001.
- Steeffel, C. I., D. J. DePaolo, and P. C. Lichtner (2005), Reactive transport modeling: An essential tool and a new research approach for the Earth sciences, *Earth Planet. Sci. Lett.*, 240, 539–558, doi:10.1016/j.epsl.2005.09.017.
- Stipp, S. L. S. (1998), Observation of hydrolysis, hydration and recrystallization on calcite surfaces exposed only to air, *Mineral. Mag.*, 62A, 1460–1462.
- Stokes, J. P., A. P. Kushnick, and M. O. Robbins (1988), Interface dynamics in porous media: A random-field description, *Phys. Rev. Lett.*, 60, 1386–1389, doi:10.1103/PhysRevLett.60.1386.
- Strating, E. H., and R. L. M. Vissers (1991), Dehydration-induced fracturing of eclogite-facies peridotites—Implications for the mechanical-behavior of subduction oceanic lithosphere, *Tectonophysics*, 200, 187–198, doi:10.1016/0040-1951(91)90014-J.
- Sun, Y., and C. Beckermann (2006), Sharp interface tracking using the phase field model, *J. Comput. Phys.*, 220, 626–653, doi:10.1016/j.jcp.2006.05.025.
- Sussman, M., A. S. Almgren, J. B. Bell, P. Collela, L. H. Howell, and M. L. Welcome (1999), An adaptive level set approach for incompressible two phase flows, *J. Comput. Phys.*, 148, 81–124, doi:10.1006/jcph.1998.6106.
- Svandal, A., B. Kvamme, L. Granasy, T. Pusztai, T. Buanes, and J. Hove (2006), The phase field theory applied to CO₂ and CH₄ hy-

- drate, *J. Cryst. Growth*, 287, 486–490, doi:10.1016/j.jcrysgro.2005.11.071.
- Swift, M. R., E. Orlandi, W. R. Osborn, and J. M. Yeomans (1996), Lattice Boltzmann simulations of liquid-gas and binary fluid systems, *Phys. Rev. E*, 54, 5041–5052, doi:10.1103/PhysRevE.54.5041.
- Tada, R., and R. Siever (1989), Pressure solution during diagenesis, *Annu. Rev. Earth Planet. Sci.*, 17, 89–118, doi:10.1146/annurev.ea.17.050189.000513.
- Takeda, H., S. M. Miyama, and M. Sekiya (1994), Numerical simulation of viscous flow by smoothed particle hydrodynamics, *Prog. Theor. Phys.*, 92, 939–960, doi:10.1143/PTP.92.939.
- Tang, C., and P. Bak (1988), Critical exponents and scaling relations for self-organized critical phenomena, *Phys. Rev. Lett.*, 60, 2347–2350, doi:10.1103/PhysRevLett.60.2347.
- Tang, L.-H., and H. Leschorn (1992), Pinning by directed percolation, *Phys. Rev. A*, 45, R8309–R8312, doi:10.1103/PhysRevA.45.R8309.
- Tang, L.-H., M. Kardar, and D. Dahr (1995), Driven depinning in anisotropic media, *Phys. Rev. Lett.*, 74, 920–923, doi:10.1103/PhysRevLett.74.920.
- Tanner, L. (1979), The spreading of silicone oil drops on horizontal surfaces, *J. Phys. D*, 12, 1473–1484, doi:10.1088/0022-3727/12/9/009.
- Tartakovsky, A. M., and P. Meakin (2005a), Simulation of free-surface flow and injection offluids into fracture apertures using smoothed particle hydrodynamics, *Vadose Zone J.*, 4, 848–855, doi:10.2136/vzj2004.0178.
- Tartakovsky, A. M., and P. Meakin (2005b), A smoothed particle hydrodynamics model for miscible flow in three-dimensional fractures and the two-dimensional Rayleigh-Taylor instability, *J. Comput. Phys.*, 207, 610–624, doi:10.1016/j.jcp.2005.02.001.
- Tartakovsky, A. M., and P. Meakin (2005c), Modeling of surface tension and contact angles with smoothed particle hydrodynamics, *Phys. Rev. E*, 72, 026301, doi:10.1103/PhysRevE.72.026301.
- Tartakovsky, A. M., and P. Meakin (2006), Pore-scale modeling of immiscible and miscible flows using smoothed particle hydrodynamics, *Adv. Water Resour.*, 29, 1464–1478, doi:10.1016/j.advwatres.2005.11.014.
- Tartakovsky, A. M., P. Meakin, T. D. Scheibe, and R. M. Eichler West (2007a), Simulations of reactive transport and precipitation with smoothed particle hydrodynamics, *J. Comput. Phys.*, 222, 654–672, doi:10.1016/j.jcp.2006.08.013.
- Tartakovsky, A. M., P. Meakin, T. Scheibe, and B. Wood (2007b), A smoothed particle hydrodynamics model for reactive transport and mineral precipitation in porous and fractured porous media, *Water Resour. Res.*, 43, W05437, doi:10.1029/2005WR004770.
- Tartakovsky, A. M., A. L. Ward, and P. Meakin (2007c), Pore-scale simulations of drainage of heterogeneous and anisotropic porous media, *Phys. Fluids*, 19, 103301, doi:10.1063/1.2772529.
- Tartakovsky, A. M., G. Redden, P. C. Lichtner, T. D. Scheibe, and P. Meakin (2008a), Mixing induced precipitation: Experimental study and multiscale numerical analysis, *Water Resour. Res.*, 44, W06S04, doi:10.1029/2006WR005725.
- Tartakovsky, A. M., D. M. Tartakovsky, T. D. Scheibe, and P. Meakin (2008b), Hybrid simulation of reaction-diffusion systems in porous media, *SIAM J. Sci. Comput.*, 30, 2799–2816, doi:10.1137/070691097.
- Ten Berge, H. F. M., and G. H. Bolt (1988), Coupling between liquid flow and heat flow in porous media: A connection between two classical approaches, *Transp. Porous Media*, 3, 35–49.
- Thompson, K. E., and H. S. Fogler (1998), Pore-scale model for fluid injection and in situ gelation in porous media, *Phys. Rev. E*, 57, 5825–5832, doi:10.1103/PhysRevE.57.5825.
- Tiwari, A., and J. Abraham (2006), Dissipative particle dynamics for two-phase flow, *Phys. Rev. E*, 74, 056701, doi:10.1103/PhysRevE.74.056701.
- Tsakiroglou, C. D., and A. C. Payatakes (2000), Characterization of the pore structure of reservoir rocks with the aid of serial sectioning analysis, mercury porosimetry and network simulation, *Adv. Water Resour.*, 23, 773–789, doi:10.1016/S0309-1708(00)00002-6.
- Tsimpanogiannis, I. N., and P. C. Lichtner (2006), Pore-network study of methane hydrate dissociation, *Phys. Rev. E*, 74, 056303, doi:10.1103/PhysRevE.74.056303.
- Unverdi, S. O., and G. Tryggvason (1992), A front-tracking method for viscous, incompressible, multifluid flows, *J. Comput. Phys.*, 100, 25–37, doi:10.1016/0021-9991(92)90307-K.
- Urbach, J. S., R. C. Madison, and J. T. Markert (1995), Interface depinning, self organized criticality and the Barkhausen effect, *Phys. Rev. Lett.*, 75, 276–279, doi:10.1103/PhysRevLett.75.276.
- van der Waals, J. D. (1873), Over de Continuïteit van den Gas- en Vloeistoftoestand, thesis, Univ. Leiden, Leiden, Netherlands.
- van der Waals, J.D. (1893), The thermodynamic theory of capillarity under the hypothesis of a continuous density variation (in Dutch), *Verh. K. Akad. Wet. Amsterdam, Sect. 1*, 1(8). (English translation, J. S. Rowlinson, *J. Stat. Phys.*, 20, 197–244, 1979.)
- van Dijke, M. I. J., and K. S. Sorbie (2003), Pore-scale modeling of three-phase flow in mixed wet porous media: Multiple displacement chains, *J. Petrol. Sci. Eng.*, 39, 201–216, doi:10.1016/S0920-4105(03)00063-9.
- Vedvik, A., G. Wagner, U. Oxaal, J. Feder, P. Meakin, and T. Jossang (1998), The fragmentation transition for invasion percolation in hydraulic gradients, *Phys. Rev. Lett.*, 80, 3065–3068, doi:10.1103/PhysRevLett.80.3065.
- Verhaeghe, F., S. Arnout, B. Blanpain, and P. Wollants (2005), Lattice Boltzmann model for diffusion-controlled dissolution of solid structures, *Phys. Rev. E*, 72, 036308.
- Wang, M., and Z. X. Li (2003), Nonideal gas flow and heat transfer in micro- and nanochannels using the direct simulation Monte Carlo method, *Phys. Rev. E*, 68, 046704.
- Wells, J. T., D. R. Janecky, and B. J. Travis (1991), A lattice gas automata model for heterogeneous reactions at mineral surfaces and in pore networks, *Physica D*, 47, 115–123, doi:10.1016/0167-2789(91)90284-G.
- Wilkinson, D., and J. F. Willemsen (1983), Invasion percolation: A new form of percolation, *J. Phys. A Math. Gen.*, 16, 3365–3376, doi:10.1088/0305-4470/16/14/028.
- Witten, T. A., Jr., and L. M. Sander (1981), Diffusion-limited aggregation: A kinetic critical phenomenon, *Phys. Rev. Lett.*, 47, 1400–1403, doi:10.1103/PhysRevLett.47.1400.
- Wong, P.-Z., and J. W. Cable (1983), Hysteresis behavior in the diluted random-field Ising system $\text{Fe}_{0.70}\text{Mg}_{0.30}\text{Cl}_2$, *Phys. Rev. B*, 28, 5361–5364, doi:10.1103/PhysRevB.28.5361.
- Xu, C. S., C. Hang, D. Montiel, and H. Yang (2007), Rapid and quantitative sizing of nanoparticles using three-dimensional single particle tracking, *J. Phys. Chem. C*, 111, 32–35, doi:10.1021/jp0671796.
- Xu, Z., and P. Meakin (2008), Phase-field modeling of solute precipitation and dissolution, *J. Chem. Phys.*, 129, 014705, doi:10.1063/1.2948949.
- Xu, Z., P. Meakin, and A. Tartakovsky (2009), A diffuse-interface model for smoothed particle hydrodynamics, *Phys. Rev. E*, in press.
- Yardley, B. W. O., and S. H. Bottrell (1988), Immiscible fluids in metamorphism: Implications of two-phase flow for reaction history, *Geology*, 16, 199–202, doi:10.1130/0091-7613(1988)016<0199:IFIMIO>2.3.CO;2.
- Yeong, C. L. Y., and S. Torquato (1998), Reconstructing random media, *Phys. Rev. E*, 57, 495–506, doi:10.1103/PhysRevE.57.495.
- Yiotis, A. G., I. N. Tsimpanogiannis, A. K. Stubos, and Y. C. Yortsos (2006), Pore-network study of the characteristic periods in the drying of porous materials, *J. Colloid Interface Sci.*, 297, 738–748, doi:10.1016/j.jcis.2005.11.043.

- Yu, C.-J., A. G. Richter, A. Datta, M. K. Durbin, and P. Datta (1999), Observation of molecular layering in thin liquid films using x-ray reflectivity, *Phys. Rev. Lett.*, 82, 2326–2329, doi:10.1103/PhysRevLett.82.2326.
- Zheng, H. W., C. Shu, and Y. T. Chew (2006), A lattice Boltzmann model for multiphase flows with high density ratio, *J. Comput. Phys.*, 218, 353–371, doi:10.1016/j.jcp.2006.02.015.
- Zhu, Y., and P. J. Fox (2002), Simulation of pore-scale dispersion in periodic porous media using smoothed particle hydrodynamics, *J. Comput. Phys.*, 182, 622–645.
- Zhu, Y., P. J. Fox, and J. P. Morris (1997), Smoothed particle hydrodynamics model for flow through porous media, in *Computer Methods and Advances in Geomechanics*, vol. 2, edited by J.-X. Yuan, pp. 1041–1046, Balkema, Rotterdam, Netherlands.
- Zhu, Y., P. J. Fox, and J. P. Morris (1999), A pore-scale numerical model for flow through porous media, *Int. J. Numer. Anal. Methods Geomech.*, 23, 881–904.
-
- P. Meakin, Center for Advanced Modeling and Simulation, Idaho National Laboratory, Idaho Falls, ID 83415, USA. (paul.meakin@inl.gov)
- A. M. Tartakovsky, Computational Mathematics Technical Group, Computational and Information Sciences Directorate, Pacific Northwest National Laboratory, Richland, WA 99352, USA.